THEORETICAL STUDIES OF NON-LINEAR ELECTROTHERMAL INSTABILITIES IN A FULLY IONIZED PLASMA

by

FRANCESCA MARSH

A thesis submitted for the degree of Doctor of Philosophy of the University of London and for the Diploma of Membership of the Imperial College

Blackett Laboratory
Imperial College of Science and Technology
London

March 1982

TO MY

PARENTS

ABSTRACT

The non-linear behaviour of electrothermal instabilities in a fully ionised, homogeneous, two temperature plasma is studied using a fluid model. The current is carried predominantly parallel to the magnetic field, as in the Tokamak configuration, and modes with wave vector $\underline{K}$ perpendicular to the magnetic field are considered. The optimum wavelength for growth of such modes has previously been shown to be of the order of a few ion Larmor radii, with growth rates of the order of the Ohmic heating rate. The inclusion of Bremsstrahlung radiation loss is shown to enhance the instability.

Non-linear steady-state solutions of the electron energy equation reveal the possibility of large amplitude filaments of current when the instability has developed and saturated. Furthermore it is shown that ion acoustic turbulence and electron runaway can occur in the maxima of the current filaments; although the average plasma parameters preclude the existence of either of these phenomena. The possible effects of the presence of these filaments on electron energy transport is considered.

The development in time of the electrothermal instability in one space dimension is followed numerically. The two cases of constant applied electric field, and constant total current are considered. In the former case it is found that the instability develops until a point is reached when the electron temperature increases everywhere and the system runs away. In the latter case a filamentary structure develops and a steady state is reached for short wavelengths. For longer wavelength, faster growing modes the condition for onset of ion acoustic instability is violated in the filament peaks. The model is changed to

include the effects of the presence of ion acoustic turbulence and the results from it are discussed.

ACKNOWLEDGEMENTS

The work in this thesis was performed while the author was a member of the Plasma Physics Group at the Blackett Laboratory, Imperial College. I would like to thank all the members of this group for many stimulating discussions. In particular I would like to thank the following people and organisations for their assistance in various ways :

Professor M.G. Haines, my supervisor, for his valuable guidance throughout this work.

Dr D.J. Bond for many enlightening and pertinent discussions at the most crucial stages.

Dr D.E. Potter for his assistance with some of the computational problems encountered.

Dr J. Wesson of Culham Laboratory for many inspiring and helpful comments in the latter part of the research.

The Science Research Council and Culham Laboratory for financial support.

Finally I would like to thank my husband Bowker for his relentless support throughout and his refreshing approach to the subject of Plasma Physics.

LIST OF CONTENTS

LIST OF FIGURES

5.3

b Number density profiles

c z-component of current density profiles

d y-component of current density profiles

e z-component of magnetic field profiles

f Total pressure profiles

g Variation in time of the rate of change of the electric field and the rate of change of the internal energy

5.4 Mesh length set equal to six scale lengths

a Spatial variation of electron temperature at various times

b Number density profiles

c z-component of current density profiles

d y-component of current density profiles

e z-component of magnetic field profiles

f Total pressure profiles

g Variation in time of the rate of change of the internal energy and the rate of change of the electric field

5.5 Mesh length set equal to seven scale lengths

a Spatial variation of electron temperature at various times

b Number density profiles

c z-component of current density profiles

d y-component of current density profiles

e z-component of magnetic field profiles

f Total pressure profiles

g Variation in time of the rate of change of the maximum electron temperature, the rate of change of the internal energy and the rate of change of the electric field

5.6 Mesh length set equal to eight scale lengths

a Spatial variation of electron temperature at various times

b Number density profiles

c z-component of current density profiles

d y-component of current density profiles

e z-component of the magnetic field profiles

f Variation in time of the rate of change of the electric field and the rate of change of the internal energy

Chapter 6

6.3 The effects of ion acoustic turbulence on the development of the filament

a Electron temperature profiles at various times

b z-component of current density profiles

c y-component of current density profiles

d Number density profiles

e Variation in time of the rate of change of the electric field

f Spatial variation of the anomaly factor ξ at various times

Steady-state profiles of :

g The electron temperature

h The z-component of the current density

i The number density

j The anomaly factor ξ

LIST OF SYMBOLS

A_F	initial drift speed over initial sound speed
A_H	the ratio of the electric field to some natural electric field
a_e	electron Larmor radius
a_i	ion Larmor radius
α^1	Spitzer conductivity constant
α	linear growth rate
α_1	a switch parameter
α_2	a switch parameter
$\underline{B}$	magnetic field
β_e	ratio of kinetic to magnetic pressures
B	dimensionless constant determining the strength of the radiation term
β_r	Bremsstrahlung radiation coefficient
c^1	thermal conductivity constant
c_1, c_2	constants of integration
c(t)	time dependent constant of integration
c	velocity of light
c_s	ion sound speed
Δx	distance between adjacent mesh points
Δt	time step
δ_{im}	Kronecker delta function
e	magnitude of charge on one electron
$\underline{E}$	electric field
E_I	internal energy
F	a function measuring the relative strength of the magnetic field
f_o	a function measuring the initial strength of the magnetic field
ε	a dimensionless parameter

$\hbar$	Planck's constant
$\underline{j}$	current density
k_B	Boltzmann's constant
$\underline{K}$	wave vector
K_e	classical thermal conductivity coefficient
$\chi_{\perp e}, \chi_{\perp i}$	electron and ion thermal conductivity perpendicular to the magnetic field
L_o	scale length
λ_m	mesh length
m_e	electron mass
m_i	ion mass
n	number density
n	time step number
p	iteration step number
p, p_e, p_i	total pressure and electron and ion pressures
π_e	initial ratio of kinetic to magnetic pressure
R	a dimensionless constant measuring radiation strength
s	dimensionless distance
σ	electrical conductivity
t	dimensionless electron temperature in units of ion temperature
t_o	scale time
t	dimensionless time
T_e	electron temperature
T_i	ion temperature
τ_e	electron-ion collision time
$\underline{U}$	drift velocity
V_d	drift velocity
V, V_e, V_i	centre of mass velocity and electron and ion velocities
ω_e	electron cyclotron frequency
x	dimensionless linear growth rate
y	square of the dimensionless wave number

CHAPTER 1

INTRODUCTION

This work was embarked upon in an attempt to explain the anomalously high electron energy loss observed experimentally in Tokamaks[1]. The anomalous electron energy loss rate is reflected in the electron energy confinement time, which is tens of times smaller than predicted by theory. With this aim in mind, we study the non-linear behaviour of an electrothermal instability in a fully ionised, magnetised, two temperature plasma using a fluid model. If this instability exists in Tokamaks, it may increase the electron energy loss rate by increasing the rate at which energy is equipartitioned to the ions to a rate above that calculated assuming the electrothermal instability were absent.

In Chapter 1 we review the work done by other authors on electrothermal instabilities; not only in fully ionised, but also in partially ionised, gases. The review leads us to the reasons why the work in this thesis was carried out. A description is given of how the electrothermal instability manifests itself in a fully ionised, magnetised two temperature plasma, and under what conditions it exists. It is this type of electrothermal instability which is the theme of this thesis. Finally in Chapter 1, we define and briefly describe the basic equations from which most of the equations used in the rest of this thesis are derived.

In Chapter 2 we add to existing results[2] of the linear behaviour of an electrothermal instability by including a radiation loss term. The effect of Bremsstrahlung loss is specifically described, and from the

mechanism by which it affects the instability, we deduce how the presence of other, more important, radiation loss terms would affect this instability. Also in this chapter we analyse the model used by Tomimura and Haines[3] to test its suitability for the basis of a numerical simulation to follow the growth of an electrothermal instability into the non-linear regime. Consequently, some changes are made to the model used in [3] which facilitate the computer model without substantially affecting the behaviour of the instability.

A study is made in Chapter 3 of the properties of possible saturated steady states of the electrothermal instability. The results obtained from this model are shown to depend strongly on which of the many possible steady states the electrothermal instability relaxes to if any. One is unable to predict from this model either the steady state which would be preferred if the instability were allowed to develop from a small, random perturbation, or the time taken to reach it[4].

The numerical model used to follow the evolution of an intially small, random perturbation about a steady state into the non-linear regime is developed in Chapter 4. The model used by Tomimura and Haines[3] is modified on the grounds of the results found in Chapter 2. In this chapter we describe the computational and mathematical problems arising in the simulation and how they are dealt with. During the simulation it is found necessary to solve a sparse matrix equation rapidly. A description of the method and the computer program used for this purpose is given in Appendix A. Appendix B contains a discussion of the details of the numerical stability test also used in the simulation.

In Chapter 5 we present the results from the numerical model. These results fall into two main categories; those obtained when the applied electric field to maintain the discharge is held constant in time and those obtained when the electric field is allowed to vary in time

to keep the total current constant.

In the last chapter of this thesis we formulate a model to include the macroscopic effects of ion acoustic turbulence on the evolution of the instability. Some calculations are presented showing the effect on energy transport and on electrical conductivity.

A general review of electrothermal instabilities

Electrothermal instabilities cover a broad class of thermal instabilities in which Ohmic dissipation provides the free energy to drive the instability. They have been shown to occur in many different types of plasma, and their nature and behaviour varies considerably with the device in which they occur.

The presence of electrothermal instabilities in alkali seeded noble gases has been experimentally observed by many authors [e.g. 5 and 6]. The instability mechanism in partially ionised gases[7,8,9] depends on the high sensitivity of the degree of ionisation of the gas to electron temperature. Nelson and Haines[8] made an extensive survey of the properties of this kind of instability, incorporating the effects of finite ionisation rates, energy convection, radiation transfer, thermal conduction, finite degree of ionisation and Coulomb as well as neutral collisions. In this model the electron density is in Saha equilibrium at the electron temperature. Perturbations of the electron temperature lead to much larger perturbations in the electron density. These larger fluctuations in electron density substantially alter the plasma parameters, such as conductivity and Hall parameter, and the energy balance in the plasma is altered so that the fluctuations are amplified under certain conditions. In general these fluctuations can propagate as a wave. If the Hall parameter, defined as

$$\omega_e \tau_e = \frac{\sigma B}{n_e e c}$$

(when σ is the electrical conductivity, $\underline{B}$ the magnetic field, n_e the electron number density, e the charge on an electron and c the velocity of light) is greater than some critical value, growth of the instability occurs because the perturbed Ohmic heating rate exceeds the perturbed equipartition rate to the neutrals. The critical value for the Hall parameter exists because only when this is exceeded is the perturbed current large enough to produce a perturbed Ohmic heating rate greater than the perturbed equipartition rate which depends upon the electron density. The wave vector is perpendicular to the magnetic field here, and maximum growth rate occurs with an angle of about 45° between the wave vector and the current vector. This is because the perturbed Ohmic heating peaks when the perturbed current, which is perpendicular to the wave vector (charge conservation), is parallel to the zero order current, but the all important contribution to the perturbed current from the Hall term peaks when the wave vector is parallel to the zero order current. The growth time for these instabilities is typically of the order of 10^{-6} seconds. They can occur in closed loop magnetohydrodynamic generators and are of great importance because non uniformities in the electron density and temperature have a damaging effect on the performance of the generator. We note here that radiation transfer is shown in this paper to have a damping effect on these instabilities.

We now turn our attention to the work done on the nature and behaviour of the electrothermal instability in a fully ionised, resistive plasma. Haines[10] succeeded in explaining the break up of a plasma shell into separated current elements during the early stages of a θ pinch, reported by Dixon et al[11], in terms of such an instability where the wave vector is parallel to the magnetic field and perpendicular to

the current. It was in this paper that the behaviour and the conditions for onset of the non convective electrothermal mode were first calculated. These conditions and a description of the instability mechanism is deferred to the next paragraph where we discuss the nature of the instability with the wave vector perpendicular to the magnetic field. Returning to the work in [10], the growth time, for conditions relevant to a θ pinch, was found to be of the order of 10^{-6} seconds for wavelengths of the order of a few centimetres or less. It was also pointed out that, for conditions relevant to Tokamaks, using this model, the wavelength of the instability would be much longer and the growth rates much shorter and therefore the instability of no interest. However they realised that the situation may be changed if the wave vector were perpendicular to the magnetic field instead of parallel. This is because, as will be seen later, one of the factors determining the wavelength of the instability is the effect of the thermal conduction which damps the short wavelength modes. Across the magnetic field, in a Tokamak, the thermal conduction would be severely reduced by a factor $(1 + \omega_e^2\tau_e^2)$ (where $\omega_e\tau_e$ is the Hall parameter). Also the growth rate, which goes like the Ohmic heating rate, would be larger in the early stages at low temperatures. This partly inspired the work carried out by Tomimura and Haines[2] on the behaviour of the electrothermal instability in a fully ionised plasma with wave vector perpendicular to the magnetic field. Further inspiration for this work came from the appearance of (spatially) oscillatory electron temperature profiles when they studied the steady-state of a diffuse pinch in cylindrical geometry[12].

The work in this thesis was largely inspired by the work done by Tomimura and Haines[2] on the linear theory of electrothermal instabilities in a fully ionised, magnetised, two temperature plasma

with wave vector $\underline{K}$ perpendicular to the magnetic field $\underline{B}$. It seems fitting, therefore, to report here in greater detail on the salient features of, and pertinent results, from the above mentioned work, in order to establish the foundations for this non-linear model.

In a fully ionised, magnetised plasma the electrothermal instability presents itself as spatial oscillations in electron temperature, number and current density, as well as in electric and magnetic fields. The free energy to drive the instability is provided by Ohmic dissipation. Physically, the unstable modes are driven, in most cases, by the following mechanism. A local increase in electron temperature increases the electrical conductivity, using a Spitzer model. The current flows preferentially in that region, hence increasing the local Ohmic heating rate. If the corresponding changes in energy dissipation rate mechanisms, such as equipartition from the electrons to the ions, electron thermal conduction, and radiation loss, do not equal this increased Ohmic heating rate, the perturbation in electron temperature will grow. In some cases, however, with long wavelength convective modes, it is the local decrease in the equipartition rate, as opposed to any increase in the Ohmic heating rate, providing the net source of energy required to make the perturbation grow.

Tomimura and Haines completed an extensive analysis of the nature of electrothermal instabilities, which can be divided into two main sections each with two subsections :

1. a) A scalar conductivity assumption, neglecting thermoelectric forces, with ion at rest.
   b) As above but with ion motion included.
2. a) A tensor conductivity model including thermo-electric forces with ions at rest

b) As above, with ion motion included.

From the model in 1a) above, they discovered the condition for existence of the unstable non-convective mode to be,

$$\frac{T_{eo}}{T_i} > \frac{3}{2}$$

where T_{eo} represents the equilibrium electron temperature (uniform in space) before a perturbation is applied. T_i represents the ion temperature considered uniform in space and constant in time. The condition above was also found by Furth et al[13] when they studied the thermal stability of a Tokamak. Returning to 1a) above, they discovered the optimum wavelength for growth of this instability is a few times greater than $(\frac{m_i}{m_e})^{\frac{1}{2}} a_{eo}$, where a_{eo} represents the electron Larmor radius measured at the equilibrium values. The maximum growth rate is of the order of $(\frac{m_e}{m_i})\ \nu_{ei}$ in most cases, where ν_{ei} is the electron-ion collision frequency.

From the model briefly described by 1b), they discovered the existence of a convective unstable mode at long wavelengths which was not found in the previous model. This mode disappears for very large values of $(\omega_e \tau_e)^2$, relevant to fusion conditions. The condition for existence of the non-convective mode becomes,

$$\frac{T_{eo}}{T_i} > 1.3187$$

and this time a second condition, which at large values of $\omega_e \tau_e$ simplifies to, in terms of the plasma beta

$$\beta = \frac{8\pi n_o k_B (T_{eo}+T_i)}{B_o^2} < 1.07\ (1 + T_i/T_{eo})$$

where n_o is the equilibrium density, T_{eo} the electron temperature, T_i the ion temperature, k_B Boltzmann's constant and B_o the magnetic field. The optimum wavelength for growth and the maximum growth rate are more difficult to assess in this model. However, they did establish that, for large values of $(\omega_e\tau_e)^2$, the optimum wavelength and growth rate do not depend upon $\omega_e\tau_e$.

The results above are not substantially modified in model 2) with tensor conductivity assumption and thermo electric effects included. There is a reduction in the range of wavelengths for which the non-convective unstable mode exists, as well as an increase in its optimum wavelength for growth as compared with model 1).

Motivation for the work in this thesis

Electrothermal instabilities in a fully ionised plasma have been successfully used to explain the break up of a plasma shell in the early stages of a θ pinch[10]. It has also been shown that they can occur in Tokamak type discharges[3]; if they occurred in the early Ohmic heating phase their growth rates could be large enough for their presence to be important. Furthermore, their presence would not be detected using existing diagnostic techniques[14], assuming the dominant mode to be the one with the largest growth rate as found from linear theory. This is because, the resultant electron temperature fluctuations would occur over a distance of the order of centimetres or less. Changes over this distance would not be spatially resolved using Thomson scattering[15]. The presence of such fine scale fluctuations could affect the transport processes in a Tokamak. Before this hypothesis can be tested it is necessary to establish the time it

takes for the instability to develop fully and compare this with the appropriate time scales in a Tokamak. It is also necessary to study the nature and behaviour of the fully developed instability.

Transport and Maxwell's Equations

The purpose of this section is to define the equations, and introduce the notation used throughout this thesis. The transport equations used are briefly derived from well established starting points, and expressed in a form suitable for the plasma model considered. The regime of validity of the equations is summarised.

1.1 Transport Equations

The transport equations, for a fully ionised plasma comprised of electron and a single ion species with charge e, consist of the equations of continuity, momentum transport, and heat balance for the ions and the electrons. Assuming neutrality so that $n_e = n_i = n$ these equations may be written as follows :

Continuity Equation

$$\frac{\partial n}{\partial t} + \nabla.(n\underline{V}_s) = 0 \qquad (1.1.1)$$

Momentum Transport

$$m_s\, n\left(\frac{\partial \underline{V}_s}{\partial t} + (\underline{V}_s.\nabla)\,\underline{V}_s\right) = -\nabla p_s - \nabla.\underline{\underline{\pi}}_s + e_s n\left(\underline{E} + \frac{\underline{V}_s \times \underline{B}}{c}\right) + \underline{R}_s \qquad (1.1.2)$$

Heat Balance

$$\frac{3}{2} nk_B \left(\frac{\partial T_s}{\partial t} + (\underline{V}_s.\nabla)\,T_s\right) + nk_B T_s\, \nabla.\underline{V}_s + \underline{\underline{\pi}}_s : \nabla\underline{V}_s + \nabla.\underline{q}_s = Q_s \qquad (1.1.3)$$

for both species, s.

These equations, describing the transport of particles, momentum, and internal energy in an ionised gas are obtained by taking zeroth, first and second order moments of the Boltzmann kinetic equations respectively for both species. The velocity of each particle is then divided into two parts, a mean velocity $\underline{V}_s$ and a random velocity $\underline{V}_s^1$ and identifying some average quantities with macroscopic parameters. It is assumed that total momentum and energy are conserved in collisions, and momentum and energy are conserved in collisions between particles of one species, that is elastic collisions only are considered. The gas is fully ionised and neither production nor annihilation of particles is allowed. Hence the right hand side of equation (1.1.1) is zero.

In equation (1.1.2) m_s represents the mass of the particle species, p_s the scalar pressure. The complete pressure tensor is

$$\underline{\underline{P}}_s = p_s \underline{\underline{I}} + \underline{\underline{\pi}}_s$$

where the traceless tensor $\underline{\underline{\pi}}_s$ represents the part of $\underline{\underline{P}}$ arising from any anisotropy in the random velocity part of the distribution function. $\underline{E}$ and $\underline{B}$ represent macroscopic fields averaged over a volume containing many particles and over times long compared to some appropriate scale time. (The effects of rapidly fluctuating microfields are taken care of in the collision term.) $\underline{R}$ represents the mean change in the momentum of the particles of one species due to collisions with all other particles. k_B, in equation (1.1.3) is Boltzmann's constant. This equation, for the internal energy transport, is derived from the total energy transport equation by eliminating the kinetic energy part with the aid of the other two equations. T_s is the temperature of the species measured in °K, while $\underline{q}$ is the heat flux density representing transport of energy associated with random motion. Finally, Q is

the heat generated in one species due to collisions with the other species. The Gaussian system of units is employed throughout this work.

Transport Coefficients

In order to close the above equations, it is necessary to derive the relationships between π_s, $\underline{q}_s$, $\underline{R}_s$, Q_s and n_s, $\underline{V}_s$, T_s, and the derivatives of the latter. The corresponding coefficients of proportionality are known as the transport coefficients. These coefficients for a fully ionised gas have been calculated in [16-19] and in other literature, and will only be quoted in this work as and when they are used.

Conditions of Applicability

Although the difficult and extensive task of determining the transport coefficients has been carried out by many authors in different forms, in all cases their results apply only when the local distribution is very close to a Maxwellian. In a fully ionised plasma the ratio of the masses of the two components is very small (the electron to the ion mass ratio). As a consequence of this, a local Maxwellian distribution is established within each component before it is established between the components. This point makes it possible to obtain transport equations when the ion and electron temperatures differ. Hence the plasma can be considered to be made up of two interpenetrating fluids.

The important approximation that the local distribution is very close to a Maxwellian restricts the regime of validity of the transport equations. In essence, they can only be considered valid when the phenomena they are being used to describe are such that all

average quantities in the plasma change slowly in space and time compared to some characteristic scale length and time. The distribution function becomes Maxwellian in a time of the order of a collision time τ. Therefore all plasma quantities must not change significantly in time τ. This may be expressed mathematically as :

$$\frac{d}{dt} << \frac{1}{\tau}$$

When there is a very small or no magnetic field ($\omega_e \tau_e \lesssim 1$, where ω_e is the electron cyclotron frequency and τ_e the electron-ion collision time), the characteristic scale length over which plasma quantities vary must be much larger than the mean free path between collisions :

$$\nabla \sim \frac{1}{L} \quad \therefore \quad L >> \ell mfp$$

However, when the magnetic field is very strong, ($\omega_e \tau_e >> 1$), the motion of the particles in the direction perpendicular to the magnetic field is bounded by the Larmor radius, which is smaller than the mean free path. So that the validity condition becomes :

$$L_\perp >> a, \qquad L_\parallel >> \ell mfp$$

where $L_\perp$ and $L_\parallel$ are the characteristic distances in the perpendicular and parallel directions to the magnetic field respectively, and a is the Larmor radius.

Maxwell's Equations

Other equations appearing in this work are the two vector Maxwell equations

$$\nabla \times \underline{E} = -\frac{1}{c}\frac{\partial \underline{B}}{\partial t} \qquad (1.1.4)$$

otherwise known as Faraday's Law, and Ampère's Law :

$$\nabla \times \underline{B} = \frac{4\pi}{c}\underline{j} + \frac{1}{c}\frac{\partial \underline{E}}{\partial t} \qquad (1.1.5)$$

A dimensional analysis of (1.1.4) shows that

$$\frac{E}{B} \sim \frac{\omega L}{c}$$

where L and ω^{-1} are, respectively, a length and a time over which the electric and magnetic fields change appreciably. For the interaction between flow and macroscopic fields to be significant, the flow velocity V associated with the plasma should intuitively satisfy

$$V \sim \omega L$$

this implies

$$\frac{\omega L}{c} << 1$$

performing a dimensional analysis to compare the relative magnitude of the terms in equation (1.1.5) one obtains :

$$\left|\frac{1}{c}\frac{\partial \underline{E}}{\partial t}\right| / \left|\nabla \times \underline{B}\right| \sim \left(\frac{\omega L}{c}\right)^2 << 1$$

therefore (1.1.5) is replaced by

$$\nabla \times \underline{B} = \frac{4\pi}{c}\underline{j} \qquad (1.1.6)$$

This is the form of Ampère's Law used.

CHAPTER 2

THE PLASMA MODEL AND LINEAR THEORY EXTENDED

INTRODUCTION

In this chapter the linear behaviour of the electrothermal instability is discussed in greater detail than the results from it warrant. That is, the results obtained here are only a small extension of published theory[2, 13]. However, the detailed discussion serves to establish the plasma model and all the basic equations used in the rest of the thesis; hence combining the tasks of deriving the additional results to existing linear theory and describing the conditions under which the evolution of the electrothermal instability into the non-linear regime is followed.

Extensive as it is, the analysis performed by Tomimura and Haines, in [2], did not include the effects of radiation loss on an electrothermal instability. As a fully ionized hydrogen plasma is being studied and for simplicity, the only radiation loss mechanism considered is Bremsstrahlung. This is the subject of the first part of this chapter. As the results that follow show, the inclusion of Bremsstrahlung radiation loss enhances the instability because of its $n^2 T_e^{\frac{1}{2}}$ dependence.

The main reason for using perturbation theory is to determine, as far as possible, what physical effects are responsible for various aspects of the electrothermal instability. Having done so, the relative importance of the terms representing these physical effects is assessed, and the conditions under which they can be neglected, if at all,

quantified. The information gleaned from this exercise is then used to facilitate the formulation of the model used to describe the evolution of the aforementioned instabilities in Chapter 4.

The analysis described below follows closely that first used by Haines[10], and later by Tomimura and Haines[2]. For simplicity, and to avoid conditions giving rise to gradient driven drift instabilities, the stability analysis is carried out in an infinite, homogeneous plasma with wave vector perpendicular to the magnetic field and current, with uniform equilibrium profiles for number density and temperatures. This approach is acceptable provided the wave lengths of the perturbation are much smaller than the scale lengths over which the equilibrium quantities vary. We know from the last chapter, that the optimum wavelength for growth of the electrothermal instability, under these conditions, is a few times greater than $(\frac{m_i}{m_e})^{\frac{1}{2}} a_{eo}$. For devices of fusion interest, this is a few centimetres or less, therefore, the above approximation is valid. We also know from the results quoted in the last chapter, that using a tensor electric conductivity model and including thermo electric effects, does not appreciably change the behaviour of the instability in question. For this reason, the stability analysis is performed assuming the electric conductivity to be scalar, and neglecting thermo electric terms.

2.1 STABILITY ANALYSIS OF AN ELECTROTHERMAL INSTABILITY WITH BREMSSTRAHLUNG RADIATION LOSS INCLUDED

The system considered is an infinite, fully ionized, two temperature, plasma in constant and uniform applied magnetic and electric fields in the same direction, with zero order uniform profiles for electron and ion temperatures as well as number density. It is assumed that the plasma is neutral in equilibrium and quasi-neutral when the perturbation is applied. The ion temperature is considered to remain unchanged throughout, because

any perturbation, with a wavelength of the order of magnitude of interest, would be quickly flattened because of the high thermal conductivity of the massive ions, perpendicular to the magnetic field. Only perturbations perpendicular to the magnetic field are considered, and, for simplicity, all plasma quantities are allowed to vary only along the direction of propagation of the perturbation.

The linear analysis is described in a rectangular coordinate system, the z axis along the equilibrium magnetic field $\underline{B}_o$, with the x and y axes orientated to comply with a right handed system of coordinates. All perturbed quantities are assumed to vary as $\exp(iK_x x + \alpha t)$, so the wave vector $\underline{K}$ of the perturbation is parallel to the x axis. Subscripts 0 and 1 represent equilibrium and perturbed quantities respectively.

Equations and a quantitative description

Maxwell's Vector Equations

The total electric and magnetic fields and current density can be written, when the perturbation is applied,

$$\underline{B} = \underline{B}_0 + \underline{B}_1, \qquad \underline{E} = \underline{E}_0 + \underline{E}_1, \qquad \underline{j} = \underline{j}_0 + \underline{j}_1$$

using Faraday's and Ampere's Laws as given in (1.1.4) and (1.1.6) applied to the equilibrium :

$$\nabla \times \underline{E}_0 = 0 \tag{2.1.1}$$

$$\nabla \times \underline{B}_0 = \frac{4\pi}{c} \underline{j}_0 \tag{2.1.2}$$

and when the perturbation is applied the perturbed fields are described by :

$$i\underline{K} \times \underline{E}_1 = -\frac{\alpha}{c} \underline{B}_1 \tag{2.1.3}$$

$$i\underline{K}x\underline{B}_1 = \frac{4\pi}{c}\underline{j}_1 \qquad (2.1.4)$$

Where the equilibrium equations (2.1.1) and (2.1.2) have been used to eliminate the zero order fields from the full equations, and where the following relation has been used :

$$\nabla x \sim i\underline{K}x$$

taking the divergence of equations (2.1.3) and (2.1.4) gives,

$$\underline{K}.\underline{B}_1 = 0 \qquad \text{i.e. } \underline{K} \text{ perpendicular to } \underline{B}_1,\ B_{x1} = 0$$

and

$$\underline{K}.\underline{j}_1 = 0 \qquad \underline{K} \text{ perpendicular to } \underline{j}_1,\ j_{x1} = 0$$

where the vector identity $\underline{a}.(\underline{a}x\underline{b}) = 0$ has been used.

Transport Equations

Pressure Balance

Equation (1.1.2) is written for the electrons and the ions. Writing $e_s = -e$ for the electrons and $e_s = e$ for the ions, $\underline{R}_s = \underline{R}$ for the electrons and $\underline{R}_s = -\underline{R}$ for the ions, that is total momentum is conserved, and adding the resulting equations one obtains,

$$m_e n \left(\frac{\partial \underline{V}_e}{\partial t} + (\underline{V}_e.\nabla)\underline{V}_e\right) + m_i n \left(\frac{\partial \underline{V}_i}{\partial t} + (\underline{V}_i.\nabla)\underline{V}_i\right) = -\nabla p - \nabla.\underline{\underline{\Pi}}_t - \frac{ne\underline{u}x\underline{B}}{c} \qquad (2.1.5)$$

where $p = p_e + p_i$, $\underline{\underline{\Pi}}_t = \underline{\underline{\Pi}}_e + \underline{\underline{\Pi}}_i$, $\underline{u} = \underline{V}_e - \underline{V}_i$.

It is more convenient in this work to use the centre of mass velocity defined as,

$$\underline{V} = \frac{m_e \underline{V}_e + m_i \underline{V}_i}{m_e + m_i} \qquad \text{where } n_e = n_i \text{ and } z = 1 \text{ has been used.}$$

In terms of the centre of mass velocity and the current density $\underline{j}$ given by,

$$\underline{j} = -ne(\underline{V}_e - \underline{V}_i) = -ne\underline{u} \tag{2.1.6}$$

$\underline{V}_e$ and $\underline{V}_i$ can be written :

$$\underline{V}_e = \underline{V} - \frac{b_e \underline{j}}{ne}$$

$$\underline{V}_i = \underline{V} + \frac{b_i \underline{j}}{ne} \tag{2.1.7}$$

Where $b_e = (1 + \frac{m_e}{m_i})^{-1} \sim 1$ and $b_i = \frac{m_e}{m_i} b_e$. Using (2.1.6) and (2.1.7), (2.1.5) becomes

$$-n \left((m_e + m_i) (\frac{\partial}{\partial t} + \underline{V}.\nabla)\underline{V} + m_e b_e \frac{\underline{j}}{ne}.\nabla(\frac{\underline{j}}{ne}) \right) = \nabla p + \nabla.\underline{\underline{\Pi}} - \frac{\underline{j} \times \underline{B}}{c} \tag{2.1.8}$$

Using the centre of mass velocity for the equilibrium equal to zero, $\underline{V}_o = 0$, $\underline{V}.\nabla\underline{V} = \underline{V}_1.\nabla\underline{V}_1$, is a second order term and can be neglected. Using the x-component of Ampere's law,

$$\frac{4\pi}{c} j_x = \frac{\partial B_z}{\partial y} - \frac{\partial B_y}{\partial z} = 0$$

so that,

$$\frac{\underline{j}}{ne} . \nabla(\frac{\underline{j}}{ne}) = \frac{j_x}{ne} \frac{\partial}{\partial x} (\frac{\underline{j}}{ne}) = 0 \tag{2.1.9}$$

Neglecting viscosity and using $m_e << m_i$ (2.1.8) becomes,

$$-nm_i \frac{\partial \underline{V}}{\partial t} = \nabla p - \frac{\underline{j} x \underline{B}}{c} \qquad (2.1.10)$$

In equilibrium, the above equation for pressure balance becomes :

$$\nabla p_o = \frac{\underline{j}_o x \underline{B}_o}{c} = 0 \qquad (2.1.11)$$

therefore, $\underline{j}_o$ is parallel to $\underline{B}_o$. However, Ampere's Law tells us

$$\nabla x \underline{B}_o = \frac{4\pi}{c} \underline{j}_o \qquad (2.1.12)$$

Tomimura shows how equations (2.1.11) and (2.1.12) can be simultaneously satisfied. One puts $\underline{B}_o(x) = \delta \underline{j}_o(x)$ where δ is a constant. A solution to (2.1.12) gives :

$$\begin{aligned} B_{ox} &= j_{ox} = 0 \\ j_{oy} &= j_o \sin \frac{4\pi x}{c\delta} \qquad B_{oy} = \delta j_{oy} \\ j_{oz} &= j_o \cos \frac{4\pi x}{c\delta} \qquad B_{oz} = \delta j_{oz} \end{aligned} \qquad (2.1.13)$$

where c = velocity of light.

Considering the direction of the applied electric field to be fixed, say in the z direction, then there exists a plane parallel to the y-z plane and passing through some value of x for which $\underline{B}_o$, everywhere parallel to $\underline{j}_o$, is parallel to $\underline{E}_o$. The coordinates have this point as origin and the z axis is parallel to $\underline{B}_o$.

In order that the steady state magnetic field may be considered

uniform and in the z direction, it is necessary for the wavelength of rotation of the magnetic field to be much larger than the wavelength of the perturbation, that is,

$$\frac{c\delta}{2} \gg \left(\frac{m_i}{m_e}\right)^{\frac{1}{2}} a_{eo} \tag{2.1.14}$$

The restriction this condition imposes on the range of validity of the model is quantified at the end of this section.

Looking at equations (2.1.13), the region of x for which this analysis is valid, is close to x = 0 so that, $\cos \frac{4\pi x}{c\delta} \sim 1$. Hence $\sin \frac{4\pi x}{c\delta} \sim 0$. From (2.1.13) it can be seen that,

$$B_{yo} \ll B_{zo}$$

Also in this region,

$$\nabla x \underline{E}_o \simeq 0$$

is obeyed. That is the unperturbed magnetic field changes very slowly compared to the growth time of the instability.

Having decided the analysis is only valid for a region of x where $B_{zo} \gg B_{yo}$, the linear analysis is now carried out neglecting B_y in the perturbation phase as well. The motivation for this analysis comes from the problems encountered in setting up a model to look at the time development of the electrothermal instability. These problems are not encountered in a linear analysis when the plasma is considered infinite. However, when boundary conditions have to be quantified, rotating fields introduce complications. If $\nabla x \underline{E}_o = 0$ is not identically satisfied in the numerical model, it would be impossible to separate the effects produced by an electrothermal instability from those produced by the evolution of

the non steady state. We wish to establish the importance of B_{y1}. This is done by comparing the results from linear analysis with and without B_{y1}. An efficient way of doing this is to use switch parameters. That is, multiply B_{y1}, and every equation containing B_{y1} which would not be used if B_{y1} were neglected, by α_1. The switch parameter α_1 is given a value of one if B_{y1} is included or zero if B_{y1} is neglected. If B_{y1} is neglected, the perturbed z-component of the electric field goes to zero.

Including the inertial term in equation (2.1.10) allows magnet-acoustic waves to exist. Multiplying the inertial term by the switch parameter α_2, which is set equal to either one or zero, allows us to examine the effects of neglecting deviations from $\nabla p = \frac{\underline{j} \times \underline{B}}{c}$.

Returning to equation (2.1.10), writing each quantity as a sum of equilibrium and perturbed parts, and neglecting terms of order higher than the first, we have, using $p = nk_B (T_e + T_i)$

$$-n_o m_i \alpha \underline{V}_1 \alpha_2 = i\underline{K}\, n_0 k_B T_{e1} + i\underline{K}\, n_1 k_B (T_{e0} + T_i) - \frac{\underline{j}_1 \times \underline{B}_0}{c} - \frac{\underline{j}_0 \times \underline{B}_1 \alpha_1}{c} \tag{2.1.15}$$

where the zero order equation (2.1.11) has been used, and all perturbed quantities are assumed to vary as $\exp(\alpha t + iK_x x)$ so that,

$$\frac{\partial f_1}{\partial t} \rightarrow \alpha f_1 \qquad \frac{\partial f_1}{\partial x} \rightarrow iK_x f_1 \tag{2.1.16}$$

where f_1 represents any first order parameter.

Taking the cross product of equation (2.1.15) with $\underline{K}$ ($K_x \hat{\underline{x}}$) yields

$$\underline{K}x\underline{V}_1 = 0 \qquad \text{i.e. } \underline{V}_1 \text{ is parallel to } \underline{K}$$

Ohm's Law

Equation (1.1.2) is again applied to the electrons and the ions with the same prescriptions as before, namely $e_e = -e$, $e_i = e$, $\underline{R}_e = \underline{R}$, and $\underline{R}_i = -\underline{R}$. The equation for the electrons is multiplied by $\frac{-e}{m_e}$, and that for the ions by $\frac{e}{m_i}$. $\underline{R}$ can be considered to be made up of two parts, a friction force $\underline{R}_u$, and a thermal force $\underline{R}_T$. $\underline{R}_u$ arises from the randomization of electron velocity due to collisions with ions, hence producing a decrease in the ordered velocity of the electrons with respect to the ions and a corresponding loss of momentum of the electrons which is given to the ions. $\underline{R}_T$ represents the thermal force brought about due to differences in frictional forces from different directions in space due to temperature gradients. The thermal force $\underline{R}_T$ is neglected here for reasons previously given.

The resulting equations are added together. Neglecting terms of order $\frac{m_e}{m_i}$, and using the relation $\underline{j}.\nabla = 0$ (as $j_x = 0$) equation (2.1.17) is obtained. After rearranging,

$$\underline{E} + \frac{\nabla p_e}{ne} + \frac{\underline{V}x\underline{B}}{c} - \frac{m_e}{e}\frac{\partial}{\partial t}\left(\frac{\underline{j}}{ne}\right) - \frac{m_e}{e}\underline{V}.\nabla\left(\frac{\underline{j}}{ne}\right) = \frac{\underline{R}_u}{ne} + \frac{\underline{j}x\underline{B}}{nec} \qquad (2.1.17)$$

$\underline{V}_e$ and $\underline{V}_i$ have also been written in terms of the centre of mass velocity $\underline{V}$. using equations (2.1.7) to produce (2.1.17). Before linearizing this equation, a comparison of the relative magnitude of some of the terms is made. First compare the magnitude of the fourth term on the left with that of the third. A dimensional analysis of Ampere's Law gives

$$\frac{B}{L} \sim \frac{4\pi}{c} j \qquad (2.1.18)$$

where L is the scale length over which fields vary significantly.

This is expected to be, approximately, the optimum wavelength for growth of the electrothermal instability. The expected growth rate gives the time over which things change significantly. Therefore, ∇ and $\frac{\partial}{\partial t}$ can be replaced by,

$$\nabla \sim \frac{1}{L} \sim \frac{eB_0}{m_i c} \left(\frac{m_i}{k_B T_{e0}}\right)^{\frac{1}{2}} = \frac{1}{a_{eo}} \left(\frac{m_e}{m_i}\right)^{\frac{1}{2}}$$

and (2.1.19)

$$\frac{\partial}{\partial t} \sim \omega \sim \frac{n_0 e^2}{m_i \sigma_o} = \frac{m_e}{m_i} \nu_{ei}$$

For the fields to interact with the plasma,

$$V \gtrsim \omega L \qquad (2.1.20)$$

Now comparing the magnitudes of the above mentioned terms gives

$$\frac{\text{4th term}}{\text{3rd term}} \sim \frac{\text{5th term}}{\text{3rd term}} \sim \frac{m_e}{m_i} \frac{2}{\beta_e}$$

Both the 4th and 5th terms are negligible provided $\beta_e >> \frac{2m_e}{m_i}$

where $\beta_e = \frac{8\pi n k_B T_e}{B_z^2}$

Neglecting the fourth and fifth terms, Ohm's Law for the plasma considered, becomes,

$$\underline{E} + \frac{\nabla p_e}{ne} + \frac{\underline{V} \times \underline{B}}{c} = \frac{\underline{j}}{\sigma} + \frac{\underline{j} \times \underline{B}}{nec} \qquad (2.1.21)$$

Where the Spitzer model for scalar conductivity [20] has been used that is,

$$\frac{R_{11}}{ne} = \frac{j}{\sigma} \tag{2.1.22}$$

All parameters in Ohm's Law can be expressed as a sum of equilibrium and perturbed parts. Using the second of the relations in (2.1.16), linearizing and neglecting terms of higher order than the first, the three components of Ohm's Law may be written :

$$\begin{aligned} E_{x1} + \frac{ik_x p_{e1}}{n_o e} &= \frac{j_{y1} B_{zo}}{n_o ec} - \frac{j_{zo} B_{y1} \alpha_1}{n_o ec} \\ E_{y1} - \frac{V_{x1} B_{zo}}{c} &= \frac{j_{y1}}{\sigma_o} \\ E_{z1} &= \frac{j_{z1}}{\sigma_o} - \frac{j_{zo} \sigma_1}{\sigma_o^2} \end{aligned} \tag{2.1.23}$$

Where the equilibrium Ohm's Law has been used in the z-component,

$$E_{zo} = \frac{j_{zo}}{\sigma_o} \tag{2.1.24}$$

The orientation of the vector quantities involved in this linear model are shown in Figure (2.1)

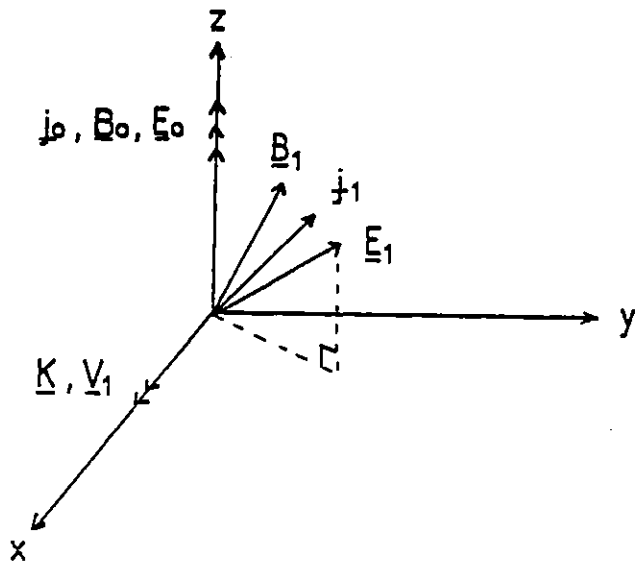

$\underline{B}_1$ and $\underline{j}_1$ are in y-z plane. $\underline{E}_1$ has components in x, y and z directions.

Figure 2.1

Although the x-component of the electric field exists, it does not enter any of the other equations but has been written here for completeness.

Heat balance equation for the electrons

As was discussed at the beginning of this chapter, the ion temperature is considered to remain uniform and constant always. It is only necessary to use the heat balance equation for the electrons. Consider the heat balance equation (1.1.3) applied to the electrons. Before splitting each parameter into its equilibrium and perturbed parts, this reads, again neglecting viscosity,

$$\frac{3}{2} nk_B \left(\frac{\partial T_e}{\partial t} + (\underline{V}_e.\nabla)\ T_e\right) + nk_B T_e\ \nabla.\underline{V}_e + \nabla.\underline{q}_e = Q_e \qquad (2.1.25)$$

Now $\nabla. = \left(\hat{x}\ \frac{\partial}{\partial x}\right).$

the unit vector $\hat{h}$ defining the direction of the total magnetic field is,

$$\hat{h} = \frac{\underline{B}}{|\underline{B}|} = \hat{z} + \frac{B_{1y}}{B_{oz}}\ \hat{y} \qquad (2.1.26)$$

where second order terms have been neglected.

So that

$$\nabla_\perp = \nabla - \nabla_{\parallel} = \hat{x}\ \frac{\partial}{\partial x} - \hat{h}\ \hat{h}.\nabla = \hat{x}\ \frac{\partial}{\partial x} \qquad (2.1.27)$$

Therefore, the only component of the heat flux, $\underline{q}_e$, of interest is that perpendicular to the total magnetic field. Furthermore, by analogy with $\underline{R}_e$, $\underline{q}_e$ is also made up of two parts, $\underline{q}_e = \underline{q}_{ue} + \underline{q}_{Te}$. When $\underline{R}_e$ was discussed previously, the thermal force was put to zero, that is, effectively, the current flow due to a temperature gradient (Seebeck effect) was neglected.

We correspondingly neglect the heat flow produced by the electric field driving the current. Hence,

$$\nabla.\underline{q}_e = \nabla_\perp.\ \underline{q}_e = \frac{\partial}{\partial x}\left(-\frac{K_e}{(1+\omega_e^2\tau_e^2)}\, k_B\, \frac{\partial T_e}{\partial x}\right) \tag{2.1.28}$$

where $\omega_e\tau_e$ is the electron cyclotron frequency multiplied by the electron-ion collision time. The coefficient of thermal conductivity K_e along the magnetic field is reduced by a factor $1/(1+\omega_e^2\tau_e^2)$ due to the inhibiting effect of the magnetic field on thermal conduction across the field. The expression for K_e is given later.

Q_e is the heat transferred to the electrons due to collisions with the ions. The electron velocities are randomized in collisions and the energy associated with their ordered velocity, $\underline{u} = \underline{V}_e - \underline{V}_i$, is converted into heat. The heat generated in the electrons is equal to the work from the frictional force on the electrons by the ions, $-\underline{R}_u.\underline{u}$. If $T_e > T_i$, heat is transferred from the electrons to the ions. Therefore the energy exchanged per unit volume per unit time from the electrons to the ions is,

$$Q_{ie} = 3\frac{m_e\, n}{m_i\, \tau_e} k_B\, (T_e - T_i) \tag{2.1.29}$$

where τ_e = collision time between electrons and ions. Neglecting the fraction of $-\underline{R}_u.\underline{u}$ acquired by the ions

$$Q_e = -\underline{R}_u.\underline{u} - Q_{ie}$$

$$Q_e = \frac{j^2}{\sigma} - 3\frac{m_e\, n\, k_B}{m_i\, \tau_e}\, (T_e - T_i) \tag{2.1.30}$$

Scalar electrical conductivity has been assumed.

Including Bremsstrahlung loss effects Q_e. The energy radiated per unit volume per unit time by the electrons is,

$$P_B = \beta_r n^2 T_e^{\frac{1}{2}}$$

where $$\beta_r = 8\sqrt{\frac{K_B \pi}{3m_e}} \frac{e^6}{m_e c^3 \hbar} \simeq 1.5 \times 10^{-27} \qquad (2.1.31)$$

is the Bremsstrahlung radiation coefficient[21]. So that Q_e in equation (2.1.25) is,

$$Q_e = \frac{j^2}{\sigma} - \frac{3m_e n k_B}{m_i \tau_e} (T_e - T_i) - \beta_r n^2 T_e^{\frac{1}{2}} \qquad (2.1.32)$$

The transport coefficients and parameters which will be employed frequently in this work are :

The electron thermal conductivity[22]

$$K_e = \frac{5}{2} \frac{n k_B T_e \tau_e}{m_e} \qquad (2.1.33)$$

the electric conductivity[22]

$$\sigma = \frac{ne^2 \tau_e}{m_e} \qquad (2.1.34)$$

the electron cyclotron frequency

$$\omega_e = \frac{eB}{m_e c} \qquad (2.1.35)$$

and the electron-ion collision time[23]

$$\tau_e = \frac{3m_e^{\frac{1}{2}} (k_B T_e)^{3/2}}{4(2\pi)^{\frac{1}{2}} ne^4 \log_e \Lambda} \tag{2.1.36}$$

Using relation (2.1.36) in relations (2.1.33) and (2.1.34) gives, respectively,

$$K_e = c^1 T_e^{5/2} \tag{2.1.37}$$

where $$c^1 = \frac{15 k_B^{5/2}}{8\sqrt{2\pi} m_e^{\frac{1}{2}} e^4 \log_e \Lambda} \simeq 1.04 \times 10^{10} \tag{2.1.38}$$

and $$\sigma = \alpha^1 T_e^{3/2} \tag{2.1.39}$$

where $$\alpha^1 = \frac{3k_B^{3/2}}{4\sqrt{2\pi} m_e^{\frac{1}{2}} e^2 \log_e \Lambda} \simeq 6.97 \times 10^6 \tag{2.1.40}$$

Returning to the heat balance equation (2.1.25), the electron velocity may be written in terms of the centre of mass velocity using the first of equations (2.1.7). We also use the fact that $jx = 0$ and $\nabla = \hat{\underline{x}} \frac{\partial}{\partial x}$. Using equations (2.1.28), (2.1.32) and (2.1.34) in equation (2.1.25) the heat balance equation for the electrons becomes

$$\frac{3}{2} nk_B \frac{\partial T_e}{\partial t} + \frac{3}{2} nk_B V_x \frac{\partial T_e}{\partial x} + nk_B T_e \frac{\partial V_x}{\partial x} = \frac{\partial}{\partial x} \left(\frac{K_e k_B}{(1+\omega_e^2 \tau_e^2)} \frac{\partial T_e}{\partial x} \right)$$

$$+ \frac{j^2}{\sigma} - \frac{3n^2 e^2 k_B (T_e - T_i)}{m_i \sigma} - \beta_r n^2 T_e^{\frac{1}{2}} \tag{2.1.41}$$

Writing each parameter as a sum of its equilibrium value and a perturbed part, using relations (2.1.16) and neglecting terms higher than first order, equation (2.1.41) becomes,

$$\frac{3}{2} n_o k_B \alpha T_{el} + ik_x n_o k_B T_{eo} V_{xl} = - \frac{k_x^2 K_{eo} k_B}{(1+\omega_{eo}^2 \tau_{eo}^2)} T_{el} + \frac{2 j_{zo} j_{zl}}{\sigma_o}$$

$$- \frac{3 n_o^2 e^2 k_B T_{eo}}{m_i \sigma_o} \left(\frac{T_{el}}{T_{eo}} + \frac{2n_l}{n_o} - \frac{2n_l}{n_o} \frac{T_i}{T_{eo}} \right)$$

$$- \left(\frac{\sigma_l}{\sigma_o} + \frac{1}{2} \frac{T_{el}}{T_{eo}} + \frac{2n_l}{n_o} \right) \beta_r n_o^2 T_{eo}^{\frac{1}{2}} \qquad (2.1.42)$$

Where the zero order heat balance equation has been used,

$$\frac{j_{zo}^2}{\sigma_o} = \frac{3 n_o^2 e^2 k_B (T_{eo} - T_i)}{m_i \sigma_o} + \beta_r n_o^2 T_{eo}^{\frac{1}{2}} \qquad (2.1.43)$$

This equation describes the steady state before the perturbation is applied. The Ohmic heating rate is balanced by the equipartition rate from the electrons to the ions and Bremsstrahlung radiation loss. The ions, therefore, act as a sink of energy in this model.

It should be noted here that in the perturbation phase the y-component of the current gives a negligible contribution to the perturbed Ohmic heating rate to first order. Also the perturbed Ohmic heating is a maximum where $\underline{j}_o \cdot \underline{j}_1$ is a maximum.

Continuity Equation

Starting with equation (1.1.1), it is a simple matter to obtain the perturbed continuity equation,

$$\alpha n_1 + ik_x n_o V_{xl} = 0 \qquad (2.1.44)$$

where the centre of mass velocity has been used to replace species velocity.

Having completely described both the steady and perturbed states of the plasma, we are now in a position to quantify the assumption of the wavelength of rotation of the steady-state fields being much larger than the optimum wavelength for growth of the electrothermal instability. Using equations (2.1.13) and (2.1.43) in relation (2.1.14) and after some algebra we find,

wavelength of rotation >> wavelength of instability

provided $$\frac{4\pi}{\beta_e}\left(\frac{T_{eo}}{3(T_{eo}-T_i)}\right)^{\frac{1}{2}} >> 1 \qquad (2.1.45)$$

where the Bremsstrahlung term has been neglected in the derivation of (2.1.45) for simplicity.

2.2 THE DISPERSION RELATION

Summary of Equations

The object of this exercise is to obtain an equation for the growth rate, α, as a fraction of wave number k_x, that is a dispersion equation.

The equations derived in the last section are summarised here to make it easier for the reader to follow the brief account of how the dispersion relation is obtained. Equations (2.1.3), (2.1.4), (2.1.15), (2.1.23) and (2.1.42) can be written,

Faraday's Law

$$ik_x E_{y1} = -\frac{\alpha}{c} B_{z1} \qquad (2.2.1)$$

$$ik_x E_{z1} = \frac{\alpha}{c} B_{y1} \tag{2.2.2}$$

Ampère's Law

$$ik_x B_{y1} = \frac{4\pi}{c} j_{z1} \alpha_1 \tag{2.2.3}$$

$$ik_x B_{z1} = -\frac{4\pi}{c} j_{y1} \tag{2.2.4}$$

Pressure Balance

$$-n_o m_i \alpha V_{x1} \alpha_2 = ik_x n_o k_B T_{e1} + ik_x n_1 k_B (T_{e0}+T_i) - \frac{j_{y1} B_{z0}}{c} + \frac{j_{z0} B_{y1}}{c} \tag{2.2.5}$$

Ohm's Law

$$E_{y1} - \frac{V_{x1} B_{z0}}{c} = \frac{j_{y1}}{\sigma_0} \tag{2.2.6}$$

$$E_{z1} = \frac{j_{z1}}{\sigma_o} - \frac{j_{z0} \sigma_1}{\sigma_0^2} \tag{2.2.7}$$

Electron heat balance

$$\frac{3}{2} n_o k_B \alpha T_{e1} + ik_x n_o k_B T_{e0} V_{x1} = -\frac{k_x^2 k_{e0} k_B}{(1+\omega_{e0}^2 \tau_{e0}^2)} T_{e1} + \frac{2 j_{z0} j_{z1}}{\sigma_0} - \frac{3 n_o^2 e^2 k_B T_{e0}}{m_i \sigma_0} \left(\frac{T_{e1}}{T_{e0}} + \frac{2n_1}{n_0} - \frac{2n_1}{n_0} \frac{T_i}{T_{e0}}\right) - \beta_r n_o^2 T_{e0}^{\frac{1}{2}} \left(\frac{\sigma_1}{\sigma_0} + \frac{1}{2} \frac{T_{e1}}{T_{e0}} + \frac{2n_1}{n_0}\right) \tag{2.2.8}$$

Continuity Equation

$$\alpha n_1 + ik_x n_o V_{x1} = 0 \tag{2.2.9}$$

It is also necessary to use an expression for $\frac{\sigma_1}{\sigma_0}$. From (2.1.39)

$$\frac{\sigma_1}{\sigma_0} = \frac{3}{2}\frac{T_{e1}}{T_{e0}} \tag{2.2.10}$$

Equation (2.2.1) is used as an expression for B_{z1}. Using this in equation (2.2.4) gives a relation between E_{y1} and j_{y1}, which is used in equation (2.2.6) to produce an expression for j_{y1} in terms of V_{x1}. This expression is used in equation (2.2.5).

Equation (2.2.2) gives B_{y1} in terms of E_{z1}, then eliminating B_{y1} from equation (2.2.3) gives E_{z1} in terms of j_{z1}. Using this equation in equation (2.2.7) gives j_{z1} in terms of $\frac{\sigma_1}{\sigma_0}$ (and hence T_{e1}/T_{e0}). This is substituted in equation (2.2.3) to give B_{y1} as a function of T_{e1}. This expression is used in equation (2.2.5). Now n_1 is written in terms of V_{x1} from equation (2.2.9), therefore equation (2.2.5) becomes an equation with T_{e1} and V_{x1} as the only perturbed quantities. That is,

$$ik_x V_{x1}\left[n_o m_i \alpha \alpha_2 + \frac{n_o k_B (T_{e0}+T_i) k_x^2}{\alpha} + \frac{\sigma_0 B_{z0}^2}{c^2\left(1+\frac{4\pi\sigma_0\alpha}{c^2k_x^2}\right)}\right]$$

$$= T_{e1}\left[k_x^2 n_0 k_B - \frac{4\pi}{c^2}\frac{9}{2}\frac{n_0^2 e^2 k_B (1-T_i/T_{e0})\alpha_1}{m_i\left(1+\frac{4\pi\sigma_0\alpha\alpha_1}{c^2k_x^2}\right)}\right.$$

$$\left. - \frac{3}{2}\frac{\beta_r n_0^2 T_{e0}^{-\frac{1}{2}} 4\pi\sigma_0\alpha_1}{c^2\left(1+\frac{4\pi\sigma_0\alpha\alpha_1}{c^2k_x^2}\right)}\right] \tag{2.2.11}$$

where the equilibrium equation (2.1.43) has been used.

Another equation in terms of V_{xl} and T_{el} is obtained from equation (2.2.8). Using an expression for j_{zl} in terms of $\frac{\sigma_1}{\sigma_0}$ $(T_{el}/T_{e0}$ using relation 2.2.10), derived as explained previously, and using equation (2.2.9) to eliminate n_1 from equation (2.2.8), the following equation is obtained after rearranging,

$$ik_x V_{xl} \left[- n_o k_B T_{e0} + \frac{6n_o^2 e^2 k_B (T_{e0}-T_i)}{m_i \sigma_o \alpha} + \frac{2\beta_r n_o^2 T_{e0}^{\frac{1}{2}}}{\alpha} \right]$$

$$= T_{el} \left[\frac{3}{2} n_o k_B \alpha + \frac{k_x^2 k_{e0} k_B}{(1+\omega_{e0}^2 \tau_{e0}^2)} + \frac{3n_o^2 e^2 k_B}{m_i \sigma_o} - \frac{9n_o^2 e^2 k_B (1-T_i/T_{e0})}{m_i \sigma_o \left(1+\frac{4\pi\sigma_o\alpha\alpha_1}{c^2 k_x^2}\right)} \right.$$

$$\left. + 2\beta_r n_o^2 T_{e0}^{-\frac{1}{2}} - \frac{3\beta_r n_o^2 T_{e0}^{-\frac{1}{2}}}{\left(1+\frac{4\pi\sigma_o\alpha\alpha_1}{c^2 k_x^2}\right)} \right] \qquad (2.2.12)$$

This leaves two simultaneous equations in V_{xl} and T_{el} which are solved to obtain a dispersion equation. The dispersion equation is written in dimensionless form, using the following dimensionless quantities.

$$x = \frac{m_i \sigma_o \alpha}{n_o e^2} \qquad y = \left(\frac{k_B T_{e0}}{m_i}\right)\left(\frac{m_i c}{eB_{z0}}\right)^2 k_x^2 = a_{e0}^2 \frac{m_i}{m_e} k_x^2$$

where a_{e0} = electron Larmor radius at equilibrium

$$\pi_e = \frac{8\pi n_o k_B T_{e0}}{B_{z0}^2} \qquad \varepsilon = \frac{3n_o c^2}{8\pi\sigma_o K_{e0}}$$

$$R = \frac{\beta_r m_i \sigma_o}{k_B T_{e0}^{\frac{1}{2}} e^2} \qquad f_o = 1 + \omega_{e0}^2 \tau_{e0}^2$$

$$T = \frac{T_i}{T_{e0}} \qquad W = \omega_{e0}\tau_{e0} = \frac{\sigma_o B_{zo}}{n_o e c} \qquad (2.2.13)$$

With the quantities defined in (2.2.13), the equation describing the

dimensionless growth rate, x (or damping rate if x is negative), as a function of the square of the dimensionless wave number y becomes,

$$\alpha_1\alpha_2x^5 + 2\alpha_2x^4\left[\frac{y}{\pi_e}\left(1 + \alpha_1\left(1+\frac{1}{\varepsilon f_o}\right)\right) + \alpha_1\left(1 + \frac{2R}{3}\right)\right]$$

$$+ x^3\left[\frac{4y^2}{\pi_e^2}\left(\frac{(\alpha_1+\alpha_2)}{\varepsilon f_o} + \alpha_2\right) + y\left(W^2\alpha_1\left(\frac{5}{3} + T + \frac{2}{\pi_e}\right)\right.\right.$$

$$\left.\left. + \frac{4}{\pi_e}\alpha_2(\alpha_1 - 2 + 3T + \frac{R}{3}(2\alpha_1-1))\right)\right]$$

$$+ x^2\left[\frac{8y^3\alpha_2}{\pi_e^3\varepsilon f_o} + \frac{2y^2}{\pi_e}\left(W^2\left(\frac{(5+\alpha_1)}{3} + T(1+\alpha_1) + \frac{2}{\pi_e} + \frac{\alpha_1}{\varepsilon f_o}\left(1+T+\frac{2}{\pi_e}\right)\right)\right.\right.$$

$$\left.\left. + \frac{4}{\pi_e}\alpha_2\left(3T-2-\frac{R}{3}\right)\right) + yW^2\alpha_1\left(2R\left(\frac{4}{3\pi_e} + \frac{2}{3}T - \frac{1}{2}\right) + \left(\frac{4}{\pi_e} -5+9T\right)\right)\right]$$

$$+ x\left[y^3\frac{4W^2}{\pi_e^2}\left(\frac{1}{\varepsilon f_o}(1 + T + \alpha_1(1+T) + \frac{2}{\pi_e}) + \frac{5}{3} + T\right)\right.$$

$$+ y^2\frac{2W^2}{\pi_e}\left(\frac{4}{\pi_e}(3T - 2 - \frac{R}{3}) + 3T(2T+3\alpha_1+2) - 8 - 5\alpha_1 + R(\frac{2}{3}T(2\alpha_1-1)-2-\alpha_1)\right)$$

$$\left. + 2\alpha_1 y W^2 (3(1-T) + R)^2\right]$$

$$+ y^4\frac{8W^2(1+T)}{\pi_e^3\varepsilon f_o} + y^3\frac{8W^2}{\pi_e^2}(3T^2 + 3T - 4 - R\frac{(1+T)}{3})$$

$$+ y^2\frac{4W^2}{\pi_e}\alpha_1(3(1-T) + R)^2 = 0 \qquad (2.2.14)$$

Putting R = 0, and $\alpha_1 = \alpha_2 = 1$, in the above equation gives the same dispersion relation as obtained by Tomimura[3], as indeed it should.

2.3 RESULTS

Analysis of Dispersion equation with Bremsstrahlung radiation loss

A detailed analysis of the behaviour of electrothermal instabilities in the linear regime can be found in references [2, 3]. It is only necessary here to observe the specific effects of Bremsstrahlung radiation loss. α_1 and α_2 are set equal to one, therefore the inclusion of Bremsstrahlung is the only difference between this analysis and that in references [2, 3].

Condition for onset of non-convective unstable mode

The condition for onset of the non convective (real x only) unstable mode can be found by putting, x = 0, in equation (2.2.14). This determines the condition for onset because x is real at x = 0 and, $\frac{dx}{dy} < 0$ at x = 0[2]. Multiplying through by $\frac{\pi_e{}^3 \varepsilon f_o}{8W^2(1+T)y^2}$ gives,

$$y^2 + \frac{\pi_e \varepsilon f_o}{(1+T)}\left((3T^2+3T-4) - R\frac{(1+T)}{3}\right) y$$

$$+ \frac{\pi_e{}^2 \varepsilon f_o}{2(1+T)}\left(3(1-T)\ (3(1-T) + 2R) + R^2\right) = 0 \qquad (2.3.1)$$

which is of the form,

$$y^2 + by + c = 0 \qquad (2.3.2)$$

with solution

$$y = \frac{-b}{2} \pm \frac{\sqrt{b^2-4c}}{2}$$

Hence, for real and positive y (y is proportional to $k_x{}^2$), two conditions

are required. These are :

$$3T^2 + 3T - 4 - R\frac{(1+T)}{3} < 0$$

and (2.3.3)

$$\frac{\varepsilon f_o}{(1+T)} \geq \frac{2(9(1-T)^2 + 6R(1-T) + R^2)}{(3T^2 + 3T - 4 - R\frac{(1+T)}{3})^2}$$

By putting $t = \frac{1}{T}$, and $R = Bt$, so that $B = \frac{\beta_r\, m_i\, \alpha^1\, T_i}{k_B e^2}$, the first of the above conditions becomes,

$$3Bt^3 + (12 + B)t^2 - 9t - 9 > 0 \qquad (2.3.4)$$

and the second becomes,

$$\varepsilon^{\frac{1}{2}} \geq \frac{(18t(t-1)^2 + 12Bt^3\,(t-1) + 2Bt^4)^{\frac{1}{2}}\,(t+1)^{\frac{1}{2}}}{(4t^2 - 3t - 3 + Bt^2(t+\frac{1}{3}))(1 + \omega_{eo}{}^2\tau_{eo}{}^2)^{\frac{1}{2}}} \qquad (2.3.5)$$

If $B = 0$ in the last two relations, the necessary and sufficient conditions for onset of a non-convective unstable mode, as obtained by Tomimura and Haines[2], are recovered. These are :

$$4t^2 - 3t - 3 > 0 \quad \text{leading to } t > 1.3187 \qquad (2.3.6)$$

and

$$(\frac{\varepsilon}{18})^{\frac{1}{2}} \geq \frac{(t-1)\,(t(t+1))^{\frac{1}{2}}}{(4t^2 - 3t - 3)(1 + \omega_{e0}{}^2\tau_{eo}{}^2)^{\frac{1}{2}}}$$

Comparing the first of (2.3.6) with (2.3.4), it is apparent that the inclusion of Bremsstrahlung radiation loss causes the plasma to be more unstable to electrothermal instabilities, because it reduces the value of t ($t = \frac{T_{eo}}{T_i}$) above which the unstable mode is present. The higher the value of B (B = constant T_i), the lower the threshold value of t

above which the plasma is unstable. At B = 1.5 it can be shown that the threshold value of t is t = 1.0. As the only source of energy for the ions is from equipartition in this model, t must be greater than one, but t must be less than one to be stable (at B = 1.5). Therefore $T_i = 1.3 \times 10^9 K$ is the maximum deuterium temperature attainable by Joule heating in the presence of pure Bremsstrahlung in a homogeneous, stable plasma.

Figure (2.3) shows a plot of x against y from equation (2.2.14) for $\pi_e = 0.02267$, $\epsilon = 2.259 \times 10^{-11}$, $\omega\tau = 1.536 \times 10^6$, $T_{eo} = 2 \times 10^8 k$, $T_i = 10^8 k$ (proportional to k_x^2). From the graph, there exists a purely growing mode for y greater than about 10^{-2}. For smaller values of y ($10^{-2.2} > y > 10^{-3}$) there is a growing mode with non zero values of Imag x. The effect of including Bremsstrahlung radiation loss is to increase slightly the growth rate of the purely growing mode (for $y > 10^{-1.9}$). The purely growing mode is of greater interest for two reasons. For conditions relevant to present day Tokamaks (high $\omega_e\tau_e$) the growth rate of the non-convective mode is much greater than that of the convective mode. Also the wavelengths of the non-convective modes are smaller ($\sim$ centimetres) than that of their convective counterparts.

Physically, the inclusion of Bremsstrahlung radiation loss increases the growth rate because of the $n^2 T_e^{\frac{1}{2}}$ dependence of the radiation loss term. Substituting (2.2.9) into (2.2.11) gives, with $\alpha_1 = \alpha_2 = 1$,

$$n_1 = \frac{-\frac{n_o}{\alpha} T_{el} \left[k_x^2 n_o k_B - \frac{4\pi}{c^2} \frac{9}{2} \frac{n_o^2 e^2 k_B (1-T_i/T_{eo})}{m_i (1+\frac{4\pi\sigma_o\alpha}{c^2 k_x^2})} - \frac{3}{2} \frac{\beta_r n_o^2 T_{eo}^{-\frac{1}{2}} 4\pi\sigma_o}{c^2 (1+\frac{4\pi\sigma_o\alpha}{c^2 k_x^2})} \right]}{\left[n_o m_i \alpha + \frac{n_o k_B (T_{eo}+T_i) k_x^2}{\alpha} + \frac{\sigma_o B_{zo}^2}{c (1+\frac{4\pi\sigma_o\alpha}{c^2 k_x^2})} \right]} \qquad (2.3.7)$$

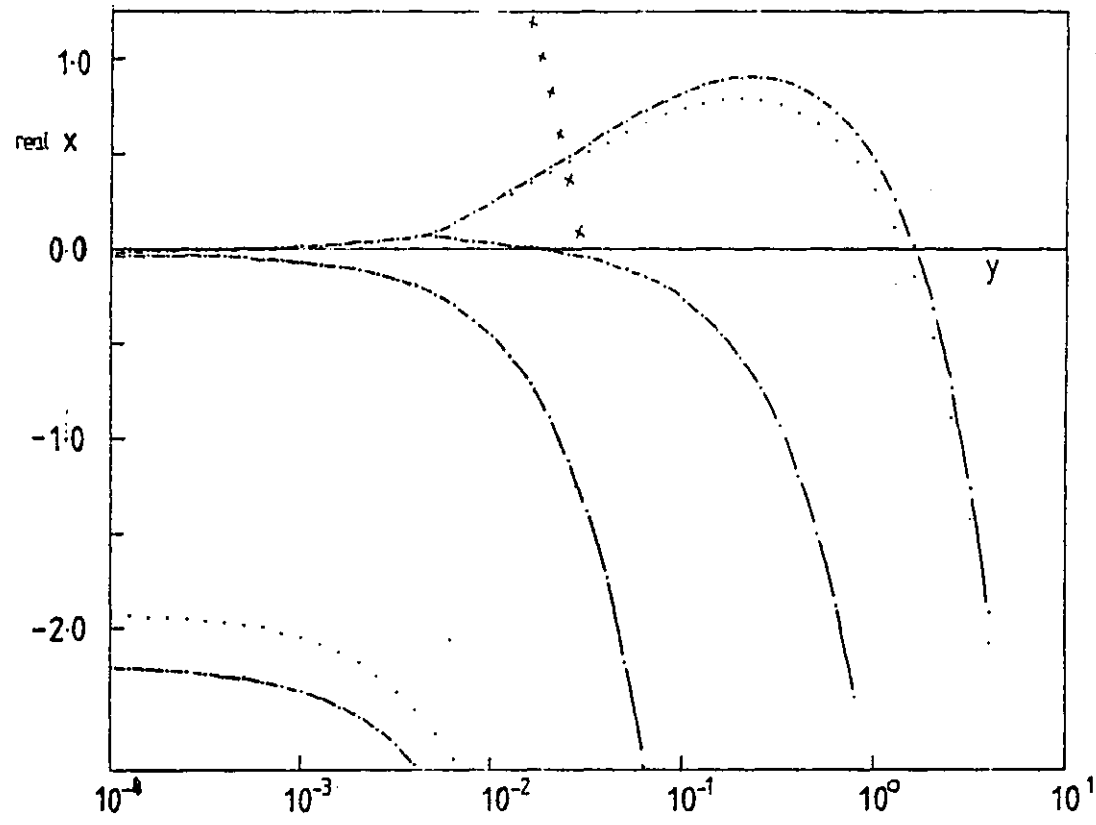

a) Plots of dimensionless growth rate real x against the square of the dimensionless wavenumber y.

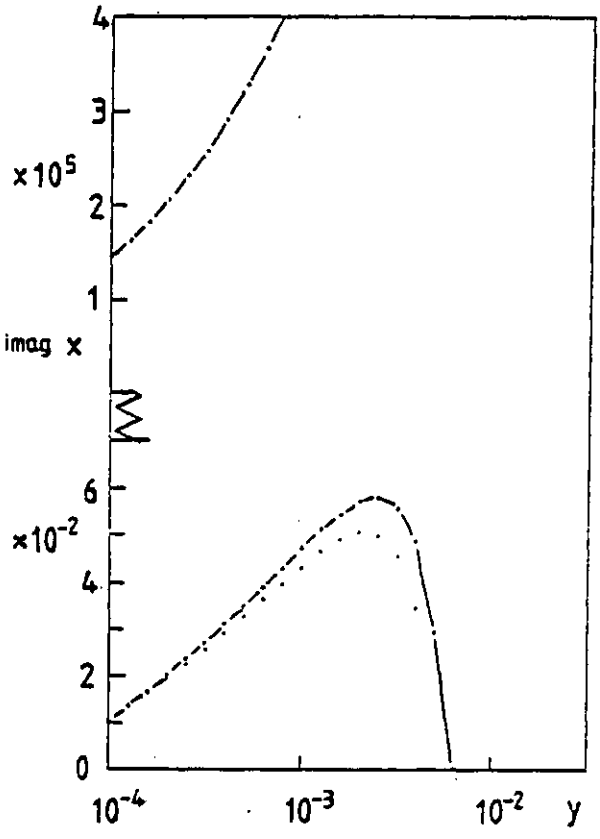

b) Plot of imaginary x against y

Key

._._. Bremsstrahlung radiation loss included

..... Changes to the results produced by neglecting Bremsstrahlung

In Figure 2.3a, above the curve made up of crosses, xxx, n_1 and T_{el} are of the same sign. Under this curve n_1 and T_{el} are of opposite sign.

Figures 2.3

$\pi_e = 0.02267$, $\varepsilon = 2.259 \times 10^{-11}$, $\omega_e \tau_e = 1.536 \times 10^{6}$

$T_{eo} = 2 \times 10^{8}$K, $T_i = 10^{8}$K

Each term in the square brackets of the denominator in (2.3.7) is positive, for positive α provided $T_{eo} > T_i$. The condition for n_1 to be of opposite sign to T_{e1}, in the region of y for which the growth rate with Bremsstrahlung is greater than that without is,

$$k_x^2 n_o k_B > \frac{4\pi}{c^2}\frac{9}{2}\frac{n_o^2 e^2 k_B}{m_i}\quad\frac{(1-T_i/T_{eo})}{(1+\frac{4\pi\sigma_o\alpha}{c^2k_x^2})}+\frac{3}{2}\frac{\beta_r n_o^2 T_{eo}^{-\frac{1}{2}}4\pi\sigma_o}{c^2(1+\frac{4\pi\sigma_o\alpha}{c^2k_x^2})} \qquad (2.3.8)$$

or in terms of x and y,

$$x > \frac{9}{2}(1 - T_i/T_{eo}) + \frac{3}{2}R - \frac{2y}{\pi_e} \qquad (2.3.9)$$

This curve is also shown in Figure(2.3a). For real positive values of x above this curve (for $10^{0.2} > y > 10^{-1.53}$) the increased growth rate is produced by the following mechanism. The perturbed temperature peaks coincide with the density troughs. Therefore the stronger dependence of the radiation loss term on density than on temperature ($n^2T_e^{\frac{1}{2}}$) leads to a decrease in radiation loss rate in the temperature peaks. The converse argument applies to the temperature troughs. Hence the Bremsstrahlung term helps to drive the instability.

For lower values of y the growth rate is increased but condition (2.3.9) does not hold. For the same steady state values of density and temperature, a higher electric field is required to balance the extra Bremsstrahlung loss term. Hence the perturbed Ohmic heating rate is higher leading to a slightly increased growth rate, because the corresponding change in the Bremsstrahlung loss does not quite cancel the effect of the extra Ohmic heating.

We conclude this section by noting the inclusion of Bremsstrahlung only has a significant effect at very high temperatures because the Bremsstrahlung coefficient is very small. Its ability to enhance the

growth rate of the instability is a consequence of its $n^2T_e^{\frac{1}{2}}$ dependence, and is primarily brought about because of the inclusion of ion motion which allows the density to change. Impurity radiation, which represents the most significant fraction of radiation loss in present day devices, would also be destabilising. Impurity radiation from free-free and free-bound transitions could have an even greater destabilising effect because the density and electron temperature dependence goes as $n^2T_e^{\gamma}$, where $\gamma \sim \frac{-3}{2}$. The value of γ depends upon the temperature, and for temperatures above 10^8K $\gamma = \frac{1}{2}$[24].

2.4 RESULTS

The Effect of neglecting the y-component of the Magnetic Field

The effect of neglecting the y-component of the magnetic field on the linear behaviour of the electrothermal instability may be assessed by putting $\alpha_1 = 0$, $\alpha_2 = 1$ in the dispersion relation, equation (2.2.14). The equation reduces to a quartic in x and cubic in y,

$$x^4 + 2x^3 \left[\frac{y}{\pi_e} \left(1 + \frac{1}{\varepsilon f_o}\right) + 3T - 2 - \frac{R}{3} \right]$$

$$+ x^2 \left[\frac{4y^2}{\pi_e^2 \varepsilon f_o} + y\left(W^2\left(\frac{5}{3} + T + \frac{2}{\pi_e}\right) + \frac{4}{\pi_e}\left(3T - 2 - \frac{R}{3}\right)\right) \right] \qquad (2.4.1)$$

$$+ x \left[\frac{2y^2W^2}{\pi_e} \left(\frac{1}{\varepsilon f_o}\left(1 + T + \frac{2}{\pi_e}\right) + \frac{5}{3} + T\right) + 2yW^2 \left(\frac{2}{\pi_e}\left(3T - 2 - \frac{R}{3}\right)\right.\right.$$

$$\left.\left. + 3T(1+T) - 4 - R\left(1+\frac{T}{3}\right)\right) \right] + \frac{4W^2(1+T)y^3}{\pi_e^2 \varepsilon f_o} + \frac{4W^2y^2}{\pi_e}\left(3T^2+3T-4-R\left(1+\frac{T}{3}\right)\right) = 0$$

The only condition for onset of the non-convective unstable mode is now,

$$3Bt^3 + (12 + B)\, t^2 - 9t - 9 > 0 \qquad (2.4.2)$$

This is identical to one of the requirements for onset obtained in the last section. However, there is not a condition on ε as there was before ($\varepsilon \propto n_o/T_{eo}^4$).

Figure 2.4 is a plot of x against y for both equations (2.4.1) and (2.2.14) clearly showing the consequences of neglecting the y-component of the magnetic field. The purely damped mode, (labelled 1 on Figure 2.4a)) does not exist when B_y is neglected. The damped magneto acoustic mode (labelled 2 on Figure 2.4a) and b)) is virtually unaffected by neglecting B_y. This mode is non-dispersive, ($\text{imag}x/y^{\frac{1}{2}}$ = constant) with much larger values of $|x|$ than any other mode. The mode labelled 3 in figure 2.4 is purely damped for all values of y when B_{yl} is neglected, but when B_{yl} is included this mode has values of y for which it is growing and is convective (non-zero values of imag x).

The most important mode for our purposes is the purely growing mode (labelled 4 in Figure 2.4) representing an electrothermal instability. This root is considerably changed by neglecting B_{yl} at long wavelengths (small y). If B_{yl} is included an optimum wavelength for growth exists. Short wavelengths (large y) are damped due to perpendicular electron thermal conduction, while long wavelengths are more slowly growing because of Faraday's law, which acts to reduce the perturbed current. If B_{yl} is neglected there is no such reduction in the z-component of the perturbed current; the Ohmic heating rate is larger and hence the growth rate increased. The behaviour of the z-component of the current is more important than that of the y-component, because the contribution to the Ohmic heating by j_y is second order and therefore negligible. The amount by which j_{zl} is reduced depends upon the wavelength and can be found using equation (2.2.2) as an expression for B_{yl}, substituting this into equation (2.2.3), giving E_{zl} in terms of j_{zl}, and finally using this

(a)

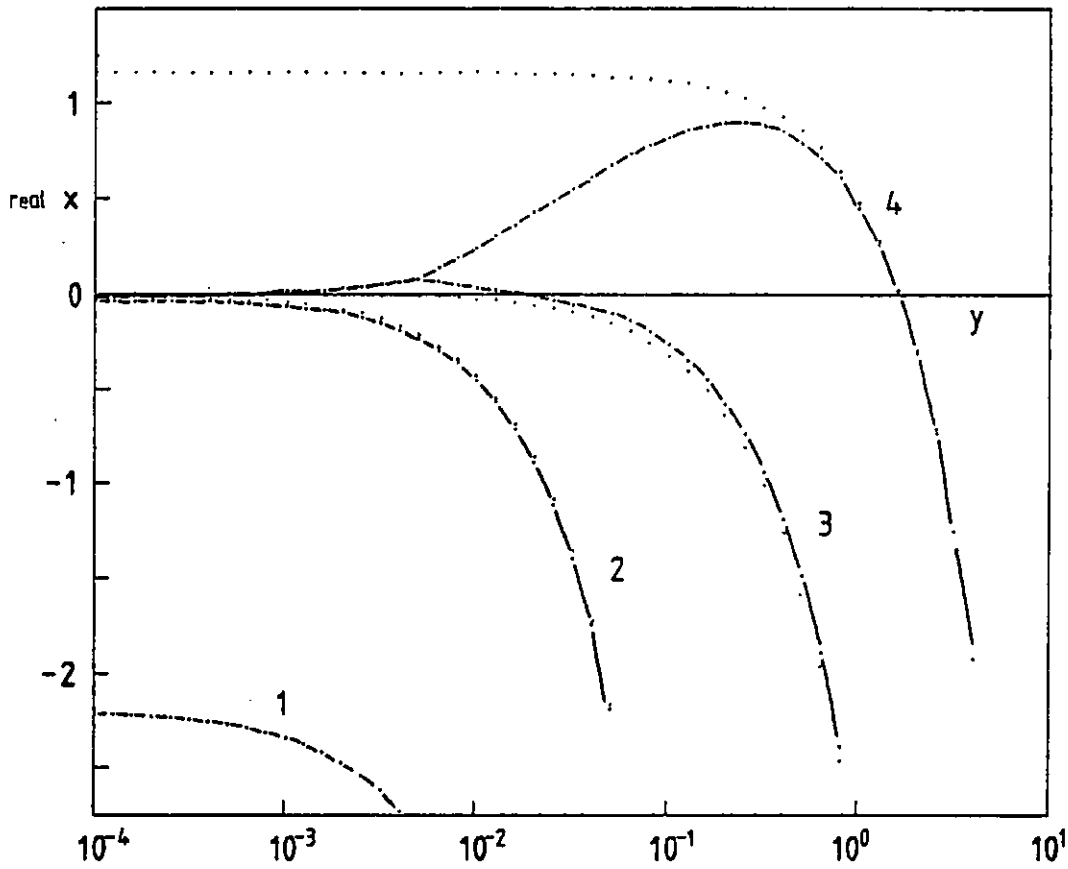

(b)

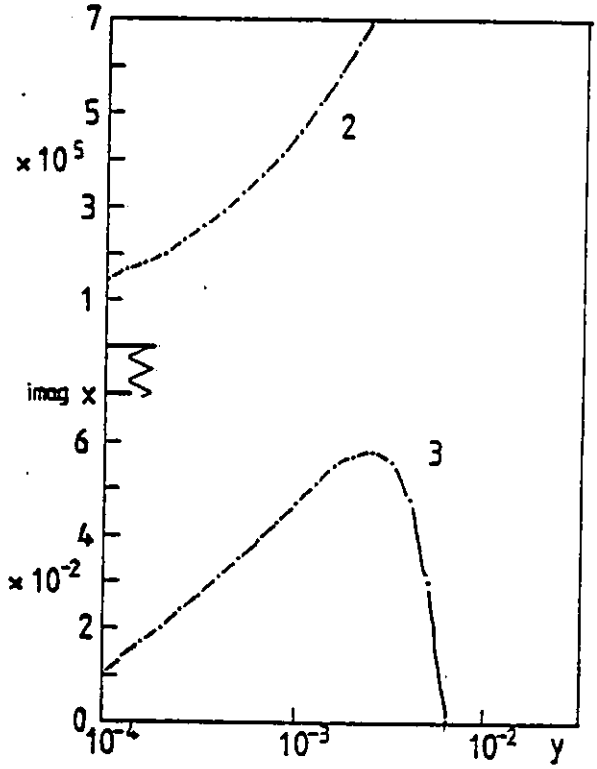

Key

·-·-· B_{yl} included

····· Changes to the results introduced by neglecting B_{yl}

Figures 2.4

The consequences of neglecting B_{yl}

Plots of x against y for $\pi_e = 0.02267$, $\varepsilon = 2.259\times10^{-11}$ $\omega_e\tau_e = 1.536\times10^{6}$, $T_{eo} = 2\times10^{8}$K, $T_i = 10^{8}$K. Bremsstrahlung loss included.

equation to eliminate E_{z1} from equation (2.2.7),

$$j_{z1} = j_{zo} \frac{\sigma_1}{\sigma_o} \left[1 + \frac{4\pi\sigma_o\alpha\alpha_1}{c^2k_x^2} \right]^{-1} \tag{2.4.3}$$

The effects of including B_{y1} are negligibly small if,

$$\frac{4\pi\sigma_o\alpha}{c^2k_x^2} << 1 \tag{2.4.4}$$

or, in terms of dimensionless quantities

$$\frac{\pi_e x}{2y} << 1 \tag{2.4.5}$$

The reduced Ohmic heating rate is not the only reason for the difference in growth rate. The phase angle between the perturbed number density n_1 and the perturbed electron temperature T_{e1} can be found using equation (2.2.9) as an expression for n_1 and substituting this into equation (2.2.11) to give,

$$n_1 = \frac{-T_{e1} \frac{n_o}{\alpha} \left[k_x^2 n_o k_B - \frac{4\pi}{c^2} \frac{9}{2} \frac{n_o^2 e^2 k_B (1-T_i/T_{eo}) \alpha_1}{m_i (1+\frac{4\pi\sigma_o\alpha\alpha_1}{c^2k_x^2})} - \frac{3}{2} \frac{\beta_r n_o^2 T_{eo}^{-\frac{1}{2}} 4\pi\sigma_o\alpha_1}{c^2 (1+\frac{4\pi\sigma_o\alpha\alpha_1}{c^2k_x^2})} \right]}{\left[n_o m_i \alpha\alpha_2 + \frac{n_o k_B (T_{eo}+T_i) k_x^2}{\alpha} + \frac{\sigma_o B_o^2}{c (1+\frac{4\pi\sigma_o\alpha}{c^2k_x^2})} \right]} \tag{2.4.6}$$

In the wavelength range for which the growth rate of the purely growing mode with B_{y1} included is much less than the growth rate without, the sign of the upper square bracket is negative if $\alpha_1 = 1$ and positive if $\alpha_1 = 0$. The sign of the lower square bracket is always positive. Therefore

n_1 and T_{el} are in phase if $\alpha_1 = 1$ (B_{y1} included) and 180° out of phase if $\alpha_1 = 0$. The dominant energy loss mechanism in this region is equipartition from the electrons to the ions, as can be shown by comparing the size of the terms in equation (2.2.8). Equipartition goes as $n^2/T_e^{3/2}$. If n_1 and T_{el} are 180° out of phase this term is smaller in the temperature peaks than it is if n_1 and T_{el} are in phase. Conversely, it is larger in the temperature troughs. This means the equipartition term tends to increase the growth rate for the case with $\alpha_1 = 0$ above that for the case with $\alpha_1 = 1$, by making the energy loss comparatively lower in the temperature peaks and higher in the temperature troughs.

We may conclude this section by stating the effect of the y-component of the magnetic field on the linear behaviour of the electrothermal instability is negligible provided the initial conditions and the wavelengths considered are such that relation (2.4.5) is obeyed.

In section (2.1) we established the zero order y-component of the magnetic field is very small and should be neglected in a numerical model to follow the evolution of the electrothermal instability. To include the perturbed y-component of the magnetic field only would therefore necessitate separating zero order and perturbed components of B_y and all other quantities affected by this component of $\underline{B}$, and solving for the perturbed quantities only. Clearly this is not a viable proposition. Having shown the y-component of $\underline{B}$ has a negligible effect under certain circumstances (2.4.5), we can circumvent this problem by neglecting B_y totally in the numerical model.

2.5 RESULTS

The effect of neglecting deviations from $\nabla p = \frac{j \times B}{c}$

The consequences of ignoring the inertial term on the linear behaviour of the electrothermal instability may be determined by putting $\alpha_2 = 0$ ($\alpha_1 = 0$) in the dispersion relation, equation (2.2.14), and comparing this to the dispersion relation obtained in the last section, equation (2.4.1). We shall not compare the two curves with $\alpha_1 = \alpha_2 = 1$ and $\alpha_1 = 1$, $\alpha_2 = 0$, because this work is, for the most part, concerned with conditions such that the y-component of the magnetic field may be neglected. The dispersion relation obtained with $\alpha_1 = \alpha_2 = 0$ reduces to a quadratic in x and y, namely,

$$x^2 \left[1 + \frac{\pi_e T}{2} + \frac{5}{3} \pi_e \right] + xy \left[\frac{5}{3} + \frac{(1+T)}{\varepsilon f_o} + T + \frac{2}{\pi_e \varepsilon f_o} \right]$$

$$+ x \left[3\pi_e T(1+T) - 4\pi_e - 4 + 6T - R \left(\frac{2}{3} + \frac{\pi_e T}{3} + \pi_e \right) \right]$$

$$+ y^2 \frac{2(1+T)}{\pi_e \varepsilon f_o} + y \left(6T^2 + 6T - 8 - 2R\left(1+\frac{T}{3}\right) \right) = 0 \qquad (2.5.1)$$

It can be seen by inspection of equation (2.5.1) that the condition for onset of the electrothermal instability does not differ from that obtained in the last section.

Figure (2.5) is again a plot of x against y for both equations (2.5.1) and (2.4.1) with $T_i = 10^8$K, $T_{eo} = 2 \times 10^8$K, $\omega_e \tau_e = 1.54 \times 10^6$, $\pi_e = 2.27 \times 10^{-2}$, $R = 0.22$ and $\varepsilon = 2.259 \times 10^{-11}$. The most important point to notice, from the point of view of this problem, is the neglect of the initial term has a negligible effect on the behaviour of the electrothermal mode (labelled 1 in Figure 2.5). The growth rate of this mode without the inertial term is very nearly the same as that with

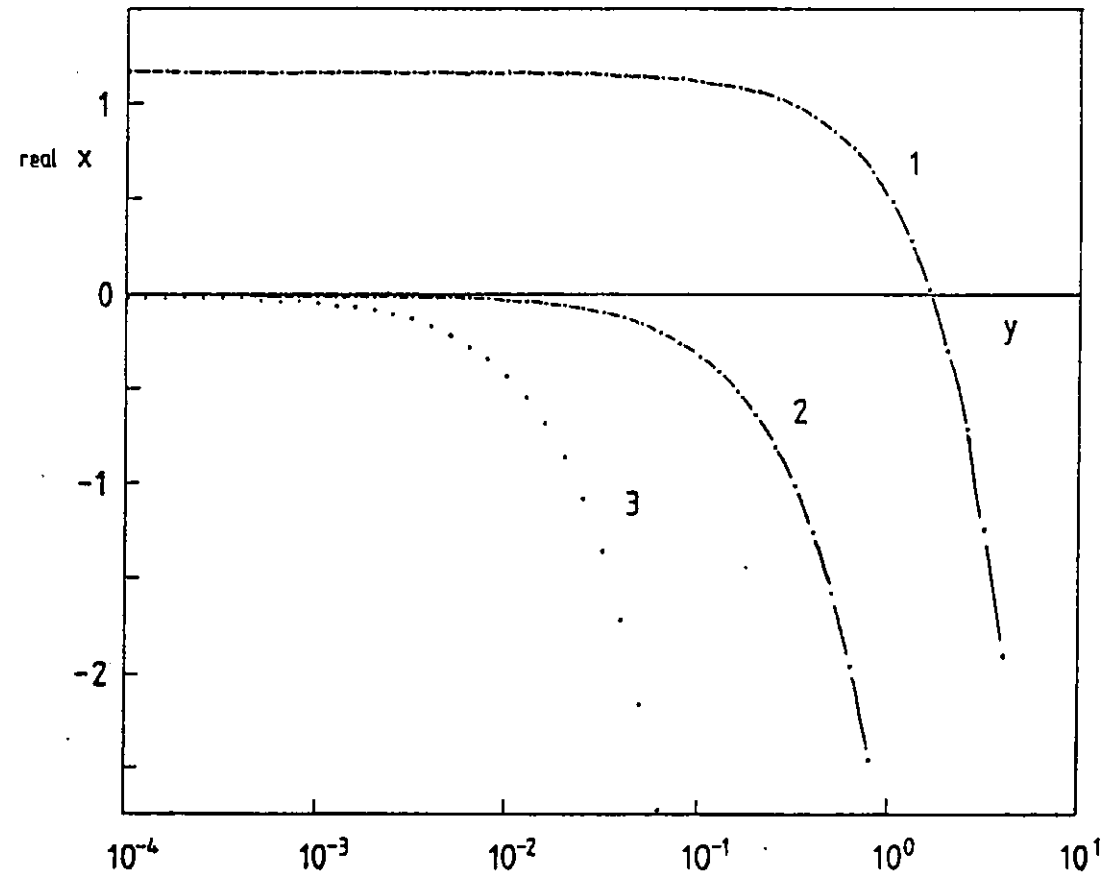

(a)

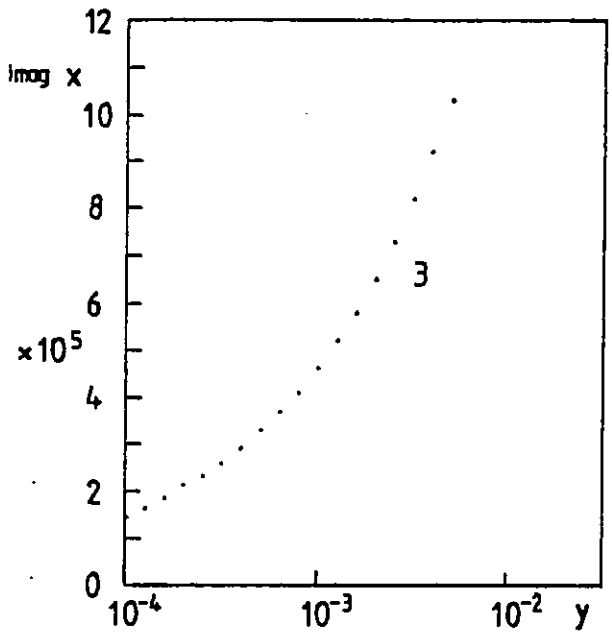

(b)

Key

-.-.-. Results obtained neglecting inertial term

..... Changes to the results produced by including inertial term

Figures 2.5

The effects of neglecting the inertial term

Plots of x against y for $T_i = 10^8$K, $T_{eo} = 2\times10^8$K, $\omega_e\tau_e = 1.54\times10^6$, $\pi_e = 2.27\times10^{-2}$, R = 0.22, $\varepsilon = 2.259\times10^{-11}$

for all wavelengths.

For the wavelength range of interest, x is real, which brings us to the only difference between the dispersion relation with $\alpha_2 = 1$ and that with $\alpha_2 = 0$. The root with a large imaginary component (labelled 3 in Figure 2.5) does not exist if $\nabla p = \frac{j\underline{x}\underline{B}}{c}$ is used ($\alpha_2 = 0$). This root is non-dispersive and has a phase velocity equal to $(V_A^2 + C_s^2)^{\frac{1}{2}}$ where V_A is the Alfvén speed and C_s the sound speed. It can therefore be identified as a damped, fast, magneto acoustic wave.

As the inertial term may be neglected in the equation for pressure balance without substantially affecting the behaviour of the electrothermal instability, this term will be neglected when studying the development in time of the above mentioned instability. This is because when any initial value problem is modelled on the computer, one is always restricted to using a time step which is smaller than the fastest time scale associated with the problem, in order that the results obtained accurately represent the true solution at any point in time. Even if one were able to use a finite difference scheme which is numerically unconditionally stable, that is the errors in the results do not amplify without bound, regardless of choice of time step, the results may still be inaccurate if the restriction on the time step is not adhered to.

Looking at Figure 2.5, the wavelength range of interest is the region where the electrothermal mode grows in time as opposed to damps. The dimensionless growth time, t_g, of the electrothermal instability is given by

$$t_g = \frac{1}{|x_1|} \qquad (2.5.2)$$

where subscript 1 means the value of x for the root labelled 1 in

Figure 2.5 while the dimensionless damping time of the mode labelled 2 is,

$$t_d = \frac{1}{|x_2|} \tag{2.5.3}$$

As can be seen from the graph, $|x_1|$ and $|x_2|$ are of order one, therefore the time scale over which parameters change is of order of one scale time for these two modes. If the inertial term is included, however, the magneto acoustic mode is present which has a damping time of order of 10^{-1} of a scale time and an oscillation period of order of 10^{-6} of a scale time.

Clearly, the fastest time scale associated with the problem is about 10^6 times greater if the inertial term is included. It is therefore advantageous, from the point of view of computational speed and efficiency, to neglect the inertial term in any numerical model designed to follow the evolution of the electrothermal instability in time into the non-linear regime.

More generally, the time scale associated with the magneto acoustic wave is much smaller that that associated with the electrothermal instability if,

$$\frac{t_m}{t_e} = \frac{\lambda}{V_m}\frac{V_{et}}{\lambda} << 1 \tag{2.5.4}$$

where t_m and t_e refer to the time scale associated with the magneto acoustic wave and the electrothermal instability respectively, and V_m and V_{et} refer to their associated velocities. V_{et} may be defined as,

$$V_{et} = \frac{\text{scale length}}{\text{scale time}} = a_{eo}\left(\frac{m_i}{m_e}\right)^{\frac{1}{2}}\frac{n_o e^2}{m_i \sigma_o} \tag{2.5.5}$$

while V_m is given by

$$V_m = (V_A^2 + C_s^2)^{\frac{1}{2}}$$

therefore equation (2.5.4) becomes,

$$\frac{t_m}{t_e} = \frac{\pi_e}{\omega_e \tau_e (2+\pi_e)} << 1 \qquad (2.5.6)$$

Provided relation (2.5.6) is true, it is worthwhile and, more importantly, valid to neglect deviations from $\nabla p = \frac{j \times B}{c}$.

SUMMARY

We have shown the inclusion of Bremsstrahlung radiation loss to enhance the growth rate of the non-convective electrothermal mode. We deduce from this result that impurity radiation would also have a destabilising effect.

The y-component of the magnetic field may be neglected without substantially affecting the linear behaviour of modes with wavelengths up to and including the optimum wavelength for growth. Hence we may neglect this component in the numerical model to follow the development of the instability into the non-linear regime.

The inclusion of the inertial term in the equation for pressure balance allows the existence of damped fast magneto acoustic waves. Neglecting this term does not considerably affect the linear behaviour of the electrothermal instability. For computational speed this term will be neglected in the numerical model.

On route to obtaining these results we have described the system, the approximations and set out the equations on which our numerical model is based to follow the evolution of the electrothermal instability.

CHAPTER 3

NON-LINEAR, STEADY-STATE SOLUTIONS

INTRODUCTION

In this chapter a model is described, and the consequences discussed, for the non-linear saturated, steady-state behaviour of the electrothermal instability. As will be shown later, it is possible for this instability to exhibit saturated, steady-state profiles of current density and electron temperature which have a large amplitude, filamentary structure. Furthermore, it is demonstrated that runaway electrons and ion acoustic instabilities can occur in the spatial maximum of the current density and electron temperature. Some calculations are presented showing the effect the presence of these filaments would have on energy transport.[4]

3.1 THE NON-LINEAR STEADY-STATE MODEL AND ASSUMPTIONS

It is assumed the electrothermal instability saturates to a steady-state in which the current density $\underline{j}_z$ is again everywhere parallel to the magnetic field $\underline{B}_z$. We know the spatial variations of the relevant parameters occur on a sufficiently small scale length that the larger scale, slower change in total pressure of the confined plasma can be neglected. We consider an equilibrium in one space dimension in which the total pressure p is a constant, that is,

$$p = n(x)\, k_B\, (T_e(x) + T_i) = \text{constant} \qquad (3.1.1)$$

where the ion temperature T_i is considered uniform. The ion temperature may be considered uniform because any fluctuation in ion temperature on a length scale of order of the wavelength of an electrothermal instability would be quickly flattened due to the ion thermal conductivity being much larger than the electron thermal conductivity perpendicular to the magnetic field, provided $\omega_e\tau_e >> 1$

$$\frac{\chi_\perp^i}{\chi_{\perp e}} \sim \left(\frac{m_i}{m_e}\right)^{\frac{1}{2}}$$

where $\chi_\perp^i$ and $\chi_{\perp e}$ are the ion and electron thermal conductivities perpendicular to the magnetic field respectively. Faradays' law dictates that the electric field E_z is also uniform.

In the steady state the electron energy equation consists of Ohmic heating, as the only energy source term, balanced by equipartition to the ions, electron thermal conduction perpendicular to the magnetic field, and Bremsstrahlung radiation loss. Assuming $\omega_e^2\tau_e^2 >> 1$ the electron energy equation (2.1.41) becomes,

$$\frac{j_z^2}{\sigma} = \frac{3n^2e^2k_B(T_e-T_i)}{m_i\sigma} + \beta_r n^2 T_e^{\frac{1}{2}} - \frac{d}{dx}\left(\frac{k_e k_B}{\omega_e^2\tau_e^2}\frac{dT_e}{dx}\right) \qquad (3.1.2)$$

The number density, n, may be eliminated from equation (3.1.2) using equation (3.1.1). Using Ohm's law, equation (2.1.24), equations (2.1.33), (2.1.34),(2.1.35) and (2.1.39) in equation (3.1.2) we obtain,

$$\alpha^1 T_e^{3/2} E_z^2 = \frac{3p^2e^2}{k_B(T_e+T_i)^2 m_i \alpha^1 T_e^{3/2}}(T_e-T_i) + \frac{\beta_r p^2 T_e^{\frac{1}{2}}}{k_B^2(T_e+T_i)^2} - \frac{d}{dx}\left(\frac{5}{2}\frac{p^2c^2}{\alpha^1 T_e^{\frac{1}{2}} B^2 (T_e+T_i)^2}\frac{dT_e}{dx}\right)$$

(3.1.3)

Equation (3.1.3) may be written in dimensionless form by defining $t = T_e/T_i$

and multiplying each term by $\frac{k_B T_i^{5/2} m_i \alpha^1}{p^2 e^2}$ to give

$$\left(\frac{\alpha^{1^2} E_z^2 m_i k_B T_i^4}{p^2 e^2}\right) t^{3/2} = \frac{3(t-1)}{(t+1)^2 t^{3/2}} + \frac{\beta_r m_i \alpha^1 T_i}{k_B e^2} \frac{t^{\frac{1}{2}}}{(t+1)^2} - \frac{d}{dx}\left[\frac{5}{2}\left(\frac{m_i c}{eB_z}\right)^2 \frac{k_B T_i}{m_i} \frac{1}{(t+1)^2 t^{\frac{1}{2}}} \frac{dt}{dx}\right] \tag{3.1.4}$$

As each term is dimensionless, we can define a parameter A_H defined as the ratio of the electric field E_z to some natural electric field, $\frac{pe}{\alpha^1 T_i^2 (m_i k_B)^{\frac{1}{2}}}$, i.e.

$$A_H^2 = \frac{m_i k_B \alpha^{1^2} T_i^4}{p^2 e^2} E_z^2 \tag{3.1.5}$$

The natural scale length for variation of $T_e(x)$ is approximately the ion Larmor radius. It is therefore convenient to replace x by s defined as,

$$s = \left(\frac{2m_i}{5k_B T_i}\right)^{\frac{1}{2}} \frac{eB}{m_i c} x \tag{3.1.6}$$

The Bremsstrahlung term defines a characteristic ion temperature for radiation loss T_R, the strength of the dimensionless radiation term being determined by,

$$B = \frac{T_i}{T_R} = \frac{\alpha^1 \beta_r m_i}{k_B e^2} T_i \tag{3.1.7}$$

where $T_R = 9.1 \times 10^8$ for deuterium. Equation (3.1.4) is simplified if we employ a distorted s dimension which we call y, defined by,

$$\frac{d}{dy} = \frac{1}{t^{\frac{1}{2}}(t+1)^2} \frac{d}{ds} \tag{3.1.8}$$

This equation now conveniently has only a second derivative and no fractional powers, that is,

$$A_H^2 \frac{t}{(t+1)^2} = \frac{3(t-1)}{t^2(t+1)^4} + \frac{B}{(t+1)^4} - \frac{d^2t}{dy^2} \qquad (3.1.9)$$

Before attempting to solve equation (3.1.9), it is instructive to consider the behaviour of the equation as t_o varies, where t_o is defined as the value of t at which $\frac{d^2t}{dy^2} = 0$,

$$A_H^2 = \frac{3(t_o-1)}{t_o^3(t_o+1)^2} + \frac{B}{t_o(t_o+1)^2} \qquad (3.1.10)$$

Figure (3.1) shows a plot of A_H^2 versus t_o for B = 0 (no Bremsstrahlung). A_H^2 has a maximum value at $t_o = \frac{3+\sqrt{57}}{8} = 1.3187$. This is the condition for onset of the electrothermal instability and gives confidence in the constant pressure model to describe both marginal stability and the non-linear steady-state.

The maximum value of $A_H^2(t_o)$ for B = 0 is 7.755×10^{-2}. For values of A_H^2 above the A_H^2-t_o curve, $\frac{d^2t}{dy^2} < 0$, whilst under the curve we have $\frac{d^2t}{dy^2} > 0$, as can be seen from equation (3.1.9). Therefore, for values of A_H^2 greater than the maximum value, t(y) can only vary monotonically on the length scale of an ion Larmor radius. For solutions of t(y) which are flat or periodic it is necessary that the electric field be less than a critical value E_c given by,

$$E < E_c = \frac{0.278\, ep}{(m_i k_B)^{\frac{1}{2}} \alpha^1 T_i^2} \qquad (3.1.11)$$

If radiation is included, the critical value of t_o, t_{oc} at which A_H^2 is a maximum is the root of,

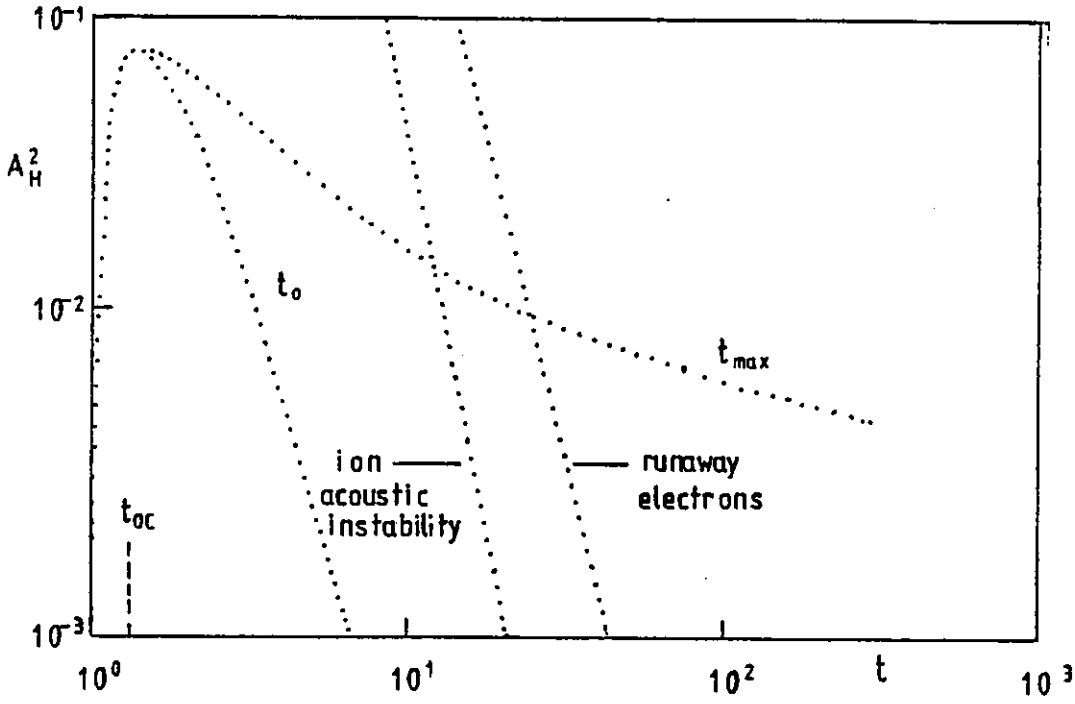

Figure 3.1 Plots of A_H^2 versus t.

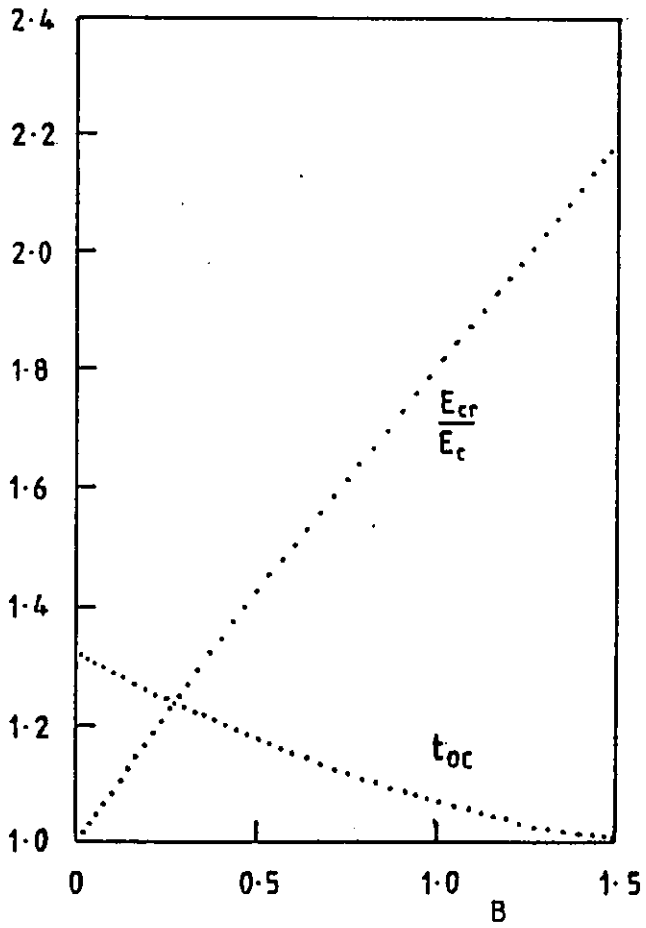

Figure 3.2 Plots of t_{oc} and E_{cr}/E_c against B.

$$3Bt_{oc}^{3} + (12+B)\, t_{oc}^{2} - 9t_{oc} - 9 = 0 \qquad (3.1.12)$$

t_{oc} is the value of T_e/T_i above which the homogeneous plasma is unstable to electrothermal instabilities with Bremsstrahlung loss included as found in Chapter 2, section 3. The maximum electric field is also increased to E_{cR} when radiation loss is included. Figure (3.2) is a plot of both t_{oc} and E_{cR}/E_c as functions of B, showing the plasma is unstable at a lower value of T_e/T_i as radiation is increased, while the maximum electric field that can be applied to sustain the discharge increases.

3.2 FILAMENTARY STRUCTURE

Referring again to figure (3.1) we can say flat profiles for t, i.e. t = constant, can only occur on the t_o curve. Also both small and large amplitude periodic, oscillatory solutions for t, for given values of A_H^2 and B, are finite lines parallel to the t axis which must include an intersection of the $A_H^2 - t_o$ curve on the right hand branch only. This is because oscillatory solutions have maxima and minima. The minimum value of t must lie in a region where $\frac{d^2t}{dy^2} > 0$ i.e. under the $A_H^2 - t_o$ curve, while the maximum value of t must lie in a region where $\frac{d^2t}{dy^2} < 0$, above the curve, and clearly the maximum value of t must be larger than the minimum value.

The maximum possible amplitude of temperature oscillations may be estimated without solving equation (3.1.9) completely, as follows. Multiplying equation (3.1.9) by $\frac{2dt}{dy}$ and integrating with respect to y we obtain,

$$\left(\frac{dt}{dy}\right)^2 = \frac{4}{(t+1)^3} + \frac{9}{(t+1)^2} + \frac{24}{(t+1)} + \frac{6}{t} - 30\ \ell n\ \left(\frac{t+1}{t}\right) \quad .$$

$$- 2A_H^2\ \left[\ell n(t+1) + \frac{1}{(t+1)}\right] - \frac{2B}{3(t+1)^3} + \text{constant of integration}$$

(3.2.1)

As will be shown, the constant of integration determines the amplitude of the electron temperature variation. For given values of A_H^2 and B there are two real values of t_o (values of t for which $\frac{d^2t}{dy^2} = 0$). Let us refer to these two values of t_o as t_{o1} and t_{o2} ($t_{o2} > t_{o1}$). As stated previously, the minimum value of t must lie between t_{o1} and t_{o2}, that is in the region where $\frac{d^2t}{dy^2} > 0$. Figure 3.3 is a plot of $\frac{d^2t}{dy^2}$ against t for three values of A_H^2 with B = 0 in all three cases. If the minimum lies arbitrarily close to either t_{o1} or t_{o2} the value of the second derivative and all higher derivatives tends to zero. Between these values, the second derivative has a maximum value. If we choose the minimum value of t, t_{min}, we know the left hand side of equation (3.2.1) is equal to zero at $t = t_{min}$. Therefore, this determines the constant of integration. The maximum value of t, t_{max}, can now be determined by finding a second value of t for which the left hand side of equation (3.2.1) is equal to zero, using Newton's method. Table (3.4) shows the values of t_{max} found as described above for randomly chosen values of t_{min} lying between t_{o1} and t_{o2}. From this we can see t_{max} increase as t_{min} decreases. Therefore the maximum amplitude of the temperature oscillation corresponds to the minimum value of t lying arbitrarily close to t_{o1}. For the case B = 0 the maximum value of t_{max} is plotted in figure 3.1 and lies to the right of the $A_H^2 - t_o$ curve.

Having found the maximum possible amplitude of the temperature oscillations we can make an interesting observation with regard to the profile of $T_e(x)$. For large amplitude oscillations the minima occur

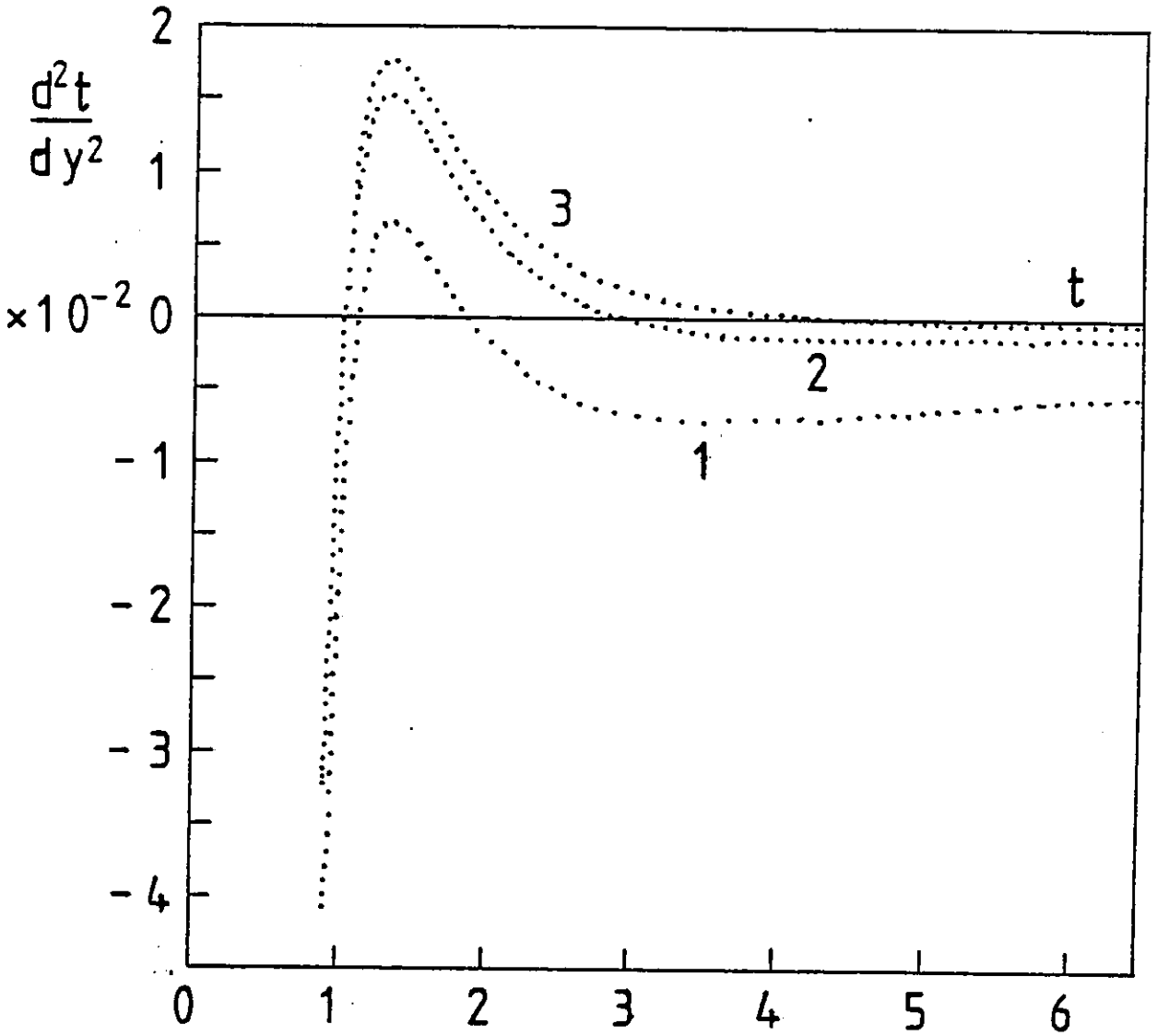

Figure 3.3

Plots of $\frac{d^2t}{dy^2}$ against t for 1) $A_H^2 = 5\times10^{-2}$

2) $A_H^2 = 1.5\times10^{-2}$

3) $A_H^2 = 0.5\times10^{-2}$

B = 0 in all three cases.

with very small values of $\frac{d^2t}{dy^2}$, whilst the maxima have comparatively large and negative values of $\frac{d^2t}{dy^2}$. This suggests the minima are very flat and shallow and the maxima sharply peaked. This is shown to be the case when equation (3.2.1) is integrated numerically.

TABLE 3.4

$A_H^2 = 0.5 \times 10^{-2}$, B = 0, $t_{o1} = 1.006851$, $t_{o2} = 4.146239$

t_{min}	t_{max}
1.006852	278.2075
1.7	35.5162
2.4	10.3184
3.1	6.0204
4.146238	4.1446

$A_H^2 = 1.5 \times 10^{-2}$, B = 0, $t_{o1} = 1.021805$ $t_{o2} = 2.923649$

t_{min}	t_{max}
1.021806	12.4712
1.5	7.5814
2.0	4.6722
2.923648	2.9239

$A_H^2 = 5 \times 10^{-2}$, B = 0, $t_{o1} = 1.096616$ $t_{o2} = 1.842697$

t_{min}	t_{max}
1.096017	2.6651
1.2	2.6099
1.4	2.3683
1.6	2.1112
1.842696	1.8445

3.3 NON-LINEAR STEADY-STATE SOLUTIONS

Equation (3.2.1) can be integrated numerically as follows. It is convenient at this stage to revert to the undistorted dimensionless space s. Using equation (3.1.8), and taking the square root, equation (3.2.1) becomes,

$$\frac{dt}{ds} = \pm \left[4t(t+1) + 9t(t+1)^2 + 24t(t+1)^3 + 6(t+1)^4 \right.$$

$$- 30t(t+1)^4 \ln\left(\frac{t+1}{t}\right) - 2A_H^2 t(t+1)^3 \left[(t+1) \ln (t+1) + 1 \right]$$

$$\left. - \frac{2B}{3} t(t+1) + C_1 t(t+1)^4 \right]^{\frac{1}{2}} = \pm G(t) \qquad (3.3.1)$$

Therefore s can be found as a function of t, namely,

$$s(t) = \pm \int \frac{dt}{G(t)} + C_2 \qquad (3.3.2)$$

where C_2 is a constant of integration. The first constant of integration, C_1, is determined by choosing the minimum temperature, t_{min}, for given values of A_H^2 and B. The maximum temperature t_{max} is then found, as described in the last section. Using t_{min} as the lower limit of the integral, we can find s(t) by varying the upper limit from a value very close to t_{min} to t_{max}. The problem then becomes one of evaluating many definite integrals numerically. This was done using a NAG library routine. The value of the second constant of integration, C_2, does not affect the shape of the temperature profile. We are therefore free to choose C_2 such that t_{min} is positioned at s = 0 for convenience. Figure 3.4 shows plots of t against s for half a wavelength. As expected, the electron temperature profile has a flat shallow minimum and sharply peaked maximum for sufficiently small values of A_H^2 when the minimum temperature, t_{min}, is chosen to be very close to t_{ol}

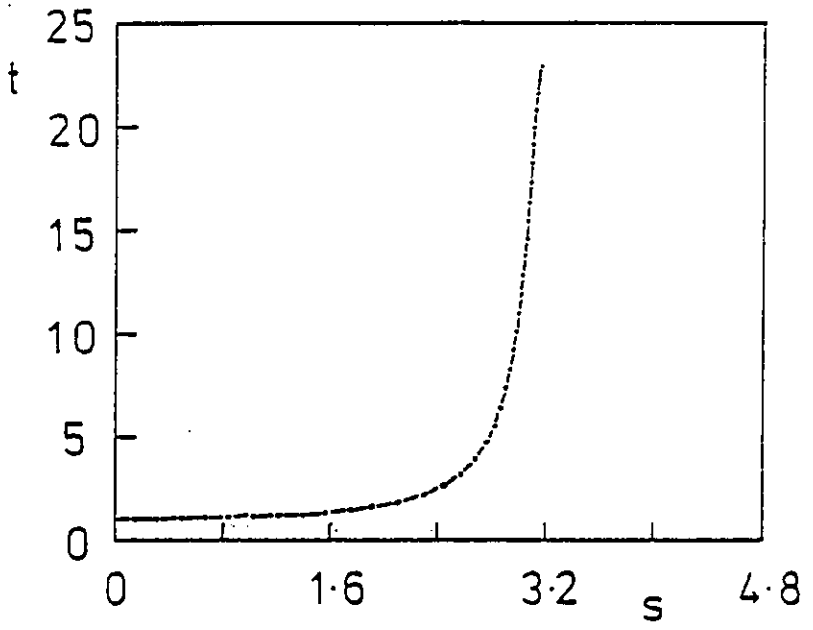

a) $A_H^2 = 1.1 \times 10^{-2}$, B = 0
$t_{ol} = 1.015605$, $t_{min} = 1.015606$
$t_{max} = 22.85$, $\frac{\lambda}{2} = 3.14$ s

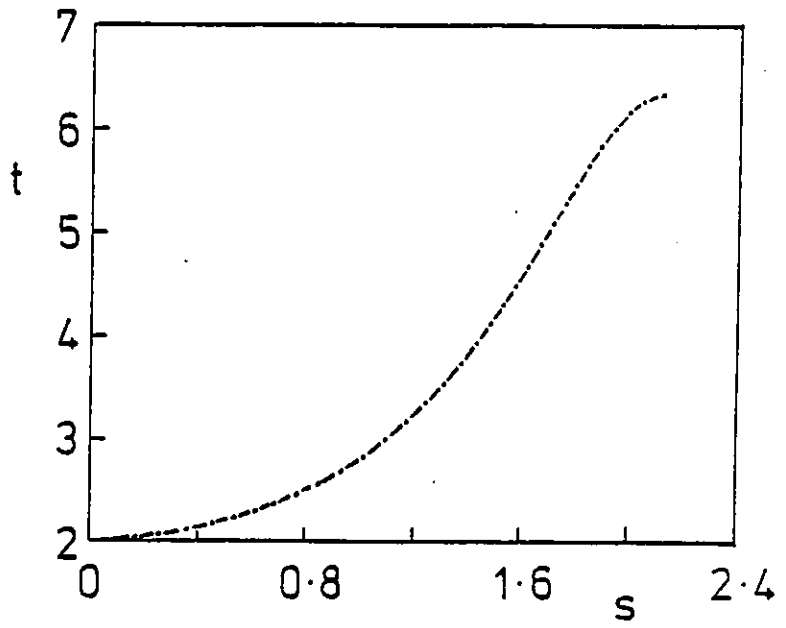

b) $A_H^2 = 1.1 \times 10^{-2}$, B = 0
$t_{min} = 2.0$, $t_{max} = 6.32$
$\frac{\lambda}{2} = 2.11$ s

Figure 3.4

Electron temperature profiles showing filamentation

Figure 3.4 contd

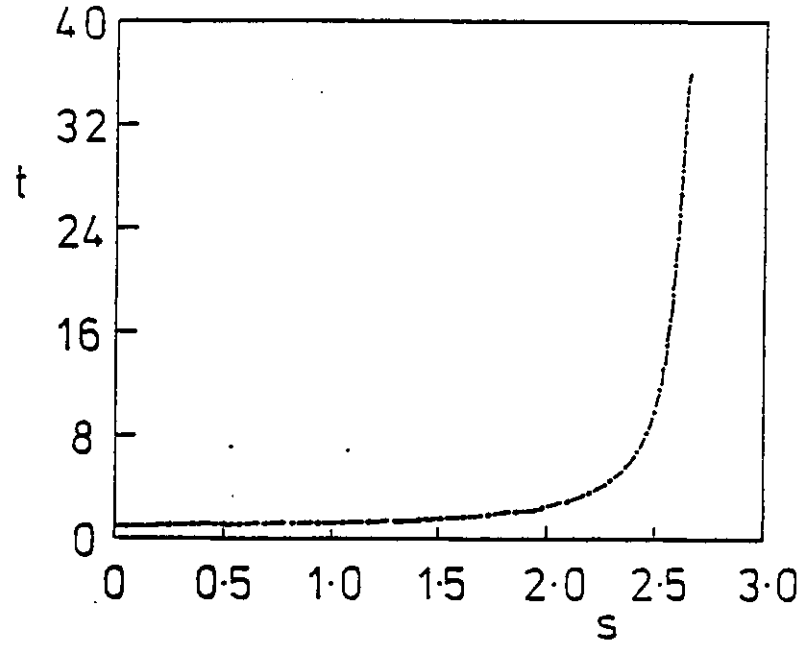

c) $A_H^2 = 1.1 \times 10^{-2}$, B = 0.11

$t_{ol} = 0.9782606$, $t_{min} = 0.9782607$

$t_{max} = 35.84$, $\frac{\lambda}{2} = 2.64s$

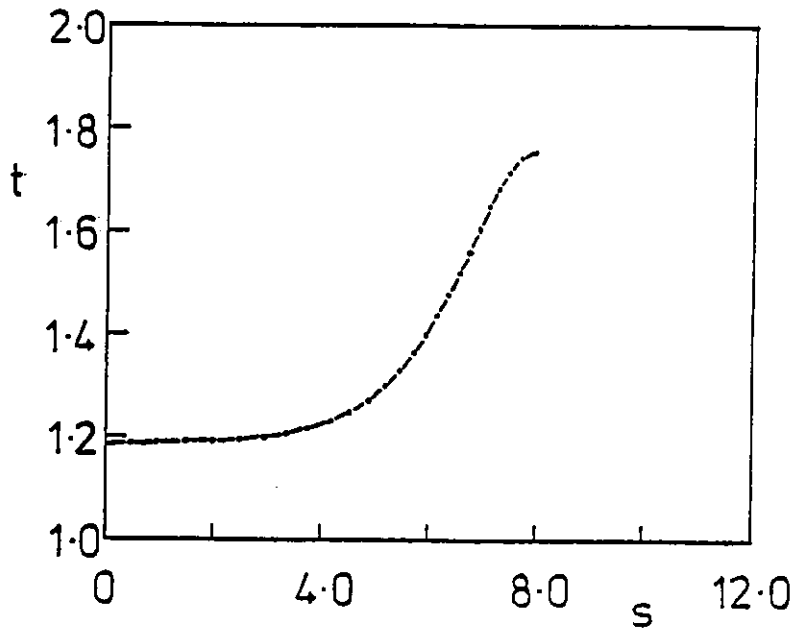

d) $A_H^2 = 7 \times 10^{-2}$, B = 0

$t_{ol} = 1.186022$, $t_{min} = 1.186023$,

$t_{max} = 1.75$, $\frac{\lambda}{2} = 7.92s$

(Figure 3.4a). For the same value of A_H^2, as t_{min} increases the amplitude of the oscillation decreases. Furthermore, the temperature profile is no longer filamentary, it is very nearly sinusoidal (Figure 3.4b). The smaller the amplitude of the oscillation for fixed A_H^2 the shorter the associated wavelength. The inclusion of Bremsstrahlung loss has two effects. It increases the amplitude of the temperature oscillation and shortens the wavelength as well (Figure 3.4c). As A_H^2 is increased, the maximum amplitude of the oscillations decreases. However, the wavelength of the maximum amplitude oscillations increases as A_H^2 is increased (Figure 3.4d).

3.4 RUNAWAY ELECTRONS AND ION ACOUSTIC INSTABILITIES

If the applied electric field exceeds a critical value E_c^1, determined by the drift velocity equal to the electron thermal speed, i.e.

$$E_c^1 = \frac{ne}{\sigma}\left(\frac{k_B T_e}{m_e}\right)^{\frac{1}{2}} \propto \frac{n}{T_e} \tag{3.4.1}$$

the plasma will be in an extreme condition of generating runaway electrons[25]. The applied field should not exceed about 1% of this value if significant numbers of runaway electrons are to be avoided. The ratio E/E_c^1 can be calculated using equations (3.1.1) and (3.1.5) as a function of t to give,

$$\frac{E}{E_c^1} = \left(\frac{m_e}{m_i}\right)^{\frac{1}{2}} A_H t(t+1) \tag{3.4.2}$$

When $E = E_c^1$ we have,

$$A_H^2 = \frac{m_i}{m_e}\,\frac{1}{t^2(t+1)^2} \tag{3.4.3}$$

This curve is plotted in Figure (3.1) for deuterium, and it crosses the t_{max} curve showing that runaway electrons can be important in the temperature maxima of the filaments even though, based on the average temperature and density of the plasma, runaway electrons should not occur. This is because the number density is low and the electron temperature high in the temperature maxima (see equation (3.4.1)).

If $T_e >> T_i$ ion acoustic instabilities can occur at a much lower electron drift velocity. We take a simplified form for the critical drift velocity above which ion acoustic instability occurs[26], that is,

$$V_d > \left(\frac{k_B T_e}{m_i}\right)^{\frac{1}{2}} + \left(\frac{k_B T_i}{m_e}\right)^{\frac{1}{2}} \tag{3.4.4}$$

Equating the right hand side of relation (3.4.4) with $\frac{\sigma E}{ne}$ and employing equation (3.1.5) we obtain,

$$A_H^2 = \frac{m_i}{m_e} \frac{[1+t^{\frac{1}{2}}(\frac{m_e}{m_i})^{\frac{1}{2}}]^2}{t^3(t+1)^2} \tag{3.4.5}$$

Choosing the ion to be deuterium the variation of A_H^2 with t as in equation (3.4.5) is also plotted in Figure (3.1) as the condition for onset of ion acoustic instability. If filaments tend to grow to their maximum amplitude, the ion acoustic turbulence will develop in the temperature maxima due to the high drift velocity there for A_H^2 less than about 1.5×10^{-2}. A fully developed runaway condition will occur in the current filament for A_H^2 less than about 10^{-2}.

3.5 EFFECTS OF THE PRESENCE OF TEMPERATURE FILAMENTS ON ENERGY TRANSPORT

Here we consider the effects of an electron temperature profile

which has a fine scale filamentary structure, with filament separation of the order of a few ion Larmor radii, on the electron energy transport in an Ohmically heated, magnetically confined plasma. It is clear the presence of such filaments could not produce a net energy loss via electron thermal conduction. It is possible, however, that their presence could lead to an anomalously high electron energy loss via equipartition to the ions. From recent experimental results[14], such fine scale electron temperature peaks (and density troughs), if they existed, would not be spatially resolved. Instead, the spatial average temperature and density would be measured, and the equipartition rate calculated classically. The value obtained in this way would be different from the value obtained if the fine structure of the electron temperature and density were taken into account. We can test this hypothesis by looking at the ratio obtained by taking the equipartition rate averaged over one wavelength and dividing by the equipartition rate calculated using the mean electron temperature, that is,

$$R_E = \frac{\frac{1}{\lambda}\int_0^{\lambda} \frac{(t-1)}{t^{3/2}(t+1)^2}\, ds}{\frac{(\bar{t}-1)}{\bar{t}^{3/2}(\bar{t}+1)^2}} \qquad (3.5.1)$$

where $$\bar{t} = \frac{1}{\lambda}\int_0^{\lambda} t\, ds \qquad (3.5.2)$$

and equation (3.1.1) has been used in the derivation of equation (3.5.1). The ratio R_E has been calculated for many temperature profiles. We know experimental measurements of electrical conductivity agree well with results predicted from theory using the Spitzer model. Therefore we must be able to demonstrate that the presence of these filaments does not appreciably affect the electrical conductivity in order for this

model to be acceptable as a possible mechanism for enhanced electron energy loss. For this reason we have also calculated the ratio, R_c, of the electrical conductivity averaged over one wavelength to the electrical conductivity calculated using the electron temperature averaged over one wavelength. The value of this ratio is included in Table (3.5).

TABLE 3.5

R_E/R_c	A_H^2	t_{max}	t_{min}	R_E	R_c
0.9036	7×10^{-2}	1.7536	1.1860	0.9096	1.0066
0.4726	2.2×10^{-2}	6.9425	1.0335	0.5609	1.1868
0.5835	1.1×10^{-2}	22.8504	1.0156	0.8682	1.4879
0.6696	9×10^{-3}	36.9329	1.0126	1.0958	1.6366
1.0372	"	34.7642	1.1000	1.6190	1.5610
1.2615	"	7.8835	2.0000	1.3690	1.0852
0.7348	8×10^{-3}	50.9998	1.0112	1.2812	1.7435
1.1274	"	47.5551	1.1000	1.8200	1.6143
2.0109	"	20.4849	2.0000	2.4537	1.2202
0.8226	7×10^{-3}	76.7902	1.0097	1.5508	1.8852
1.1644	"	70.7340	1.1000	2.0923	1.7969
1.3051	"	8.5314	2.2000	1.4135	1.0831
0.9352	6×10^{-3}	131.6769	1.0083	1.9439	2.0785
1.2468	"	119.3086	1.1000	2.4752	1.9853
1.5714	"	13.5490	2.0000	1.8318	1.1657

B = 0 in all above

Looking at Table (3.5), assuming the filaments have their maximum amplitude, and neglecting the effects of ion acoustic turbulence, both R_E and R_c increase as A_H^2 decreases. Furthermore R_E and R_c are greater than one for $A_H^2 \lesssim 9 \times 10^{-3}$. However, if the filaments do not have their maximum amplitude for a given value of A_H^2, the ratio R_E/R_c increases as t_{max} decreases.

We may conclude from these results that for sufficiently small values of A_H^2 the presence of electron temperature filaments can lead to a substantially higher electron energy loss than would be calculated from experimental results. However the electrical conductivity would also be anomalous which we know is not the case. If the temperature filaments develop to an amplitude which is less than the maximum possible, the electron energy loss is still anomalously high whilst the electrical conductivity is not appreciably affected.

The necessity for a time dependent model

All the results in this chapter come from a model which assumes the electrothermal instability saturates and reaches a steady-state which is stable. Whether a steady-state is attainable, and whether it is stable can be found only from a study of the development in time of the electrothermal instability. Such a model would also establish which of the many possible values of A_H^2 and configurations of electron temperature profile are obtained if a stable steady-state is reached. It would also show whether at any stage in the development of the electrothermal instability conditions are reached such that the ion acoustic instability is triggered. We only know from this model that it is possible provided certain conditions on the value of A_H^2 and electron temperature profile are satisfied.

CHAPTER 4

A NUMERICAL MODEL TO FOLLOW THE EVOLUTION OF THE ELECTROTHERMAL INSTABILITY

INTRODUCTION

In this chapter we develop a model to study the time development of the electrothermal instability into the non-linear regime. The plasma considered is subject to the same conditions as that considered in Chapter 2. We assume the plasma is in equilibrium initially as in Section 2.1. A small perturbation is then applied and its development in time is followed numerically. The perturbation cannot be considered small compared to equilibrium quantities for all time so that the linearized equations in Section 2.1 are not valid here. The equations are again written in dimensionless form.

4.1 EQUATIONS

The equations which can be used to describe the state of the plasma when a perturbation has been applied, and for all subsequent times, were derived in Section 2.1 These are :

Faraday's Law

$$\frac{\partial E_y}{\partial x} = -\frac{1}{c}\frac{\partial B_z}{\partial t} \qquad (4.1.1)$$

remembering that all quantities are allowed to vary only in the x-direction and the y-component of the magnetic field has been neglected (see Section 2.4).

Ampère's Law

$$\frac{\partial B_z}{\partial x} = -\frac{4\pi}{c} j_y \tag{4.1.2}$$

Pressure Balance

$$\frac{\partial p}{\partial x} = \frac{j_y B_z}{c} \tag{4.1.3}$$

where the inertial term has been neglected. The reason for this was given in Section 2.5. p is the total pressure. $p = p_e + p_i$.

Ohm's Law

The two relevant components of Ohm's law are,

$$E_y - \frac{V_x B_z}{c} = \frac{j_y}{\sigma} \tag{4.1.4}$$

$$E_z = \frac{j_z}{\sigma} \tag{4.1.5}$$

Electron heat balance equation

$$\frac{3}{2} nk_B \frac{\partial T_e}{\partial t} + \frac{3}{2} nk_B V_x \frac{\partial T_e}{\partial x} + nk_B T_e \frac{\partial V_x}{\partial x} = \frac{\partial}{\partial x}\left(\frac{K_e k_B}{(1+\omega_e^2 \tau_e^2)} \frac{\partial T_e}{\partial x}\right)$$

$$+ \frac{j^2}{\sigma} - \frac{3n^2 e^2 k_B (T_e - T_i)}{m_i \sigma} - \beta_r n^2 T_e^{\frac{1}{2}} \tag{4.1.6}$$

Continuity Equation

$$\frac{\partial n}{\partial t} + n \frac{\partial V_x}{\partial x} + V_x \frac{\partial n}{\partial x} = 0 \tag{4.1.7}$$

These equations may be written in dimensionless form with the help of the

following definitions :

We define a scale length

$$L_o = a_{eo} \left(\frac{m_i}{m_e}\right)^{\frac{1}{2}} = \left(\frac{k_B T_{eo}}{m_i}\right)^{\frac{1}{2}} \frac{m_i c}{eB_{zo}} \tag{4.1.8}$$

and a scale time

$$t_o = \frac{m_i \sigma_o}{n_o e^2} \tag{4.1.9}$$

where a zero subscript denotes the equilibrium values before a perturbation is applied so that we can define a dimensionless space $\tilde{x}$,

$$\tilde{x} = \frac{x}{L_o} \rightarrow \frac{\partial}{\partial x} = \frac{1}{L_o} \frac{\partial}{\partial x} \tag{4.1.10}$$

and a dimensionless time,

$$\tilde{t} = \frac{t}{t_o} \rightarrow \frac{\partial}{\partial t} = \frac{1}{t_o} \frac{\partial}{\partial \tilde{t}}$$

Similarly, we can write all quantities in units of equilibrium values, i.e.

$$\tilde{T}_e = \frac{T_e}{T_{eo}}, \quad \tilde{n} = \frac{n}{n_o}, \quad \tilde{B}_z = \frac{B_z}{B_{zo}}, \quad \tilde{j}_z = \frac{j_z}{j_{zo}}, \quad \tilde{j}_y = \frac{j_y}{j_{zo}},$$

$$\tilde{E}_z = \frac{E_z}{E_{zo}}, \quad \tilde{E}_y = \frac{E_y}{E_{zo}}, \quad \tilde{V}_x = V_x \frac{t_o}{L_o}, \quad \tilde{T}_i = \frac{T_i}{T_{eo}},$$

$$\tilde{\sigma} = \frac{\sigma}{\sigma_o} = \tilde{T}_e^{\,3/2} \tag{4.1.11}$$

When equations (4.1.1) to (4.1.7) are written in terms of the quantities defined in relations (4.1.10) and (4.1.11), it is found to be convenient

to define the following dimensionless quantities :

$$A_F = \frac{\sigma_o E_{zo}}{en_o}\left(\frac{m_i}{k_B T_{eo}}\right)^{\frac{1}{2}}, \qquad \varepsilon = \frac{3n_o c^2}{8\pi\sigma_o K_{eo}}$$

$$\pi_e = \frac{8\pi n_o k_B T_{eo}}{B_{zo}^2}, \qquad R = \frac{\beta_r m_i \sigma_o}{k_B T_{eo}^{\frac{1}{2}} e^2} \tag{4.1.12}$$

and a function we call F given by

$$F = 1 + \omega_o^2 \tau_o^2 \frac{\tilde{T}_e^3 \tilde{B}_z^2}{\tilde{n}^2} \tag{4.1.13}$$

equations (4.1.1) to (4.1.7) can then be written,

<u>Faraday's Law</u>

$$\frac{\partial \tilde{B}_z}{\partial \tilde{t}} = - A_F \frac{\partial \tilde{E}_y}{\partial \tilde{x}} \tag{4.1.14}$$

<u>Ampère's Law</u>

$$\frac{\partial \tilde{B}_z}{\partial \tilde{x}} = - \frac{\pi_e A_F}{2} \tilde{j}_y \tag{4.1.15}$$

<u>Pressure Balance</u>

$$\frac{\partial \tilde{p}}{\partial \tilde{x}} = A_F \tilde{j}_y \tilde{B}_z \tag{4.1.16}$$

where $\tilde{p} = \tilde{p}_e + \tilde{p}_i = \tilde{n}\,(\tilde{T}_e + \tilde{T}_i)$

<u>Ohm's Law</u>

$$A_F \tilde{E}_y - \tilde{V}_x \tilde{B}_z = \frac{\tilde{j}_y}{\tilde{\sigma}} A_F \tag{4.1.17}$$

$$\tilde{E}_z = \frac{\tilde{j}_z}{\tilde{\sigma}} \tag{4.1.18}$$

<u>Electron heat balance equation</u>

$$\tilde{n}\frac{\partial \tilde{T}_e}{\partial \tilde{t}} + \tilde{n}\tilde{V}_x \frac{\partial \tilde{T}_e}{\partial \tilde{x}} + \frac{2}{3}\tilde{n}\tilde{T}_e \frac{\partial \tilde{V}_x}{\partial \tilde{x}}$$

$$= \frac{2}{\pi_e \varepsilon}\frac{\partial}{\partial \tilde{x}}\left(\tilde{\chi}_{\perp e}\frac{\partial \tilde{T}_e}{\partial \tilde{x}}\right) + \frac{2}{3}\frac{A_F^2}{\tilde{\sigma}}\left(\tilde{j}_y + \tilde{j}_z^2\right)$$

$$- \frac{2\tilde{n}^2(\tilde{T}_e - \tilde{T}_i)}{\tilde{\sigma}} - \frac{2}{3} R\, \tilde{n}^2 \tilde{T}_e^{\frac{1}{2}} \tag{4.1.19}$$

where $\tilde{\chi}_{\perp e} = \frac{K_e}{K_{eo}} \frac{1}{(1+\omega_e^2 \tau_e^2)} = \frac{\tilde{T}_e^{5/2}}{F}$

$$\underline{\text{Continuity Equation}} \qquad \frac{\partial \tilde{n}}{\partial \tilde{t}} + \tilde{V}_x \frac{\partial \tilde{n}}{\partial \tilde{x}} + \tilde{n} \frac{\partial \tilde{V}_x}{\partial \tilde{x}} = 0 \qquad (4.1.20)$$

For ease in reproducing the script, from now on the tilde notation will be dropped. All quantities referred to will be dimensionless as defined in this section unless otherwise stated.

4.2 TRANSFORMATION OF EQUATIONS INTO SOLVABLE FORM

There are seven equations (4.1.14-20), of which three are time dependent. If the inertial term had been retained in equation (4.1.16), there would be four time dependent equations. It would then be a simple matter to use the three space like equations to produce four coupled, time dependent equations in the four unknowns, n, T_e, B_z and V_x only. However, this is not the case. We have three time dependent equations : Faraday's Law, the continuity equation and the equation for electron heat balance, which describe the evolution of B_z, n and T_e respectively, in terms of all the other variables. It is straightforward to use equations (4.1.15) and (4.1.18) to write j_y and j_z in terms of B_z and T_e (and E_z which is not an independent variable). However we are left finally with the problem of obtaining an expression for V_x in terms of B_z, T_e and n as well as incorporating the condition imposed by the equation for pressure balance (4.1.16). In order to achieve this end the following method was used.

Multiply Faraday's Law, equation (4.1.14) by B_z to give,

$$B_z \frac{\partial B_z}{\partial t} = - A_F B_z \frac{\partial E_y}{\partial x} \qquad (4.2.1)$$

Now,

$$B_z \frac{\partial E_y}{\partial x} = \frac{\partial}{\partial x} (E_y B_z) - E_y \frac{\partial B_z}{\partial x} \qquad (4.2.2)$$

and, using Ampere's Law, equation (4.1.15),

$$E_y \frac{\partial B_z}{\partial x} = - \frac{\pi_e A_F}{2} E_y j_y \tag{4.2.3}$$

so that equation (4.2.1) can be written

$$\frac{1}{2} \frac{\partial}{\partial t} B_z^2 = - A_F \frac{\partial}{\partial x} (E_y B_z) + \frac{\pi_e A_F^2}{2} E_y j_y \tag{4.2.4}$$

Using Ohm's Law, equation (4.1.17) as an expression for E_y together with the equation for pressure balance, equation (4.1.16), we obtain,

$$E_y B_z = \frac{1}{\sigma A_F} \frac{\partial p}{\partial x} + \frac{V_x B_z^2}{A_F} \tag{4.2.5}$$

Similarly, we may write,

$$E_y j_y = \frac{j_y^2}{\sigma} + \frac{V_x}{A_F^2} \frac{\partial p}{\partial x} \tag{4.2.6}$$

Substituting (4.2.5) and (4.2.6) into (4.2.4) and rearranging we obtain,

$$\frac{1}{\pi_e} \frac{\partial B_z^2}{\partial t} = - (A_F^2 \frac{j_y^2}{\sigma} + V_x \frac{\partial p}{\partial x}) - \frac{2}{\pi_e} \frac{\partial}{\partial x} (\frac{1}{\sigma} \frac{\partial p}{\partial x} + V_x B_z^2) \tag{4.2.7}$$

We now turn our attention to the electron energy equation which we rewrite in terms of electron pressure instead of electron temperature defined by, $p_e = nT_e$. Equation (4.1.19) then becomes,

$$\frac{\partial p_e}{\partial t} + \frac{5}{3} p_e \frac{\partial V_x}{\partial x} + V_x \frac{\partial p_e}{\partial x} = \frac{2}{\pi_e \varepsilon} \frac{\partial}{\partial x} (\frac{\chi_{\perp e}}{n} \frac{\partial p_e}{\partial x} - \frac{\chi_{\perp e} p_e}{n^2} \frac{\partial n}{\partial x})$$

$$+ \frac{2}{3} \frac{A^2}{\sigma} (j_y^2 + j_z^2) - \frac{2n(p_e - p_i)}{\sigma} - \frac{2}{3} R\, n^{3/2}\, p_e^{1/2} \tag{4.2.8}$$

The continuity equation, (4.1.20), has also been used to obtain equation (4.2.8).

We can obtain an equation for the rate of change of ion pressure by multiplying the continuity equation, (4.1.20), by T_i to give,

$$\frac{\partial p_i}{\partial t} + V_x \frac{\partial p_i}{\partial x} + p_i \frac{\partial V_x}{\partial x} = 0 \qquad (4.2.9)$$

remembering that the ion temperature is both uniform in space and constant in time.

We now add equations (4.2.7), (4.2.8) and (4.2.9) and obtain an expression for the rate of change of the internal energy,

$$\frac{\partial}{\partial t}\left(p+\frac{B_z^2}{\pi_e}\right) + 2V_x\left(\frac{\partial p}{\partial x} + \frac{1}{\pi_e}\frac{\partial B_z^2}{\partial x}\right) + \left(p+\frac{2}{3}p_e+\frac{2B_z^2}{\pi_e}\right)\frac{\partial V_x}{\partial x}$$

$$= \frac{2}{\pi_e \varepsilon}\frac{\partial}{\partial x}\left(\frac{\chi_{ie}}{n}\frac{\partial p_e}{\partial x} - \frac{\chi_{ie} p_e}{n^2}\frac{\partial n}{\partial x}\right) + \frac{A_F^2}{\sigma}\left(\frac{2}{3}j_z^2 - \frac{1}{3}j_y^2\right)$$

$$- \frac{2n(p_e-p_i)}{\sigma} - \frac{2}{3}R\, n^{3/2}\, p_e^{1/2} - \frac{\partial}{\partial x}\left(\frac{2}{\pi_e \sigma}\frac{\partial p_e}{\partial x}\right) \qquad (4.2.10)$$

The second term on the left hand side of equation (4.2.10) is equal to zero. From equations (4.1.15) and (4.1.16) we have,

$$\frac{\partial p}{\partial x} + \frac{1}{\pi_e}\frac{\partial B_z^2}{\partial x} = 0 \qquad (4.2.11)$$

That is the internal energy, $p + \frac{B_z^2}{\pi_e}$, is not a function of x. We shall call this quantity $E_I = p + \frac{B_z^2}{\pi_e}$, a constant in space, not in time. We now have an expression for $\frac{\partial V_x^e}{\partial x}$ in terms of p_e, n, B_z and their spatial derivatives (no time derivatives) and $\frac{\partial E_I}{\partial t}$ which is not a function of x. Let $g = \left(\frac{2B_z^2}{\pi_e} + p + \frac{2}{3}p_e\right)^{-1}$ and using (4.1.15) and (4.1.18),

$$\frac{\partial V_x}{\partial x} = g\left(\frac{2}{\pi_e \varepsilon}\frac{\partial}{\partial x}\left(\frac{\chi_{\perp e}}{n}\frac{\partial p_e}{\partial x} - \frac{\chi_\perp p_e}{n^2}\frac{\partial n}{\partial x}\right) + \frac{2}{3}A_F{}^2\sigma E_z{}^2\right.$$

$$\left. - \frac{4}{3\pi_e{}^2\sigma}\left(\frac{\partial B_z}{\partial x}\right)^2 - \frac{2n(p_e-p_i)}{\sigma} - \frac{2}{3}R\,n^{3/2}\,p_e{}^{\frac{1}{2}} - \frac{\partial}{\partial x}\left(\frac{2}{\pi_e\sigma}\frac{\partial p}{\partial x}\right) - \frac{\partial E_I}{\partial t}\right)$$

(4.2.12)

Integrating equation (4.2.12) by parts and using $\frac{\partial g}{\partial x} = g^2\frac{\partial}{\partial x}\left(\frac{p_e}{3} + p_i\right)$

$$V_x = \frac{2}{\pi_e\varepsilon}g\left(\frac{\chi_{\perp e}}{n}\frac{\partial p_e}{\partial x} - \frac{\chi_\perp p_e}{n^2}\frac{\partial n}{\partial x}\right) - \frac{2}{3}\frac{2g}{\pi_e\sigma}\frac{\partial p}{\partial x}$$

$$- \frac{2}{\pi_e\varepsilon}\int\left(\frac{\chi_{\perp e}}{n}\frac{\partial p_e}{\partial x} - \frac{\chi_{\perp e}p_e}{n^2}\frac{\partial n}{\partial x} - \frac{\varepsilon}{\sigma}\frac{\partial p}{\partial x}\right) g^2\frac{\partial}{\partial x}\left(\frac{p_e}{3} + p_i\right)\,dx$$

$$+ \frac{2}{3}E_z{}^2\,A_F{}^2\int g\,\sigma\,dx + \frac{1}{3}\left(\frac{2}{\pi_e}\right)^2\int B_z\frac{\partial}{\partial x}\left(\frac{g}{\sigma}\frac{\partial B_z}{\partial x}\right)\,dx$$

$$- \int g\left(\frac{2n(p_e-p_i)}{\sigma} + \frac{2}{3}R\,n^{3/2}\,p_e{}^{\frac{1}{2}} + \frac{\partial E_I}{\partial t}\right)\,dx + c(t) \qquad (4.2.13)$$

where c(t) is the time dependent constant of integration.

We can now use these expressions for V_x and $\frac{\partial V_x}{\partial x}$ in the three time dependent equations.

Continuity equation

The continuity equation (4.1.20) may be written in conservative form,

$$\frac{\partial n}{\partial t} + \frac{\partial}{\partial x}(n\,V_x) = 0 \qquad (4.2.14)$$

Substituting equation (4.2.13) for V_x into equation (4.2.14) and after some algebra we obtain,

$$\frac{\partial n}{\partial t} = \frac{\partial}{\partial x}\left(\frac{2g}{\pi_e}\left(\frac{\chi_{\perp e} p_e}{\varepsilon n} + \frac{nT_i}{\sigma}\right)\frac{\partial n}{\partial x}\right) + \frac{\partial}{\partial x}\left(\frac{2g}{\pi_e}\left(\frac{n}{\sigma} - \frac{\chi_{\perp e}}{\varepsilon}\right)\frac{\partial p_e}{\partial x}\right)$$

$$- \frac{2T_i g}{\pi_e}\left(\frac{\chi_{\perp e} p_e g}{\varepsilon n} + \frac{nT_i}{\sigma} + \frac{1}{3\sigma}\right)\left(\frac{\partial n}{\partial x}\right)^2 + \left(\frac{\chi_{\perp e} g^2}{\pi_e \varepsilon}\left(T_i - \frac{p_e}{3n}\right) - \frac{g}{3\pi_e \sigma}\left(1+4gnT_i\right)\right)$$

$$\times \frac{\partial n}{\partial x}\frac{\partial p_e}{\partial x} + \frac{2g^2}{3\pi_e}\left(\frac{\chi_{\perp e}}{\varepsilon} - \frac{n}{\sigma}\right)\left(\frac{\partial p_e}{\partial x}\right)^2$$

$$+ \left(\frac{\chi_{\perp e} g^2}{\pi_e \varepsilon}\left(T_i - \frac{p_e}{3n}\right) - \frac{g}{3\pi_e \sigma}\left(1+4gnT_i\right)\right)\frac{\partial p_e}{\partial x}\frac{\partial n}{\partial x}$$

$$+ \frac{1}{3}\left(\frac{2}{\pi_e}\right)^2 \frac{ng}{\sigma}\left(\frac{\partial B_z}{\partial x}\right)^2 - (\text{integral terms} + c(t))\frac{\partial n}{\partial x}$$

$$+ g\left(-\frac{2}{3} A_F^2 E_z^2 \sigma + \frac{2n(p_e - p_i)}{\sigma} + \frac{2}{3} R\, n^{3/2} p_e^{\frac{1}{2}} + \frac{\partial E_I}{\partial t}\right) n \qquad (4.2.15)$$

where "integral terms" in equation (4.2.15) refers to all the x-dependent terms in expression (4.2.13) for V_x except those which are not integrals.

Electron energy equation

Similarly, with the help of equations (4.1.15), (4.1.18), (4.2.12) and (4.2.13) the electron energy equation (4.2.8) becomes,

$$\frac{\partial p_e}{\partial t} = \frac{\partial}{\partial x}\left[\frac{2p_e}{\pi_e}\left(\frac{\chi_{\perp e}}{\varepsilon n^2}\left(1 + \frac{5}{3} p_e g\right) + \frac{5}{3}\frac{gT_i}{\sigma}\right)\frac{\partial n}{\partial x}\right]$$

$$+ \frac{\partial}{\partial x}\left[\frac{2}{\pi_e}\left(\frac{\chi_{\perp e}}{\varepsilon n}\left(1 - \frac{5}{3} p_e g\right) + \frac{5}{3}\frac{p_e g}{\sigma}\right)\frac{\partial p_e}{\partial x}\right] - \frac{5}{3}\frac{2}{\pi_e} g^2 p_e T_i \left[\frac{T_i}{\sigma} + \frac{\chi_{\perp e} p_e}{\varepsilon n^2}\right]\left(\frac{\partial n}{\partial x}\right)^2$$

$$+ \frac{g}{\pi_e}\left[\frac{5}{3}\frac{\chi_{\perp e} p_e}{\varepsilon n}\left(T_i g - \frac{1}{n}\left(1 + \frac{p_e g}{3}\right)\right) - \frac{5}{3}\frac{T_i}{\sigma}\left(\frac{4}{3} p_e g + 1\right) + \frac{\chi_{\perp e} p_e}{\varepsilon n^2} + \frac{2}{3}\frac{T_i}{\sigma}\right]\frac{\partial n}{\partial x}\frac{\partial p_e}{\partial x}$$

$$+ \frac{2g}{\pi_e}\left[\frac{5}{3}\left(\frac{\chi_{\perp e}}{\varepsilon n} - \frac{1}{\sigma}\right)\left(1 + \frac{p_e g}{3}\right) + \frac{2}{3\sigma} - \frac{\chi_{\perp e}}{\varepsilon n}\right]\left(\frac{\partial p_e}{\partial x}\right)^2$$

$$+ \frac{g}{\pi_e}\left[\frac{5}{3}\frac{\chi_{\perp e} p_e}{\varepsilon n}\left(T_i g - \frac{1}{n}\left(1 + \frac{p_e g}{3}\right)\right) - \frac{5}{3}\frac{T_i}{\sigma}\left(\frac{4}{3} p_e g + 1\right) + \frac{\chi_{\perp e} p_e}{\varepsilon n^2} + \frac{2}{3}\frac{T_i}{\sigma}\right]$$

$$x \frac{\partial p_e}{\partial x} \frac{\partial n}{\partial x} + \left(\frac{2}{\pi_e}\right)^2 \frac{1}{3\sigma} \left[2 + \frac{5}{3} p_e g\right] \left(\frac{\partial B_z}{\partial x}\right)^2$$

$$- (\text{integral terms} + c(t)) \frac{\partial p_e}{\partial x} \qquad (4.2.16)$$

$$+ \left[\frac{2}{3} \frac{A_F^2 E_z^2 p_e^{\frac{1}{2}}}{n^{3/2}} - \frac{2n^{5/2}(p_e - p_i)}{p_e^{5/2}} - \frac{2}{3} R\, n^{3/2}\, p_e^{-1/2}\right.$$

$$\left. + \frac{5}{3} g \left[-\frac{2}{3} A_F^2 E_z^2 \sigma + \frac{2n(p_e - p_i)}{\sigma} + \frac{2}{3} R\, n^{3/2}\, p_e^{\frac{1}{2}} + \frac{\partial E_I}{\partial t}\right]\right] p_e$$

where $\sigma = T_e^{3/2} = \frac{p_e^{3/2}}{n^{3/2}}$ has been used.

Faraday's Law

Faraday's Law may also be written in the same form as equations (4.2.15) and (4.2.16). Starting with equation (4.1.14) and using Ampere's Law equation (4.1.15), and Ohm's Law, equation (4.1.17), Faraday's Law may be written in conservative form,

$$\frac{\partial B_z}{\partial t} = \frac{\partial}{\partial x} \left(\frac{2}{\pi_e \sigma} \frac{\partial B_z}{\partial x} - V_x B_z\right) \qquad (4.2.17)$$

Substituting equation (4.2.13) for V_x and after some algebra we obtain,

$$\frac{\partial B_z}{\partial t} = \frac{\partial}{\partial x} \left[\frac{2gB_z}{\pi_e} \left(\frac{T_i}{\sigma} + \frac{\chi_{\perp e} p_e}{\epsilon n^2}\right) \frac{\partial n}{\partial x}\right] + \frac{\partial}{\partial x} \left[\frac{2gB_z}{\pi_e} \left(\frac{1}{\sigma} - \frac{\chi_{\perp e}}{\epsilon n}\right) \frac{\partial p_e}{\partial x}\right]$$

$$+ \frac{\partial}{\partial x} \left[\frac{2}{\pi_e \sigma} \frac{\partial B_z}{\partial x}\right] - \frac{2g^2 B_z T_i}{\pi_e} \left[\frac{\chi_{\perp e} p_e}{\epsilon n^2} + \frac{T_i}{\sigma}\right] \left(\frac{\partial n}{\partial x}\right)^2$$

$$+ \frac{g^2 B_z}{\pi_e} \left[\frac{\chi_{\perp e}}{\epsilon n} \left(T_i - \frac{p_e}{3n}\right) - \frac{4}{3} \frac{T_i}{\sigma}\right] \frac{\partial n}{\partial x} \frac{\partial p_e}{\partial x} - \frac{gT_i}{3\pi_e \sigma} \frac{\partial n}{\partial x} \frac{\partial B_z}{\partial x}$$

$$+ \frac{g^2 B_z}{\pi_e} \left[\frac{\chi_{\perp e}}{\epsilon n} \left(T_i - \frac{p_e}{3n}\right) - \frac{4}{3} \frac{T_i}{\sigma}\right] \frac{\partial p_e}{\partial x} \frac{\partial n}{\partial x} + \frac{2B_z g^2}{3\pi_e} \left[\frac{\chi_{\perp e}}{\epsilon n} - \frac{1}{\sigma}\right] \left(\frac{\partial p_e}{\partial x}\right)^2$$

$$- \frac{g}{3\pi_e \sigma} \frac{\partial p_e}{\partial x} \frac{\partial B_z}{\partial x} - \frac{gT_i}{3\pi_e \sigma} \frac{\partial B_z}{\partial x} \frac{\partial n}{\partial x} - \frac{g}{3\pi_e \sigma} \frac{\partial B_z}{\partial x} \frac{\partial p_e}{\partial x}$$

$$+ \left(\frac{2}{\pi_e}\right)^2 \frac{B_z g}{3\sigma} \left(\frac{\partial B_z}{\partial x}\right)^2 - [\text{integral terms} + c(t)] \frac{\partial B_z}{\partial x}$$

$$+ g \left[-\frac{2}{3} A_F^2 E_z^2 \sigma + \frac{2n(p_e - p_i)}{\sigma} + \frac{2}{3} R\, n^{3/2}\, p_e^{\frac{1}{2}} + \frac{\partial E_I}{\partial t}\right] B_z \qquad (4.2.18)$$

This leaves us with the problem of finding a suitable method to solve the three time dependent non-linear, second order, coupled, partial differential equations, (4.2.15), (4.2.16) and (4.2.18), numerically.

4.3 CONCISE REPRESENTATION OF THE EQUATIONS

The equations we wish to solve,((4.2.15), (4.2.16) and (4.2.18)) may be written more concisely using vector notation and a summation convention. We define a three component vector $\underline{U}$ which has components :

$$\underline{U}(U_1, U_2, U_3) \qquad U_1 \equiv n, \quad U_2 \equiv p_e, \quad U_3 \equiv B_z$$

then we may represent equations (4.2.15), (4.2.16) and (4.2.18) with one equation, namely,

$$\frac{\partial U_i}{\partial t} = \sum_{m=1}^{3} \left[\frac{\partial}{\partial x}\left(K_{im} \frac{\partial U_m}{\partial x}\right) + \sum_{\ell=1}^{3} Q_{im\ell} \frac{\partial U_m}{\partial x} \frac{\partial U_\ell}{\partial x}\right.$$

$$\left. + R_{im} \frac{\partial U_m}{\partial x} + S_{im} U_m\right] \qquad (4.3.1)$$

where i = 1,3 i.e. if i = 1 we obtain equation (4.2.15) (U_1 = n) and so on.

Identifying the components of the matrices K_{im} $Q_{im\ell}$, R_{im} and S_{im} with the coefficients in equations (4.2.15), (4.2.16) and (4.2.18) we find :

$$K = \begin{bmatrix} U_1 g\Gamma & U_1 g\Theta & 0 \\ \frac{5}{3} U_2 g\Gamma - \frac{U_2}{U_1}\Phi & \frac{5}{3} U_2 g\Theta + \Phi & 0 \\ U_3 g\Gamma & U_3 g\Theta & 2\Lambda \end{bmatrix} \qquad (4.3.2)$$

$$Q_{i=1} = g \begin{bmatrix} -T_i [U_1 g\Gamma + \frac{\Lambda}{3}] & \frac{gU_1}{2}[\frac{\Gamma}{3} + T_i\Theta] - \frac{\Lambda}{3} & 0 \\ \frac{gU_1}{2}[\frac{\Gamma}{3} + T_i\Theta] - \frac{\Lambda}{3} & -\frac{U_1 g\Theta}{3} & 0 \\ 0 & 0 & \frac{4}{\pi_e} U_1 \frac{\Lambda}{3} \end{bmatrix}$$

(4.3.3)

$$Q_{i=2} = g \begin{bmatrix} -\frac{5}{3} U_2 g T_i \Gamma & -\frac{\Gamma}{6}[2 + \frac{5}{3} gU_2] & 0 \\ & -\frac{T_i}{6}[2\Lambda + 5gU_2\Theta] & \\ -\frac{\Gamma}{6}[2 + \frac{5}{3} gU_2] & -\frac{\Theta}{3}[2 + \frac{5}{3} gU_2] & 0 \\ -\frac{T_i}{6}[2\Lambda + 5gU_2\Theta] & \frac{2}{3}\Lambda & \\ 0 & 0 & \frac{4}{\pi_e}\frac{\Lambda}{3g}[2 + \frac{5}{3} U_2 g] \end{bmatrix}$$

(4.3.4)

$$Q_{i=3} = g \begin{bmatrix} -U_3 g T_i \Gamma & \frac{U_3 g}{2}[T_i\Theta + \frac{\Gamma}{3}] & \frac{T_i \Lambda}{3} \\ \frac{U_3 g}{2}[T_i\Theta + \frac{\Gamma}{3}] & \frac{U_3 g \Theta}{3} & -\frac{\Lambda}{3} \\ \frac{T_i \Lambda}{3} & -\frac{\Lambda}{3} & \frac{4}{\pi_e}\frac{U_3 \Lambda}{3} \end{bmatrix} \qquad (4.3.5)$$

where $\Gamma = \frac{2}{\pi_e \varepsilon}\frac{\chi_{\perp e} p_e}{U_1^2}$, $\Theta = \frac{2}{\pi_e \sigma} - \frac{2\chi_{\perp e}}{\pi_e \varepsilon U_1}$

$$\Lambda = \frac{1}{\pi_e \sigma} \quad \text{and} \quad \Phi = \frac{2\chi_{\perp e}}{\pi_e \varepsilon U_1} \qquad (4.3.6)$$

$$R_{im} = - [\text{integral terms} + c(t)]\ \delta_{im} \qquad (4.3.7)$$

where δ_{im} is the Kronecker delta function i.e. $\delta_{im} = 1$ if $i = m$ and $\delta_{im} = 0$ if $i \neq m$.

$$S = \begin{bmatrix} g(\Psi + \frac{\partial E_I}{\partial t}) & 0 & 0 \\ 0 & \frac{5}{3} g\ (\Psi + \frac{\partial E_I}{\partial t}) - \frac{\Psi}{U_2} & 0 \\ 0 & 0 & g(\Psi + \frac{\partial E_I}{\partial t}) \end{bmatrix} \qquad (4.3.8)$$

where $\Psi = -\frac{2}{3} A_F^2 E_z^2 \sigma + \frac{2U_1(U_2 - U_1 T_i)}{\sigma} + \frac{2}{3} R\, U_1^{3/2}\, U_2^{1/2}$

4.4 DIFFERENCE SCHEME

There are very few guidelines for choosing difference schemes for non-linear initial-value problems. All the literature on the subject of difference methods deals with linear or very simple non-linear

equations. The approach taken here is to choose a difference method based on its merits for performance on similar, but much simpler, equations of the same type as the system of equations (4.3.1) which is essentially parabolic. We use the Crank Nicholson implicit difference scheme which has the following advantages and disadvantages :

a) It is accurate to second order in both the time step and the space step.

b) As it is an implicit method we shall be able to use a larger time step than if an explicit method were used. This scheme is unconditionally stable for equations with one independent variable regardless of choice of time step. However, we shall have to perform some "local" stability analysis on the linearised form of the equations. Whether or not these stability tests are sufficient can only practically be assessed by the feasibility of the results. Practical experience shows that instabilities usually start as local phenomena [27] which gives confidence in this local stability approach.

c) The accuracy and stability of the scheme will be obtained at the expense of a more complex set of equations for the variables as a function of time and space.

In difference form, the system of equations described by (4.3.1) becomes,

$$U_{ij}^{p+1} = U_{ij}^{n} + \frac{\Delta t \phi}{\Delta x^2} \sum_{m=1}^{3} [\, \bar{K}_{im\, j+\frac{1}{2}} (U_{mj+1}^{p+1} - U_{mj}^{p+1}) - \bar{K}_{im\, j-\frac{1}{2}} (U_{mj}^{p+1} - U_{mj-1}^{p+1}) \,]$$

$$+\frac{\Delta t(1-\phi)}{\Delta x^2}\sum_{m=1}^{3}\left[\bar{K}_{im\ j+\frac{1}{2}}(U^n_{mj+1}-U^n_{mj})-\bar{K}_{im\ j-\frac{1}{2}}(U^n_{mj}-U^n_{mj-1})\right]$$

$$+\frac{\Delta t\phi}{4\Delta x^2}\sum_{m=1}^{3}\sum_{\ell=1}^{3}\left[\bar{Q}_{im\ell j}(U^p_{mj+1}-U^p_{mj-1})(U^{p+1}_{\ell j+1}-U^{p+1}_{\ell j-1})\right]$$

$$+\frac{\Delta t(1-\phi)}{4\Delta x^2}\sum_{m=1}^{3}\sum_{\ell=1}^{3}\left[\bar{Q}_{im\ell j}(U^n_{mj+1}-U^n_{mj-1})(U^n_{\ell j+1}-U^n_{\ell j-1})\right]$$

$$+\frac{\Delta t\phi}{2\Delta x}\sum_{m=1}^{3}\bar{R}_{imj}(U^{p+1}_{mj+1}-U^{p+1}_{mj-1})+\frac{\Delta t(1-\phi)}{2\Delta x}\sum_{m=1}^{3}\bar{R}_{imj}(U^n_{mj+1}-U^n_{mj-1})$$

$$+\Delta t\phi\sum_{m=1}^{3}\bar{S}_{imj}U^{p+1}_{mj}+\Delta t(1-\phi)\sum_{m=1}^{3}\bar{S}_{imj}U^n_{mj} \qquad (4.4.1)$$

where the subscript j denotes the space mesh point, the superscript n the time step and the superscript p refers to the p^{th} iteration step during the time interval $\Delta t = t^{n+1} - t^n$. Also, $\Delta x = x_{j+1} - x_j$. Values of the variable $\underline{U}$ (U_1,U_2,U_3) at the previous iteration step p are used to define the time average for the coefficients,

$$\bar{K} = \frac{1}{2}K(\underline{U}^p) + \frac{1}{2}K(\underline{U}^n), \qquad \bar{Q} = \frac{1}{2}Q(\underline{U}^p) + \frac{1}{2}Q(\underline{U}^n)$$

$$\bar{R} = \frac{1}{2}R(\underline{U}^p) + \frac{1}{2}R(\underline{U}^n), \qquad \bar{S} = \frac{1}{2}S(\underline{U}^p) + \frac{1}{2}S(\underline{U}^n) \qquad (4.4.2)$$

During each time step we are required to iterate around the non-linear coefficients K,Q,R and S. To clarify the situation we shall go through the first time step. The values of $\underline{U}^n_j(U_1,U_2,U_3)$ are known for all j at time step n; these are the initial conditions. To start the iteration procedure we assume that $\underline{U}_j$ after one iteration will be very close to the known initial conditions for all j i.e. put $\underline{U}^p_j = \underline{U}^n_j$ so that, for the first iteration $\bar{K} = K(\underline{U}^n)$ etc. Therefore the only unknowns in (4.4.1) are $\underline{U}^{p+1}_j$, that is, the first approximation for the values of $\underline{U}$

at the new time level n+1. Furthermore, the system of equations in (4.4.1) is first order in the unknowns $\underline{U}_j^{p+1}$ and can be rearranged to give a matrix equation of the form,

$$A\underline{U}^{p+1} = W \qquad (4.4.3)$$

(The exact form of the matrix equation (4.4.3) and its method of solution is discussed in the next section.) Having solved this matrix equation and obtained our first approximation to $\underline{U}$ at the new time level n+1, the procedure is repeated. That is $\underline{U}_j^{p+1}$ is now called $\underline{U}_j^{p}$, the coefficients in (4.4.2) are calculated again and a second approximation for $\underline{U}_j^{n+1}$ obtained. Hopefully, after a number of iterative steps, convergence is achieved,

$$\lim_{p\to\infty} \underline{U}^{p+1} = \underline{U}^{p}$$

then $\underline{U}^{p+1}$ is the required solution at the time step n+1 [28].

$$\underline{U}^{n+1} = \lim_{p\to\infty} U^{p+1}$$

If $\phi = \frac{1}{2}$ in (4.4.1) the method (in the limit) described is the Crank Nicholson implicit difference method. If $\phi = 0$, the method is explicit and if $\phi = 1$ the scheme is fully implicit. For very little extra work, we have left ourselves the option of varying ϕ. This proved to be of use particularly when testing the computer programs.

4.5 THE MATRIX EQUATION, $A\underline{U}^{p+1} = W$, AND BOUNDARY CONDITIONS

The matrix equation (4.4.3) is obtained by rearranging (4.4.1)

and collecting the coefficients of $\underline{U}_{j-1}^{p+1}(U_1,U_2,U_3)$, $\underline{U}_{j}^{p+1}(U_1,U_2,U_3)$ and $\underline{U}_{j+1}^{p+1}(U_1,U_2,U_3)$. These coefficients then form the matrix A which is block tridiagonal, whilst the remaining known terms form the column vector W.

The system of difference equations (4.4.1) can be written,

$$\alpha_j \, U_{j+1}^{p+1} + \beta_j \, U_j^{p+1} + \gamma_j \, U_{j-1}^{p+1} = W_j \tag{4.5.1}$$

where α, β and γ are 3x3 matrices and U^{p+1} and W are 3 component column vectors. Identifying the elements of the matrices α, β and γ and the elements of the column vector W with the coefficients of $U_{1,2,3j+1}^{p+1}$, $U_{1,2,3j}^{p+1}$, $U_{1,2,3j-1}^{p+1}$ and the remaining terms respectively we find,

$$\alpha_{imj} = \frac{\Delta t\phi}{\Delta x^2} \left[\bar{K}_{im\ j+\frac{1}{2}} + \frac{1}{4} \sum_{\ell=1}^{3} \bar{Q}_{im\ell j} (U_{\ell j+1}^{p} - U_{\ell j-1}^{p}) \right] + \frac{\Delta t\phi}{2\Delta x} \bar{R}_{imj} \tag{4.5.2}$$

$$\beta_{imj} = -\delta_{im} - \frac{\Delta t\phi}{\Delta x^2} \left[\bar{K}_{im\ j+\frac{1}{2}} + \bar{K}_{im\ j-\frac{1}{2}} \right] + \Delta t\phi \, \bar{S}_{imj} \tag{4.5.3}$$

$$\gamma_{imj} = \frac{\Delta t\phi}{\Delta x^2} \left[\bar{K}_{im\ j-\frac{1}{2}} - \frac{1}{4} \sum_{\ell=1}^{3} \bar{Q}_{im\ell j} (U_{\ell j-1}^{p} - U_{\ell j+1}^{p}) \right] - \frac{\Delta t\phi}{2\Delta x} \bar{R}_{imj} \tag{4.5.4}$$

where δ_{im} is the Kronecker delta function i = 1,3 m = 1,3

$$W_{ij} = - U_{ij}^{n} - \Big(\frac{\Delta t(1-\phi)}{\Delta x^2} \sum_{m=1}^{3} \Big[\bar{K}_{im\ j+\frac{1}{2}} (U_{mj+1}^{n} - U_{mj}^{n}) - \bar{K}_{im\ j-\frac{1}{2}} (U_{mj}^{n} - U_{mj-1}^{n}) \Big]$$

$$+ \frac{\Delta t(1-\phi)}{4\Delta x^2} \sum_{m=1}^{3} \sum_{\ell=1}^{3} \Big[\bar{Q}_{im\ell j} (U_{mj+1}^{n} - U_{mj-1}^{n})(U_{\ell j+1}^{n} - U_{\ell j-1}^{n}) \Big]$$

$$+ \frac{\Delta t(1-\phi)}{2\Delta x} \sum_{m=1}^{3} \bar{R}_{imj} \left(U^n_{mj+1} - U^n_{mj-1}\right) + \Delta t(1-\phi) \sum_{m=1}^{3} \bar{S}_{imj} U^n_{mj}\Big) \tag{4.5.5}$$

α, β and γ form the elements of the matrix A which is block tridiagonal because of the three point difference scheme.

Boundary Conditions

Returning to the physics of the problem, we know the optimum wavelength for growth of the electrothermal instability is of the order of a few ion Larmor radii which in Tokamaks is a few centimetres or less. This was our justification (see Chapter 2) for considering the electrothermal instability to be born out of a perturbation about a steady-state plasma with uniform profiles for number density, electron temperature and magnetic and electric fields. For this reason our space mesh must be restricted to a small region over which the above approximation holds. Furthermore, in Section 4 of Chapter 2 we demonstrated that the model we are now using, in which the y-component of the magnetic field is neglected, only holds for wavelengths less than some upper limit. For wavelengths greater than this upper limit the growth rate from this model is much greater than the growth rate from the model with the y-component of the magnetic field included (see Figure 2.4a). An effective and acceptable way of suppressing these long wavelength modes, which could otherwise dominate, is to restrict the space mesh to a size which is equal to the upper wavelength limit.

As we can only represent a small region of space on our mesh, and therefore only a small region of plasma compared with the diameter of a Tokamak, we choose to use periodic boundary conditions because

these are as valid as any and simpler to apply than others.

Let the region of space in which our equations apply be discretely represented by J mesh points. Therefore using periodic boundary conditions we have

$$\underline{U}_{j=1} = \underline{U}_{j=J}$$

and (4.5.6)

$$\left.\frac{\partial \underline{U}}{\partial x}\right|_{j=1} = \left.\frac{\partial \underline{U}}{\partial x}\right|_{j=J}$$

In this case the matrix A in equation (4.4.3) is block perdiagonal (see Figure 4.5).

Figure 4.5 Block Perdiagonal matrix equation.

$$\begin{bmatrix} \beta_1 & \alpha_1 & 0 & \cdots & \gamma_1 \\ \gamma_2 & \beta_2 & \alpha_2 & \cdots & 0 \\ 0 & \gamma_3 & \beta_3 & \alpha_3 & \cdots & 0 \\ \vdots & & & & & \\ \alpha_{J-1} & 0 & \cdots & \gamma_{J-1} & \beta_{J-1} \end{bmatrix} \begin{bmatrix} U_1 \\ U_2 \\ U_3 \\ \\ \\ \\ \\ U_{J-1} \end{bmatrix} = \begin{bmatrix} W_1 \\ W_2 \\ W_3 \\ \\ \\ \\ \\ W_{J-1} \end{bmatrix}$$

α_j, β_j and γ_j are 3x3 matrices whose elements given by (4.5.2) to (4.5.4) and U_j and W_j are 3 component column vectors.

That is, it is block tridiagonal with additional blocks in the upper right and lower left hand corners. The dimensions of the matrix A are 3(J-1)x3(J-1), and the matrix equation has to be solved at each iteration within every time step. Hence we require that the matrix equation be solved rapidly and efficiently. The method and the computer program used are discussed in Appendix A[29]. This computer program is now obtainable from the Computer Physics Communications International Physics Program Library.

4.6 EVALUATION OF THE MATRICES K, Q, R AND S

The evaluation of the elements of the matrices K and Q is fairly straightforward. Equations (4.4.2) tell us that we require the values of the elements of $\bar{K}$ and $\bar{Q}$. These are calculated quite simply by finding the values of the elements using n, p_e and B_z (U_1,U_2 and U_3) at the previous time level n, finding the values of the elements using n, p_e and B_z at the last iteration p and taking the average of the two quantities.

The evaluation of the elements of $\bar{R}$ and $\bar{S}$ is not as simple. Looking at the definitions of R and S, relations (4.3.7) and (4.3.8) respectively, there are three points to notice. Firstly, it is necessary to evaluate an integral numerically at every mesh point j. Secondly, we must find a way of determining the value of $\frac{\partial E_I}{\partial t}$, bearing in mind that it is not a function of space, and thirdly we must find the value of c(t). We recall that c(t) arises as a constant of integration (therefore a constant in space but not in time) when finding an expression for V_x (see equation (4.2.13)).

For clarity we shall repeat the integral terms which have to be evaluated,

$$\text{Integral terms} = \frac{2}{3} A_F^2 E_z^2 \int g\,\sigma\,dx + \frac{1}{3}\left(\frac{2}{\pi_e}\right)^2 \int B_z \frac{\partial}{\partial x}\left(\frac{g}{\sigma}\frac{\partial B_z}{\partial x}\right) dx$$

$$- \frac{2}{\pi_e \varepsilon} \int \left(\frac{\chi_{ie}}{n}\frac{\partial p_e}{\partial x} - \frac{\chi_{ie} p_e}{n^2}\frac{\partial n}{\partial x} - \frac{\varepsilon}{\sigma}\frac{\partial p}{\partial x}\right) g^2 \frac{\partial}{\partial x}\left(\frac{p_e}{3} + p_i\right) dx$$

$$- \int g \left(\frac{2n(p_e - p_i)}{\sigma} + \frac{2}{3} R\, n^{3/2}\, p_e^{1/2}\right) dx - \frac{\partial E_I}{\partial t} \int g\,dx \qquad (4.6.1)$$

where $g = \left(\frac{2B_z^2}{\pi_e} + p + \frac{2}{3} p_e\right)^{-1}$ and $p = p_e + p_i$.

These terms are evaluated by interpreting the integral as the area under the curve and using the Trapezium rule. Generally, if a function $f(x)$ is discretely represented at J mesh points from j=1 to J, then we approximate the value of the integral of $f(x)$ at the point x_j by,

$$\int_{x_j} f(x)\,dx \approx \sum_{j=1}^{j-1} (f_j + f_{j+1}) \frac{\Delta x}{2} \qquad (4.6.2)$$

Equation (4.6.2) is applied to every term in equation (4.6.1). The gradient terms are dealt with in the usual way.

The constant of integration c(t) is determined by specifying the centre of mass velocity, V_x, at the left hand boundary i.e. $V_{xj=1}$. As the boundary conditions are periodic,

$$V_{xj=1} = V_{xj=J} \qquad (4.6.3)$$

The $\hat{x}$-direction corresponds to the radial direction in a Tokamak so there cannot be a net flow in the $\hat{x}$ direction. Therefore, we choose,

$$V_{xj=1} = V_{xj=J} = 0 \quad \text{for all } t \qquad (4.6.4)$$

Looking at equation (4.2.13) we can now determine c(t). At j=1 the integral terms are all zero therefore, putting $V_{xj=1}$ to zero, we have,

$$c(t) = \left(\frac{2}{3}\frac{2g}{\pi_e\sigma}\frac{\partial p}{\partial x} - \frac{2g}{\pi_e\varepsilon}\left(\frac{\chi_{\perp e}}{n}\frac{\partial p_e}{\partial x} - \frac{\chi_{\perp e}p_e}{n^2}\frac{\partial n}{\partial x}\right)\right)_{j=1} \qquad (4.6.5)$$

Finally, we must evaluate $\frac{\partial E_I}{\partial t}$. This is done by making use of the fact that $\frac{\partial E_I}{\partial t}$ is not a function of space together with the right hand boundary conditions, $V_x = 0$ at $j = J$. Applying equation (4.2.13) at the point j=J and rearranging we obtain an expression for $\frac{\partial E_I}{\partial t}$,

$$\frac{\partial E_I}{\partial t} = \Big[\frac{2}{3}A_F{}^2E_z{}^2\int g\,\sigma\,dx + \frac{1}{3}\left(\frac{2}{\pi_e}\right)^2\int B_z\frac{\partial}{\partial x}\left(\frac{g}{\sigma}\frac{\partial B_z}{\partial x}\right)dx$$

$$- \frac{2}{\pi_e\varepsilon}\int\left(\frac{\chi_{\perp e}}{n}\frac{\partial p_e}{\partial x} - \frac{\chi_{\perp e}p_e}{n^2}\frac{\partial n}{\partial x} - \frac{\varepsilon}{\sigma}\frac{\partial p}{\partial x}\right)g^2\frac{\partial}{\partial x}\left(\frac{p_e}{3} + p_i\right)dx$$

$$- \int g\left(\frac{2n(P_e - p_i)}{\sigma} + \frac{2}{3}R\,n^{3/2}\,p_e{}^{1/2}\right)dx\Big]/\int g\,dx \qquad (4.6.6)$$

all evaluated at j=J.

where the periodic boundary conditions have been used to eliminate the non integral terms in equation (4.2.13) to get equation (4.6.6).

4.7 LOCAL STABILITY ANALYSIS FOR THE DIFFERENCE SCHEME

For the difference scheme to be considered numerically stable we require that any error in the result is reduced from one time step to the next. The system of difference equations (4.4.1) couples both the dependent variables U_1,U_2 and U_3, which comprise the state of the system, and different points on the space mesh. Before determining the stability we simplify the problem by decoupling points on the space mesh. This is done, in the usual way, by studying the Fourier modes on the mesh separately and by demanding that the scheme is stable for every Fourier mode.

It is generally accepted that lower order terms do not affect the stability of diffusion type problems, such as we have[27]. However,

their presence may force one to use smaller time steps, e.g. a large source term causes rapid changes in $\underline{U}$ so that a small time step is required. For this reason, and for simplicity, we shall examine the stability of the difference scheme applied to the system of equations (4.3.1) neglecting terms of order lower than the second. That is applied to,

$$\frac{\partial U_i}{\partial t} = \sum_{m=1}^{3} \frac{\partial}{\partial x} \left(K_{im} \frac{\partial U_m}{\partial x}\right) \tag{4.7.1}$$

Furthermore, we shall assume K_{im} to be constant. The stability conditions obtained are then "local conditions" and must be satisfied everywhere on the space mesh for all time steps. The difference scheme applied to (4.7.1), if the elements of K_{im} are considered constant, gives,

$$U_{ij}^{n+1} = U_{ij}^{n} + \sum_{m=1}^{3} \frac{K_{im}\Delta t\phi}{\Delta x^2} \left(U_{ij+1}^{n+1} - 2U_{ij}^{n+1} + U_{ij-1}^{n+1}\right)$$

$$+ \sum_{m=1}^{3} \frac{K_{im}(1-\phi)\Delta t}{\Delta x^2} \left(U_{ij+1}^{n} - 2U_{ij}^{n} + U_{ij-1}^{n}\right) \tag{4.7.2}$$

Analysing the method for a Fourier mode,

$$U_{ij} = \hat{U}_i e^{ikx} = \hat{U}_i e^{ikj\Delta x} \tag{4.7.3}$$

we obtain,

$$\hat{U}_i^{n+1} e^{ikj\Delta x} = \hat{U}_i^{n} e^{ikj\Delta x} + \sum_{m=1}^{3} \frac{K_{im}\Delta t\phi}{\Delta x^2} \hat{U}_m^{n+1} e^{ikj\Delta} \left(e^{ik\Delta x} - 2 + e^{-ik\Delta x}\right)$$

$$+ \sum_{m=1}^{3} \frac{K_{im}\Delta t(1-\phi)}{\Delta x^2} \hat{U}_m^{n} e^{ikj\Delta x} \left(e^{ik\Delta x} - 2 + e^{-ik\Delta x}\right) \tag{4.7.4}$$

Now, using $e^{ik\Delta} + e^{-ik\Delta} = 2 \cos k\Delta x$

and $2(\cos k\Delta x - 1) = -4 \sin^2 \frac{k\Delta x}{2}$ (4.7.5)

in (4.7.4) and dividing through by $e^{ikj\Delta}$, we obtain,

$$\hat{U}_i^{n+1} = \hat{U}_i^n - \sum_{m=1}^{3} \frac{\Delta t\phi}{\Delta x^2} K_{im} \hat{U}_m^{n+1} 4 \sin^2 \frac{k\Delta x}{2}$$

$$- \sum_{m=1}^{3} \frac{\Delta t(1-\phi)}{\Delta x^2} K_{im} \hat{U}_m^n 4 \sin^2 \frac{k\Delta x}{2} \qquad (4.7.6)$$

This equation is of the form,

$$(I + M)\, \underline{\hat{U}}^{n+1} = (I - P)\underline{\hat{U}}^n \qquad (4.7.7)$$

where I is the identity matrix (3x3) and the elements of M and P are,

$$M_{im} = \frac{4\Delta t\phi}{\Delta x^2} \sin^2 \frac{k\Delta x}{2} K_{im}$$

$i=1,3$
$m=1,3$ (4.7.8)

$$P_{im} = \frac{4\Delta t(1-\phi)}{\Delta x^2} \sin^2 \frac{k\Delta x}{2} K_{im}$$

Clearly if $\phi = \frac{1}{2}$ the difference scheme is the Crank Nicholson implicit difference scheme and M = P. Rearranging (4.7.7), we obtain an expression for the amplification matrix $G(\Delta t, \Delta x, k)$ of the difference scheme for the Fourier mode of wavenumber k.

$$\underline{\hat{U}}^{n+1} = G(\Delta t, \Delta x, k)\, \underline{\hat{U}}^n \qquad (4.7.9)$$

where $G = (I + M)^{-1} (I - P)$ (4.7.10)

For stability, if the amplitude of a Fourier mode is finite at time t = 0

then it must be finite for all time steps[28]. This condition imposes a requirement on each of the eigenvalues g_m of the amplification matrix G such that a necessary and sufficient condition for stability is

$$|g_m| \leq 1 \tag{4.7.11}$$

for all modes k and all eigenvalues m.

To find all the eigenvalues of the matrix G is impracticable and unnecessary. We only need to know the magnitude of the largest eigenvalue. Gerschgorin's theorem[30] tells us that the eigenvalue with the largest magnitude of the matrix A is always less than or equal to a certain combination of summations of the elements of A, that is,

$$\rho(A) = \max_i |\lambda_i| \tag{4.7.12}$$

$$\rho(A) \leq \min \left(\max_i \sum_m |a_{im}| ; \max_m \sum_i |a_{im}| \right)$$

where $\rho(A)$ denotes the spectral radius of the matrix A, λ_i are the eigenvalues of A and a_{im} are the elements. The implementation of Gerschgorin's theorem is discussed in more detail in Appendix B.

Finally, it can be shown[27] that the worst case to consider for stability is the Fourier mode with wavenumber k such that,

$$\frac{k\Delta x}{2} = \frac{\pi}{2} \quad \text{or} \quad \lambda = 2\Delta x \tag{4.7.13}$$

This is because it is the smallest wavelength which can be represented on the space mesh. Three mesh points are insufficient to represent one wavelength so that, if the difference scheme adequately deals with this wavenumber and does not allow this mode to dominate the solution, we

can assume the scheme is stable.

4.8 THE COMPUTER PROGRAM

We conclude this chapter with a description of the computer program used to follow the time development of an electrothermal instability using the methods described in the preceding sections.

The initial conditions and the behaviour of E_z

The steady-state condition of the plasma, before the perturbation is applied, is completely described by giving the values of :

$$\omega_o\tau_o, \quad T_i, \quad T_{eo} \text{ and } \pi_e = \frac{8\pi n_o k_B T_{eo}}{B_{zo}^2}$$

The value of A_F is obtained by applying the electron energy equation (4.1.19) to the steady-state, before the perturbation is applied giving,

$$A_F^2 = 3(1 - T_i) + R \qquad (4.8.1)$$

If Bremsstrahlung is not included, it is only necessary to give the ratio T_i/T_{eo} as opposed to both T_i and T_{eo}. The size of the space mesh together with the number of mesh points determines the value of Δx,

$$\Delta x = \frac{\text{mesh length}}{J-1} = \frac{\lambda_m}{J-1} \qquad (4.8.2)$$

The perturbations in n, p_e and B_z are chosen such that :

a) total mass is conserved, $\sum_{j=1}^{J-1} (n_j+n_{j+1}) \frac{\Delta x}{2} = \lambda_m$

b) Pressure balance is obeyed, $(p + \frac{B_z^2}{\pi_e})$ is not a function of j.

c) The mesh length, λ_m, is less than the cut off wavelength above which the model is not valid (see Chapter 2, section 4).

d) This value is obtained from linear theory, given $\omega_o\tau_o$, T_i, T_{eo} and π_e. Periodic boundary conditions are observed.

The value of ϕ must be given at the beginning of each run. This determines whether the difference scheme is explicit ($\phi = 0$), implicit ($0 < \phi < 1$) or fully implicit ($\phi = 1$).

E_z is not an independent variable in the problem. However, we consider two ways of treating this parameter which are consistent with both the linear model and the non-linear steady-state problem considered in Chapter 3. The first set of results are obtained with E_z constant in time as well as uniform in space. The remaining results are obtained by imposing the more realistic constraint of constant total current,

$$\int_o^{\lambda_m} j_z \, dx \approx \sum_{j=1}^{J-1} (j_{zj} + j_{zj+1}) \frac{\Delta x}{2} = \lambda_m \qquad (4.8.3)$$

Hence the applied electric field is chosen at each time step such that the above relation (4.8.3) is satisfied. Using Ohm's Law, equation (4.1.18), E_z is given by,

$$E_z(t) = \frac{\lambda_m}{\sum_{j=1}^{J-1} (\sigma_j + \sigma_{j+1}) \frac{\Delta x}{2}} \qquad (4.8.4)$$

(The total current is equal to λ_m because we are working in dimensionless units normalised to the initial values.)

The main program

The perturbations together with the initial steady-state conditions determine $\underline{U}^n$. The subroutine TPORT calculates the electrical conductivity σ_j^n and the electron thermal conductivity $\chi_{\perp j}^n$ at every mesh point j=1, J-1. These values are used in subroutine KAPQ to find the elements of the matrices K and Q at level n for all j. Now that K is known a stable time step Δt can be obtained. A first approximation for Δt is chosen intuitively. Subroutine DTIME (see Appendix B) tests the stability of the difference scheme with this value of Δt at every mesh point. If this value of Δt fails the stability test it is halved and the stability test performed again. This process is repeated until a stable time step is found. Subroutine RSUMS is used to evaluate $\frac{\partial E_I^n}{\partial t}$ (equation (4.6.6)) and $c(t)^n$ (equation (4.6.5)), and then used to evaluate the elements of the matrices R and S. The right hand side of equation (4.5.1) W_j is a column vector whose elements are given by (4.5.5). These are calculated by a subroutine called RHS. Similarly the elements of the matrices α, β and γ, given by equations (4.5.2) to (4.5.4), are calculated by subroutine ALBGAM. Subroutine PERDIAG is called upon to solve the matrix equation (4.4.3) hence giving a first approximation to $\underline{U}^{n+1}$ called $\underline{U}^p$. E_z^p is updated, if necessary, using equation (4.8.4)

TPORT is called to find σ_j^p and $\chi_{\perp j}^p$ and KAPQ to find K^p and Q^p. In practice it is not found necessary to test the stability of the time step at every iteration, or even at every time step. Hence we move to RSUMS which gives us the elements of R^p and S^p. With these new values for K, Q, R and S we use relations (4.4.2) to find the time averaged values, $\bar{K}$, $\bar{Q}$, $\bar{R}$ and $\bar{S}$. Subroutines RHS and ALBGAM are again called upon to find "A" and "W" of the matrix equation (4.4.3) which is again solved by PERDIAG. We now have a second approximation for $\underline{U}^{n+1}$ which we call $\underline{U}^p$. The process described in this paragraph is repeated until convergence is achieved.

A test for convergence

A convergence test which proved satisfactory in most cases may be described with the following inequality,

$$\left| \frac{\underline{U}_j^{p+1} - \underline{U}_j^{p}}{\underline{U}_j^{n} - \underline{U}_j^{1}} \right| \leq b \quad \text{for all } j \qquad (4.8.5)$$

$\underline{U}^1$ = 1st approximation to $\underline{U}^{n+1}$

where b was varied from 10^{-2} to 10^{-3}. This test for convergence obviously breaks down when the system is tending towards a steady-state in which case,

$$\underline{U}_j^{n} \simeq \underline{U}_j^{n+1} \qquad (4.8.6)$$

and therefore the denominator in (4.8.5) is very small, so that the accuracy demanded by (4.8.5) is unreasonable. However, the approach of a steady-state would also be indicated by the behaviour of other parameters e.g. $\frac{\partial E_I}{\partial t}$ and V_x tending to zero. At other times we can compare the value of $\frac{\partial E_I}{\partial t}$, calculated using the condition that $V_x = 0$ at $j = J$, to the values obtained using the converged results as another test for convergence.

In summary, the test for convergence given by (4.8.5) on its own is possibly inadequate. However, used in conjunction with other tests it is acceptable.

Further program tests

Other functions performed by the program include a test to verify that mass is conserved. We cannot expect exact mass conservation because the equations were not differenced conservatively, so that truncation errors will be present as well as the ever present round off

errors. However, we do expect mass conservation within a few percent, otherwise the difference equations do not even approximately represent the differential equations. Therefore, in the program we calculate the quantity,

$$\sum_{j=1}^{j=J-1} (n_j+n_{j+1}) \frac{\Delta x}{2}$$

and print its value every n timesteps, where n is specified according to the particular run.

We also check that the internal energy

$$p_j + \frac{B_{z\,j}^2}{\pi_e} = E_I \tag{4.8.7}$$

does not vary significantly with j. We calculate the internal energy E_I at every mesh point j and find the mean value of E_I, that is,

$$\bar{E}_I = \frac{1}{J} \sum_{j=1}^{J} E_{Ij} \tag{4.8.8}$$

The standard deviation from the mean is then given by

$$S_d^2 = \frac{1}{J} \sum_{j=1}^{J} (E_{Ij} - \bar{E}_I)^2$$

We arbitrarily impose the condition that the standard deviation from the mean should be less than one percent of the mean value of E_I,

$$\frac{S_d}{\bar{E}_I} < 10^{-2} \tag{4.8.9}$$

If this condition is not satisfied subroutine PROBLEM is called which prints out an error message together with the time step at which it

occurred and the program stops.

CHAPTER 5

RESULTS FROM THE TIME DEPENDENT MODEL

INTRODUCTION

This chapter consists of two distinct sections. In the first section we present the results obtained from following the evolution of the electrothermal instability when the applied electric field E_z is considered to be held constant for all time. The second section deals with the results obtained for the more realistic situation experimentally of E_z varying in time in such a way as to keep the total current constant.

5.1 CONSTANT FIELD E_z

A random perturbation is applied to a steady-state system. The evolution of the perturbation is followed numerically assuming the applied electric field E_z is constant for all time. For a given set of initial conditions, about which the perturbation is applied, the cut off wavelength, λ_m, above which this model is invalid, is found from linear theory. The length of the mesh is set equal to λ_m. The perturbation is chosen such that total mass is conserved,

$$\sum_{j=1}^{J-1} (n_j + n_{j+1}) \frac{\Delta x}{2} = \lambda_m = \Delta x(J-1) \qquad (5.1.1)$$

and such that the quantity E_I is not a function of j. The perturbations in p_e and B_z are chosen using a random number generator for j=1, J-1. Writing equation (4.2.11) in discrete form we have,

$$p_{ej} + n_j T_i + \frac{B_{zj}^2}{\pi_e} = c_1 \quad \text{for all } j \tag{5.1.2}$$

where c_1 is an unknown constant. Using (5.1.2) as an expression for the number density n we may rewrite equation (5.1.1) which can be rearranged to give the value of the constant c_1 in terms of known quantities.

$$c_1 = T_i + \frac{1}{2(J-1)} \sum_{j=1}^{J-1} \left(p_{ej} + p_{ej+1} + \frac{(B_{zj}^2 + B_{zj+1}^2)}{\pi_e}\right) \tag{5.1.3}$$

Having found the value of c_1 we can use equation (5.1.2) to find n_j for j=1, J-1. The amplitude of the perturbation is chosen so that the effects produced by second order terms are negligible. The minimum number of mesh points required for a particular run can be approximated from linear theory. For a given set of initial conditions we know the wavelength, λ_s, below which all modes are damped. Hence for the difference scheme to be able to handle the shortest growing wavelength we require,

$$\Delta x \leq \frac{\lambda_s}{4} \tag{5.1.4}$$

so that this mode is acceptably resolved.

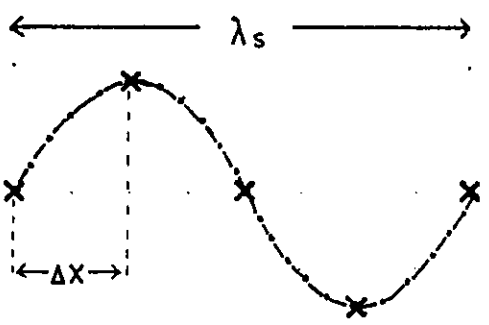

Figure 5.1 The minimum number of mesh points required to represent λ_s adequately.

This condition implies that,

$$J \geq 1 + 4 \frac{\lambda_m}{\lambda_s} \tag{5.1.5}$$

In order to assist the analysis of the results obtained, we discretely Fourier analyse the profiles for the number density n, the electron temperature T_e and the magnetic field, B_z, as these are the independent variables in the problem. In this way, we can also check that the amplitude of the smallest wavelength on the mesh is insignificant at all times. If this is found not to be true a finer mesh must be used and the time step changed accordingly. The discrete function f_j periodic in J such that,

$$f_1 = f_J$$

which is neither an odd nor an even function may be represented exactly at the mesh points by the trigonometric series,

$$f_j = \frac{a_o}{2} + \sum_{n=1}^{\frac{J-1}{2}} \left(a_n \cos \frac{2n\pi(j-1)}{J-1} + b_n \sin \frac{2n\pi(j-1)}{J-1}\right) \tag{5.1.6}$$

where the coefficients a_o, a_n and b_n are defined,

$$a_o = \frac{2}{(J-1)} \sum_{j=1}^{J-1} f_j$$

$$a_n = \frac{\sum_{j=1}^{J-1} f_j \cos \frac{2n\pi(j-1)}{J-1}}{\sum_{j=1}^{J-1} \cos^2 \frac{2n\pi(j-1)}{J-1}}$$

$$b_n = \frac{\sum_{j=1}^{J-1} f_j \sin \frac{2n\pi(j-1)}{J-1}}{\sum_{j=1}^{J-1} \sin^2 \frac{2n\pi(j-1)}{J-1}} \tag{5.1.7}$$

The denominators in the expressions for a_n and b_n are exactly equal to $\frac{2}{J-1}$ in the limit of f being a continuous function. However, for the discrete case they only approximate to $\frac{2}{J-1}$. In practice the deviation from $\frac{2}{J-1}$ was found to be insignificant and certainly no bigger than round off error for small n.

Many runs on the computer were performed to follow the growth of the electrothermal instability keeping E_z constant and applying a random perturbation in the manner previously described. Results obtained with different numbers of mesh points were compared. Also results were compared at the same time, $t = n\Delta t$, for different values of n and Δt. These tests allow us to check the accuracy of the results.

Figure (5.2a) is a plot of the dimensionless perturbed electron temperature profiles at different times in the earlier stages of the run. (These particular plots were obtained with the random number generator choosing values between $\pm 5 \times 10^{-4}$. However the same behaviour pattern persists with even smaller values for the magnitudes of the initial perturbations.) We can see from these profiles how the longer wavelength modes quickly dominate. Figure (5.2b) shows the electron temperature profiles at later times, whilst figures (5.2c-g) show the corresponding profiles for the number density, the $\hat{y}$ and $\hat{z}$ components of the current density, the centre of mass velocity and the magnetic field respectively. As expected, we can see that the density peaks in the electron temperature troughs and vice versa. Also, at all times, the perturbed current density in the $\hat{y}$ direction is always very much smaller than that in the $\hat{z}$ direction. Returning to the electron temperature profiles, Figure (5.2b), by this time the longest wavelength mode on the mesh is very much stronger than all shorter wavelength modes. However we also observe that the average electron temperature is increasing in time. That is the infinite wavelength mode is growing as

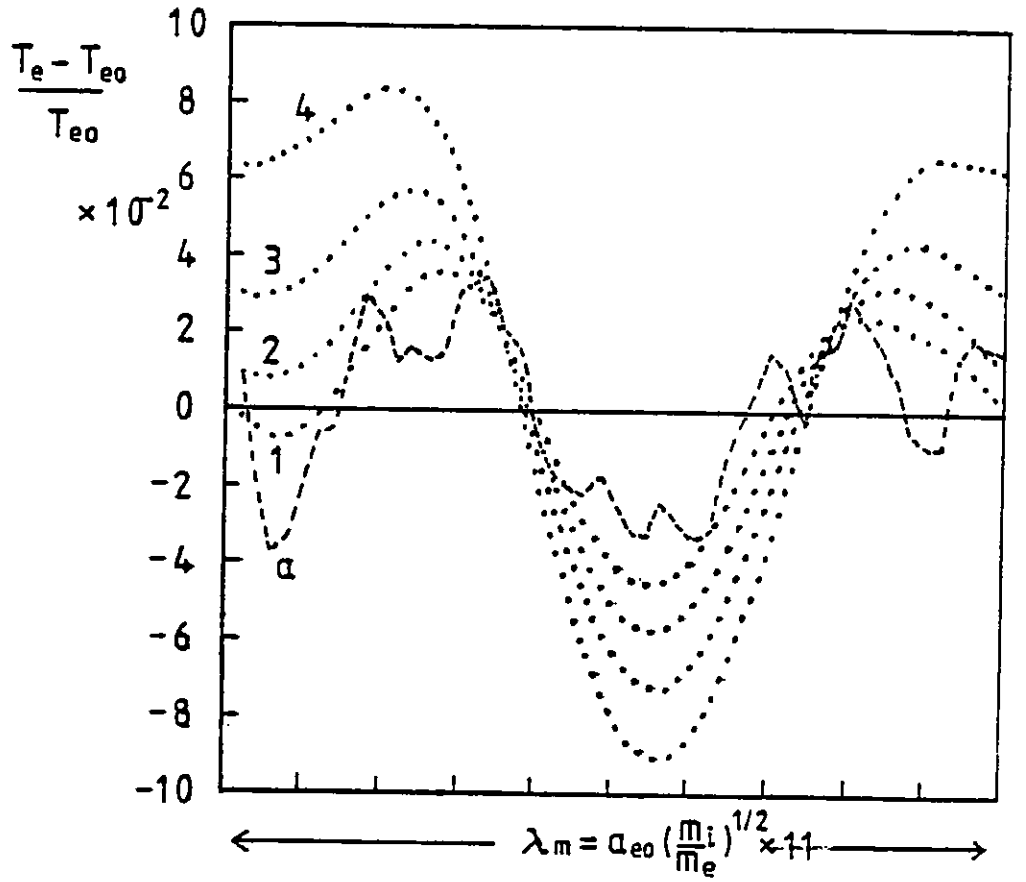

Figure 5.2a Electron temperature profiles at :

a) dimensionless time $t = 5\times10^{-2}$

1) $t = 0.5$
2) $t = 1.0$
3) $t = 1.5$
4) $t = 2.0$

Figures 5.2

Results from numerical model with electric field E_z held constant

$\omega_o\tau_o = 1.54\times10^{6}$, $\pi_e = 2.2667\times10^{-2}$, R = 0, $T_i/T_{eo} = 0.5$
Mesh length set to eleven scale lengths.

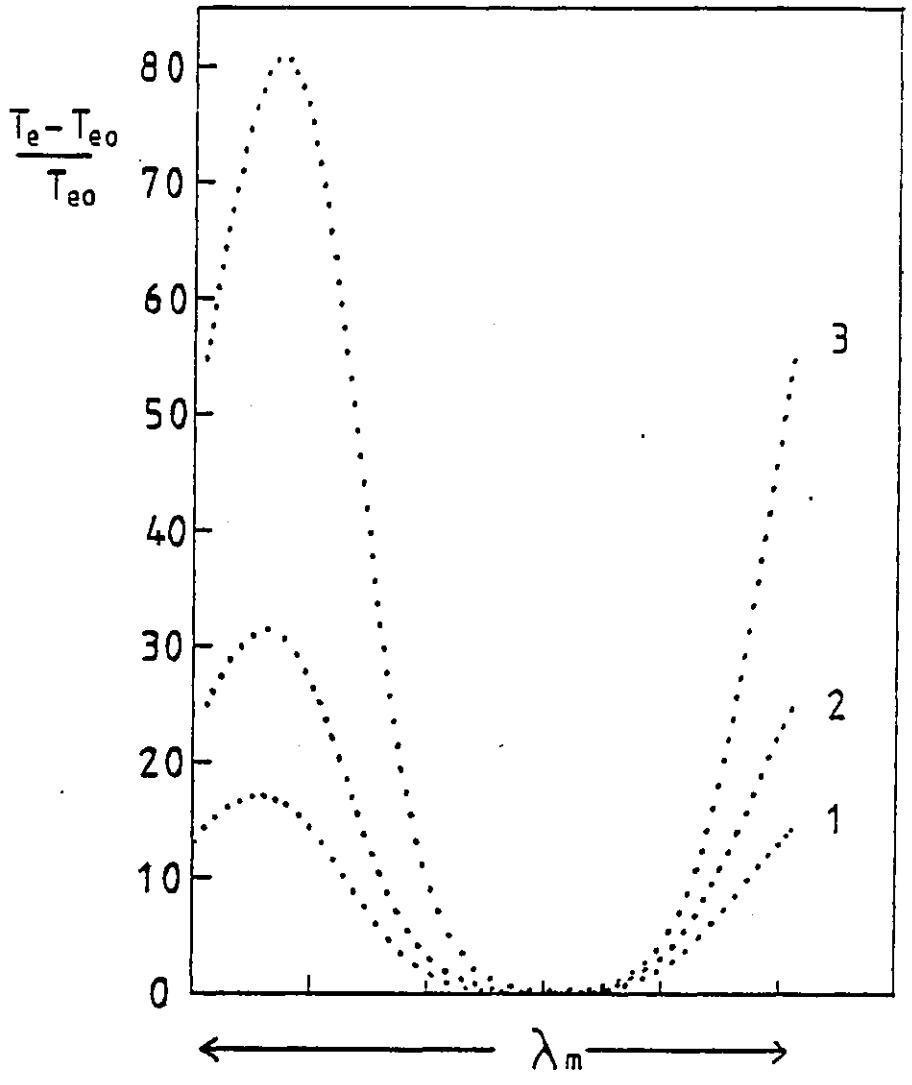

Figure 5.2b Electron temperature profiles at :

1) dimensionless time t = 5.0
2) t = 5.1
3) t = 5.2

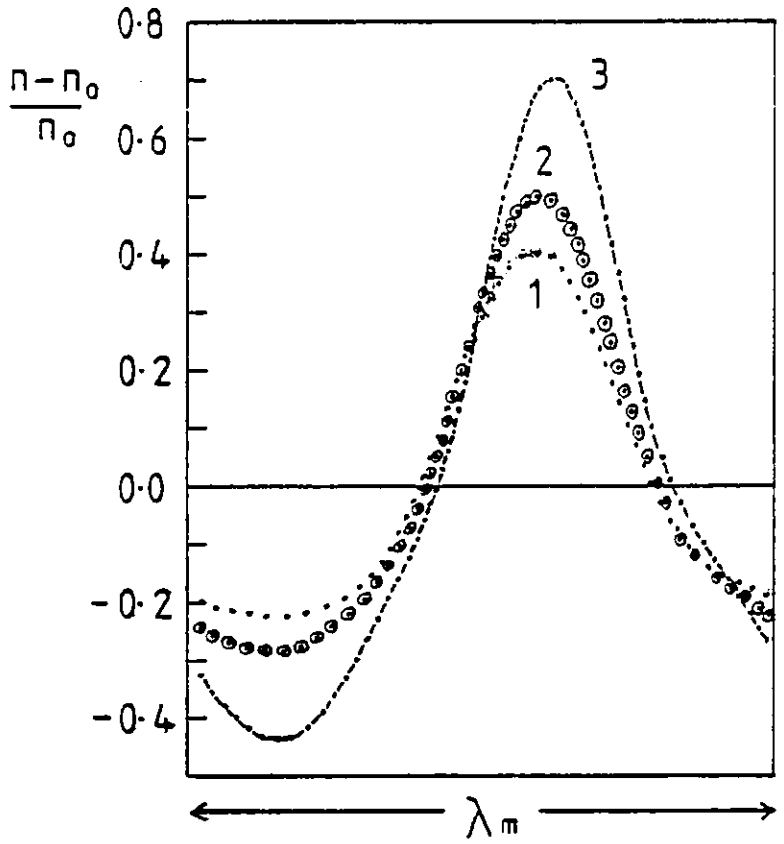

Figure 5.2c Number density profiles at :

1) dimensionless time t = 5.0
2) t = 5.1
3) t = 5.2

Figure 5.2d z-component of current density profiles at :

1) dimensionless time t = 5.0
2) t = 5.1
3) t = 5.2

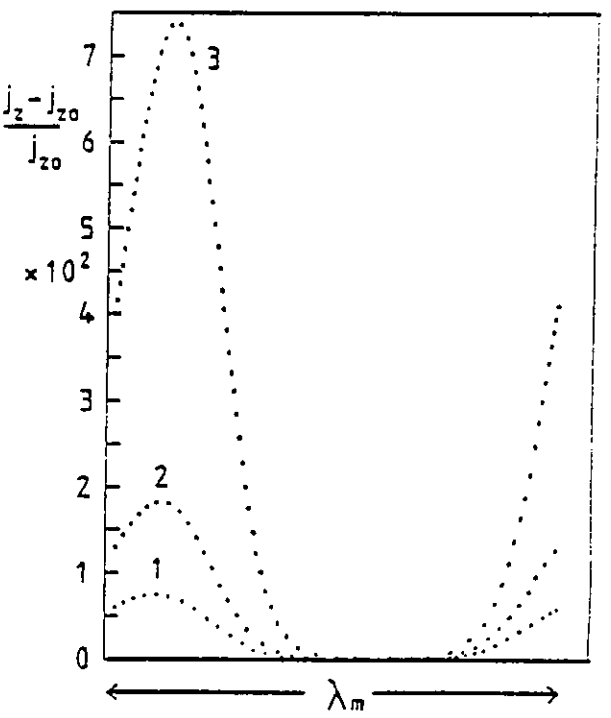

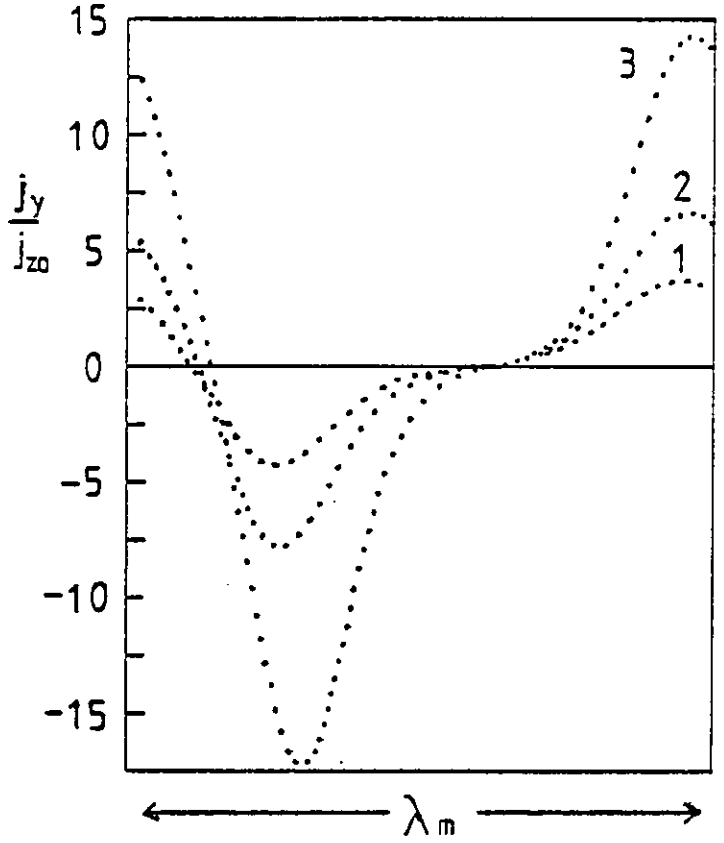

Figure 5.2e y-component of current density at :

1) dimensionless time t = 5.0
2) t = 5.1
3) t = 5.2

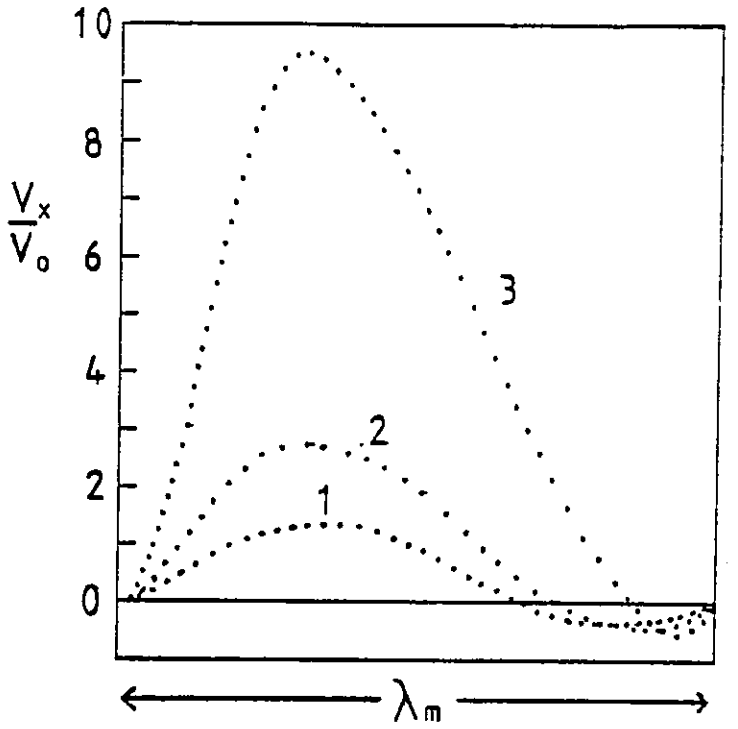

Figure 5.2f Centre of mass velocity profiles at :

1) dimensionless time t = 5.0
2) t = 5.1
3) t = 5.2

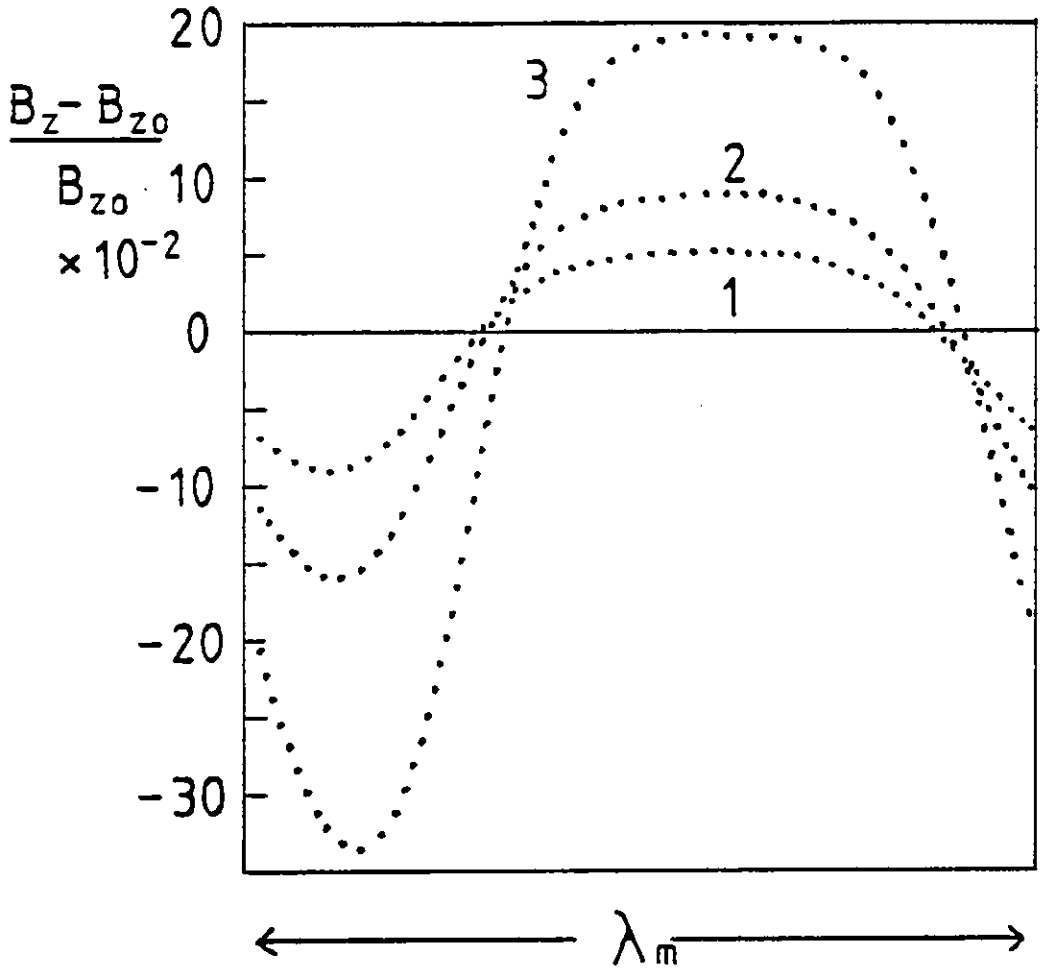

Figure 5.2g z-component of the magnetic field at :

1) dimensionless time t = 5.0
2) t = 5.1
3) t = 5.2

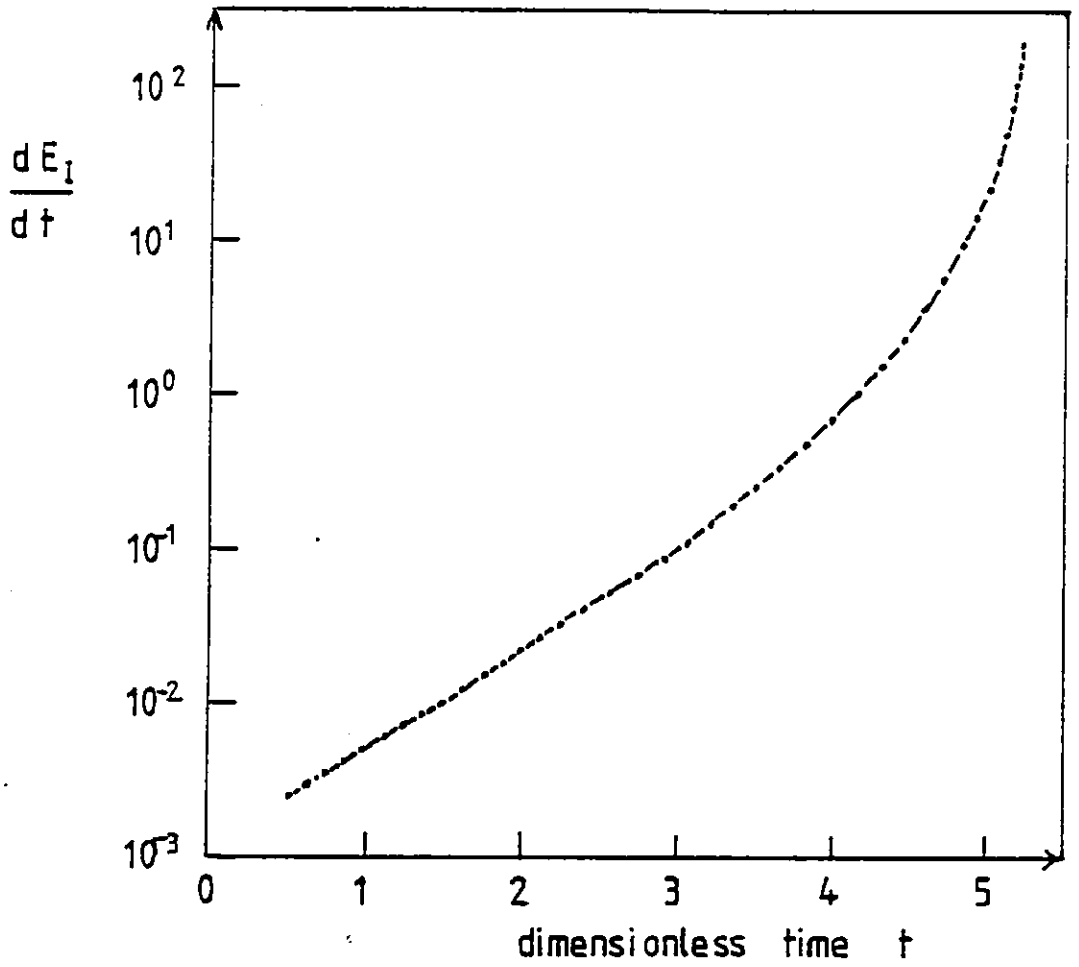

Figure 5.2h The rate of change of the internal energy against time.

well. These observations are quantified by looking at the values of the Fourier coefficients a_o, a_n and b_n as a function of time, Table (5.1). We print here the values of a_n and b_n for n = 1 and n = 2 only as these modes are the strongest. These results show that the constant term a_o, or the amplitude of the infinite wavelength mode, becomes comparatively stronger as time increases. Hence the system is starting to run away, that is, it is getting hotter everywhere at an ever increasing rate and this effect is becoming increasingly dominant. As will be shown, a steady-state will never be achieved in such a system. This is also indicated by a plot of the value of $\frac{dE_I}{dt}$ as a function of time, figure (5.2h). This figure shows not only that $\frac{dE_I}{dt}$ is increasing in time, but $\frac{d^2E_I}{dt^2}$ is also.

The neglect of the y-component of the magnetic field appears to be directly responsible for allowing the infinite wavelength mode to grow. This is not strictly the case although this argument is upheld by once again looking at the results from linear theory. The dispersion relation obtained from the linear model where the y-component of the magnetic field is included and the inertial term is neglected is obtained by putting $\alpha_1 = 1$, $\alpha_2 = 0$ in equation (2.2.14) and dividing through by y. The growth rate of the infinite wavelength mode is then found by putting y = 0 (because $y = (\frac{2\pi}{\lambda})^2$) in the resulting equation. The non zero growth rate is given by

$$x = \frac{(5 - \frac{4}{\pi_e} - 9T) \pm [(5 - \frac{4}{\pi_e} - 9T)^2 - 4(\frac{5}{3} + T + \frac{2}{\pi_e})\ 18(1-T)^2]^{\frac{1}{2}}}{2(\frac{5}{3} + T + \frac{2}{\pi_e})} \qquad (5.1.8)$$

Again the radiation term has been neglected to obtain equation (5.1.8).

TABLE 5.1

Amplitudes of the Fourier modes as a function of time for the electron temperature profile

dimensionless time t	a_0	a_1	a_2	b_1	b_2
0	2.34×10^{-3}	8.68×10^{-3}	-2.02×10^{-2}	2.71×10^{-3}	-7.05×10^{-3}
0.5	1.44×10^{-3}	1.90×10^{-2}	-2.54×10^{-2}	6.14×10^{-3}	-9.95×10^{-3}
1.0	3.39×10^{-3}	3.22×10^{-2}	-2.69×10^{-2}	1.05×10^{-2}	-1.05×10^{-2}
1.5	7.42×10^{-3}	5.01×10^{-2}	-2.76×10^{-2}	1.67×10^{-2}	-1.07×10^{-2}
2.0	1.58×10^{-2}	7.62×10^{-2}	-2.79×10^{-2}	2.62×10^{-2}	-1.05×10^{-2}
2.5	3.36×10^{-2}	1.16×10^{-1}	-2.72×10^{-2}	4.13×10^{-2}	-9.38×10^{-3}
3.0	7.30×10^{-2}	1.82×10^{-1}	-2.43×10^{-2}	6.74×10^{-2}	-5.63×10^{-3}
3.5	1.65×10^{-1}	3.05×10^{-1}	-1.53×10^{-2}	1.18×10^{-1}	5.44×10^{-3}
4.0	4.07×10^{-1}	5.84×10^{-1}	1.22×10^{-2}	2.42×10^{-1}	4.18×10^{-2}
4.5	1.20	1.46	1.20×10^{-1}	6.64×10^{-1}	2.04×10^{-1}
5.0	6.33	7.28	9.66×10^{-1}	4.05	2.01
5.1	11.15	12.75	1.54	8.03	4.33
5.2	27.40	28.88	0.48	25.15	13.15
5.25	68.41	53.88	-16.34	80.80	30.16

x is negative for all values of T for which the instability condition is violated, and negative for $\pi_e << 1$ regardless of the value of T. We can say that the infinite wavelength mode is always damped in any situation of interest if the y-component of the magnetic field is included in the model. It is important to notice here that if the y component of the magnetic field is included the electric field E_z is no longer held constant. We compare this result with that from the dispersion relation for the model we are using where both the inertial term and the y-component of the magnetic field are ignored, $(\alpha_1=\alpha_2=0)$ equation (2.5.1). Putting y = 0 in this equation we find the dimensionless non zero growth rate x to be given by

$$x = 4 + 4\pi_e - 6T - 3\pi_e T(1+T) \qquad (5.1.9)$$

Assuming π_e to be negligibly small for the moment, we see that this infinite wavelength mode will grow provided,

$$T < \frac{2}{3} \quad \text{or} \quad \frac{T_{eo}}{T_i} > 1.5 \qquad (5.1.10)$$

We know the onset condition for the electrothermal instability to be

$$\frac{T_{eo}}{T_i} > 1.3187 \quad \text{without radiation} \qquad (5.1.11)$$

It appears that there exists a temperature range within which the electrothermal instability may be excited and the infinite wavelength mode damped, as we require. However, this is not so. Referring to the plots obtained, Figures 5.2, from the numerical model, it is only the electron temperature which has a growing constant term. This must be so because we conserve total mass and hence a uniform perturbation of the

density can never exist. Haines[10] showed that the condition for onset of the non-convective electrothermal instability is,

$$\frac{T_{eo}}{T_i} > 1.5 \qquad \text{if the density is unperturbed} \tag{5.1.12}$$

Therefore provided the plasma is unstable to electrothermal instabilities, this infinite wavelength mode will grow in our model.

In order to overcome this flaw in the model we must first understand physically why the inclusion of the y-component of the magnetic field prevents an increase in the average electron temperature, or conversely, why the neglect of it allows a "runaway" behaviour. Consider perturbing the steady-state electron temperature uniformly and leaving the other parameters, n and B_z, undisturbed. The electron energy equation (4.1.19) tells us that a uniform increase in the electron temperature alone grows, provided the electrothermal instability condition is violated, if the current is given by

$$j_z = \sigma E_z = T_e^{3/2} E_z \tag{5.1.13}$$

and E_z is held at its steady-state value. In which case we have,

$$\frac{dT_e}{dt} = \frac{2}{3} A_F^2 T_e^{3/2} - \frac{2(T_e - T_i)}{T_e^{3/2}} \tag{5.1.14}$$

Furthermore, not only will T_e continue to increase, but the rate at which it increases will increase as T_e gets larger. Hence the system runs away. This behaviour is a direct result of allowing the current density j_z, and hence $\underline{j}.\underline{E}$, to increase everywhere without limit. In reality, an increase in j_z produces an increase in the curl of B_y (Ampère's Law). That is, some of the energy available goes into

magnetic energy. This change in time in B_y produces a curl E_z (Faraday's Law) which acts in such a way as to oppose the increasing current. We have effectively allowed the current density to increase without limit by not allowing the electric field E_z to change. Hence the fundamental reason for the runaway behaviour is the constant electric field condition. The system runs away if the electric field is held constant whether or not the y-component of the magnetic field is included. In the two models compared it is whether or not the electric field is allowed to vary rather than the inclusion or neglect of B_y which determines the behaviour of the infinite wavelength mode. In the next section we formulate a model which prevents this unrealistic runaway behaviour.

5.2 CONSTANT TOTAL CURRENT CONSTRAINT

In this section we change the model to overcome the unrealistic runaway behaviour of the system produced by allowing the current density to increase without limit because E_z is held constant in time. We impose the condition that the total current in the $\hat{z}$ direction be conserved. This is fortunately a more realistic model because it is found experimentally that the total current in the discharge remains approximately constant in time. Therefore we choose to vary the electric field E_z such that total current is conserved, that is

$$\int_0^{\lambda_m} j_z \, dx = \lambda_m \qquad \text{for all time} \tag{5.2.1}$$

because j_z is equal to one everywhere before the perturbation is applied, so that,

$$E_z(t) = \frac{\lambda_m}{\int \sigma \, dx} \tag{5.2.2}$$

where Ohm's Law, equation (4.1.18), has been used. Limiting the length of the mesh to λ_m should mean that, for the wavelengths we are able to represent with this model, the amount of energy going into the magnetic field, which we have ignored, is negligibly small. This assumption can be tested for each run.

A random perturbation is again applied to the system in the same manner as described in the last section. That is, such that total mass is conserved equation (5.1.1) and the quantity E_I is not a function of j. Equation (5.2.2) is then used in discrete form to find the value of the applied electric field E_z,

$$E_z^n = \frac{\lambda_m}{\sum_{j=1}^{J-1} (T_{ej}^{n\ 3/2} + T_{ej+1}^{n\ 3/2}) \frac{\Delta x}{2}} \qquad (5.2.3)$$

at every time level n. Inner iterations are performed at later time steps as successively improved approximations for T_e at time levels n+1 are found. This ensures that the value of E_z obtained is self-consistent.

Again many runs were performed for each set of results presented here to check that the effects observed are physical and not produced by numerical errors. We compared the results from runs with different initial amplitudes of perturbation with the same time step and space step. In every case the results exhibited the same behaviour. The space step Δx and the time step Δt were also changed and the results consistently compared. In all of these tests the results did not appreciably deviate from those presented here.

5.3 THE MESH LENGTH EQUAL TO THE CUTOFF WAVELENGTH

The initial steady-state to be perturbed is completely described

by giving the values of the temperature ratio $\frac{T_i}{T_{eo}}$, π_e and $\omega_o\tau_o$, if Bremsstrahlung radiation is neglected. If Bremsstrahlung is included we have to specify the electron temperature. For this reason and because Bremsstrahlung has a very small effect except at high temperatures, we neglect radiation loss. Choosing,

$$\begin{aligned} \omega_o\tau_o &= 6.14 \times 10^{6} \\ \pi_e &= 4.338 \times 10^{-3} \\ T_i/T_{eo} &= 0.5 \end{aligned} \tag{5.3.1}$$

we can calculate the linear dimensionless growth rate x for any value of the square of the dimensionless wavenumber y, using the dispersion relation equation (2.2.14). Using equation (2.2.14) and the condition for the effect of the inclusion of the y-component of the magnetic field to have negligible effect upon the growth of the electrothermal instability, relation (2.4.5), it is a simple matter to find the dimensionless wavelength λ_m above which our model breaks down.

$$\text{If} \qquad \lambda_m = 20 \tag{5.3.2}$$

which is the optimum wavelength for growth, we find the left hand side of (2.4.5) has the value,

$$\frac{\pi_e x}{2y} = \frac{\pi_e x \lambda_m^2}{2(2\pi)^2} \simeq 2 \times 10^{-2} \tag{5.3.3}$$

Hence we consider the value of λ_m given in (5.3.2) to be the largest wavelength that can be represented using this model, with this particular set of initial conditions. The mesh length was set equal to λ_m and the following results were obtained.

The plots in Figure 5.3 depict the evolution of the initial random perturbation. As can be seen from these figures, the longest wavelength the space mesh can represent eventually dominates. This result is expected because linear theory tells us that this mode has the largest linear growth rate. The electron temperature profile develops a large single filament (Figure 5.3a). At t = 12 scale times, this hot filament has a half-width equal to about 0.13 λ_m. The electron temperature troughs are very flat. The maximum electron temperature is about 16 times the initial electron temperature, while the temperature in the trough is very nearly equal to the ion temperature. This minimum temperature in the trough is reached quite quickly. After t = 5 scale times the temperature in this region is virtually constant. This can be understood by looking at the current density profiles and the electron energy equation (4.1.6). Figures (5.3c) and (5.3d) tell us that after t = 5 scale times there is about one tenth of the initial current in the electron temperature trough. All derivatives of the electron temperature here are very nearly zero and the electron and ion temperatures are very nearly equal. Hence the small rate of change of the electron temperature here is due to the fact that all the terms are small in equation (4.1.6). The density in this region, however, is still changing considerably (Figure (5.3b)). The large scale structure ofthe number density shows there is a density minimum at the temperature maximum and vice versa. Again this result was expected from linear theory. However, there is a secondary density peak located at the density minimum which quickly develops, and continues to grow. The secondary peak is a result of the plasma not leaving this region as quickly as that either side of it, and it does not mean the density is increasing here. This phenomenon may be explained by looking at the current density profiles, Figures (5.3c) and (5.3d). We observe that the current density in the $\hat{y}$-

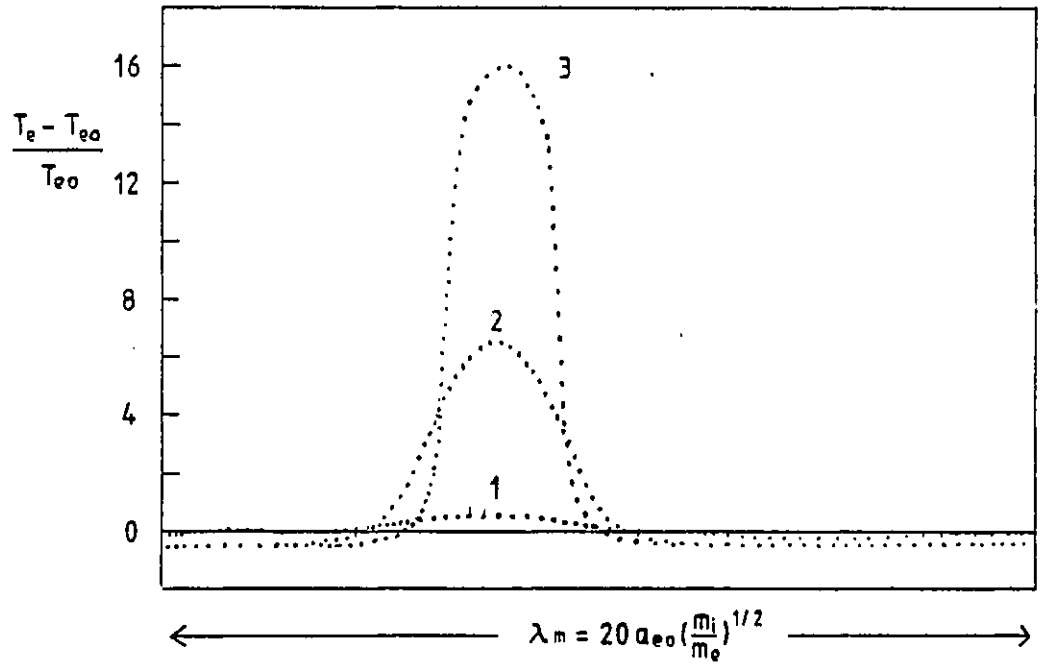

Figure 5.3a Electron temperature profiles at dimensionless times 1) t = 1; 2) t = 5; 3) t = 12.

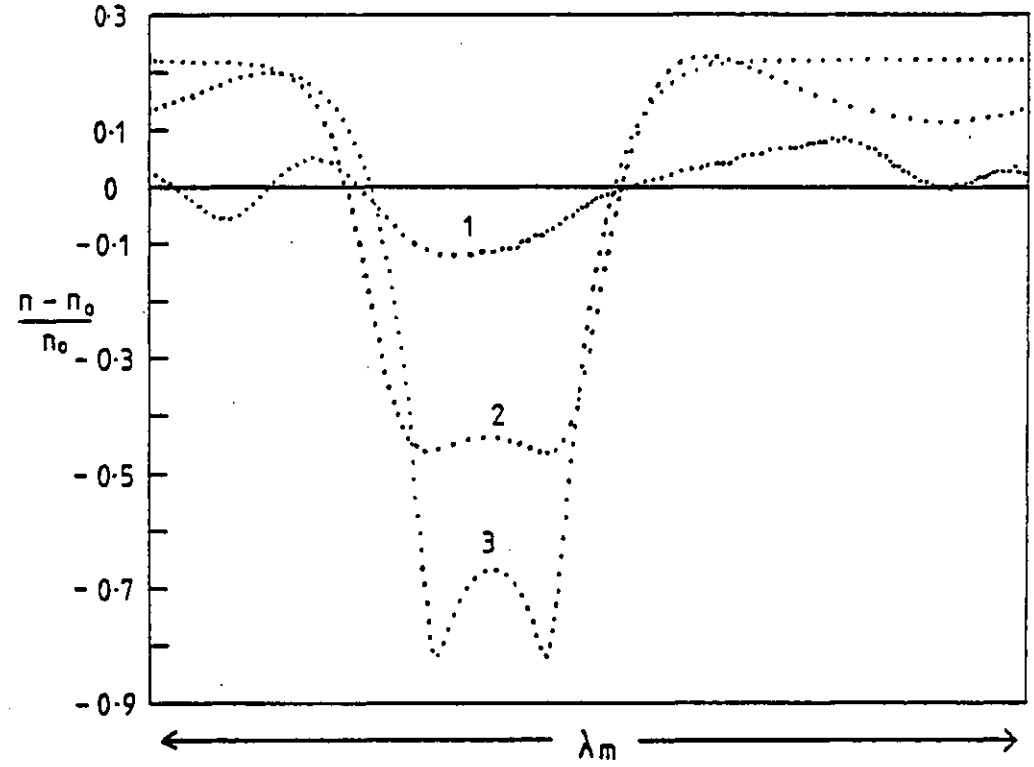

Figure 5.3b Number density profiles at 1) t = 1; 2) t = 5; 3) t = 12.

Figures 5.3

Results obtained when the mesh length is set equal to the cutoff wavelength

$\omega_o \tau_o = 6.14 \times 10^6$, $\pi_e = 4.338 \times 10^{-3}$, $T_i/T_{eo} = 0.5$, R = 0

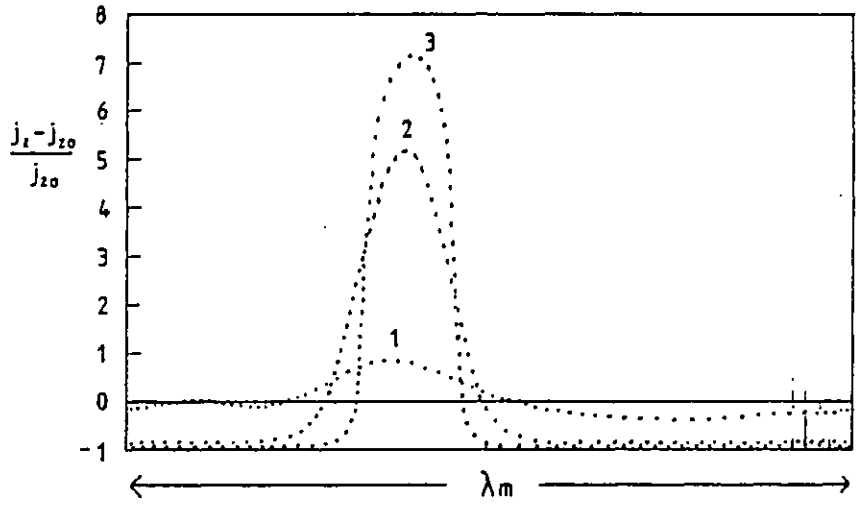

Figure 5.3c z-component of current density at 1) t=1, 2) t=5, 3) t=12.

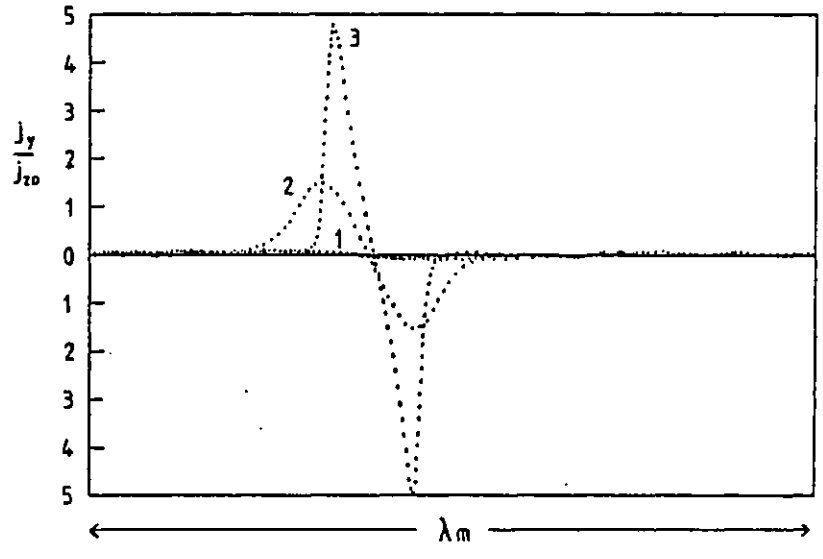

Figure 5.3d y-component of current density at 1) t=1, 2) t=5, 3) t=12.

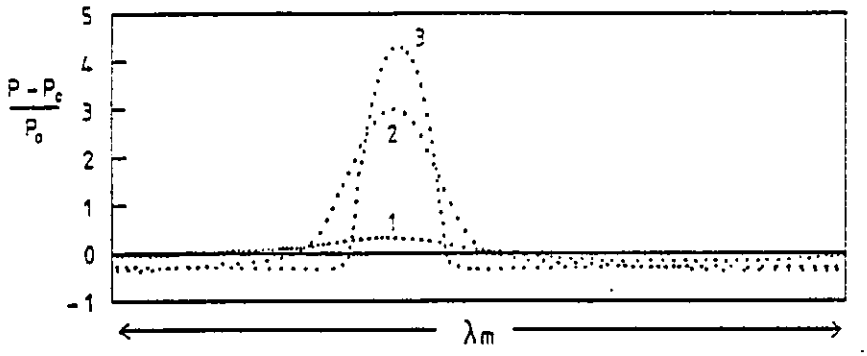

Figure 5.3e Spatial variation of total pressure at 1) t=1, 2) t=5, 3) t=12.

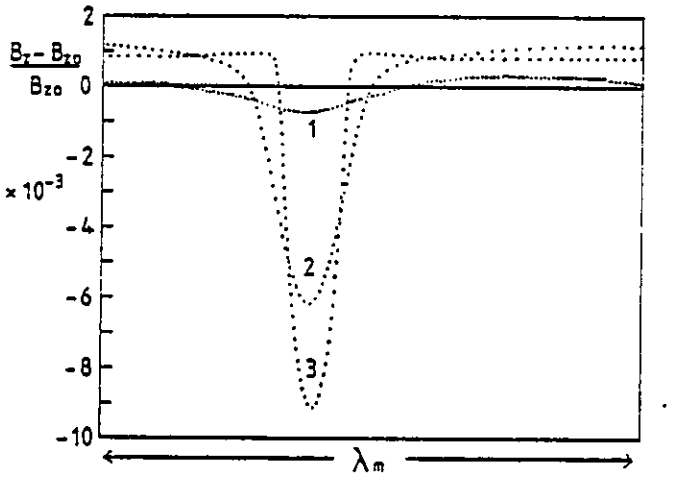

Figure 5.3f z-component of the magnetic field at 1) t=1, 2) t=5, 3) t=12.

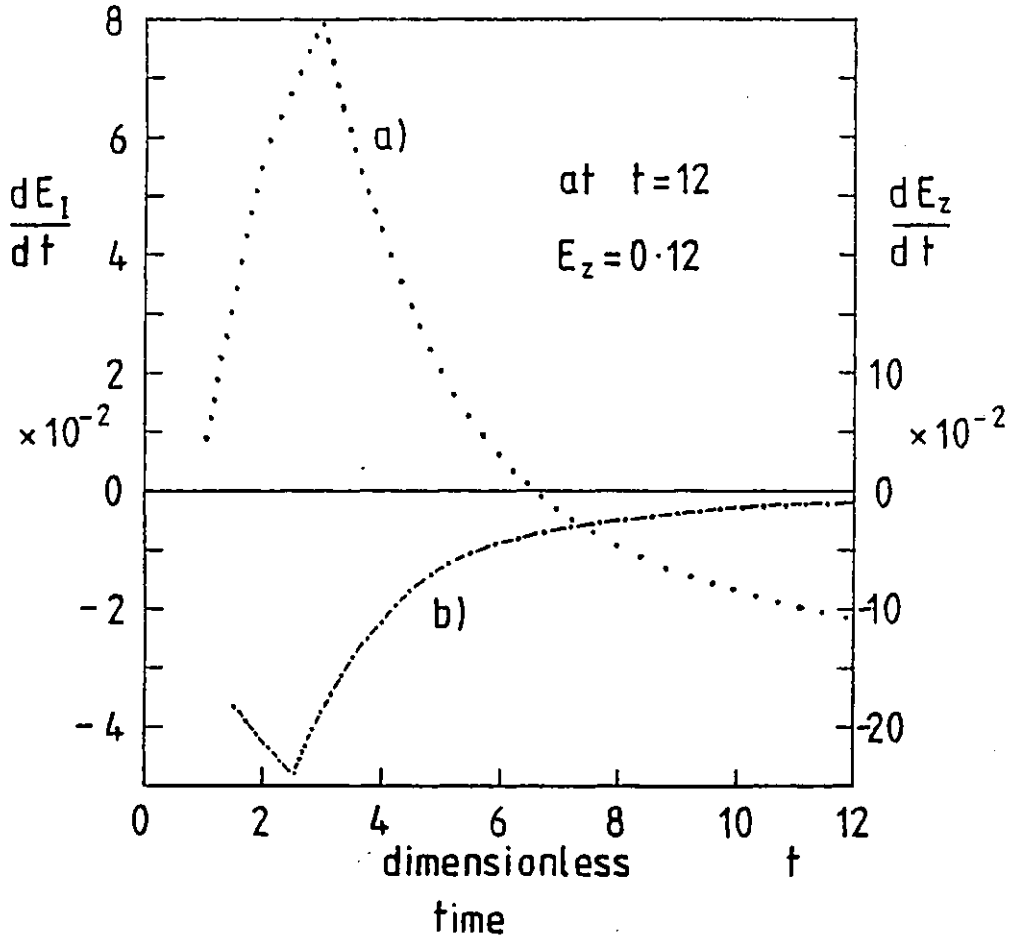

Figure 5.3g In Figure 5.3g the curve labelled a) shows the variation in time of the rate of change of the internal energy and the curve labelled b) shows the variation in time of the rate of change of the applied electric field required to maintain constant total current.

direction, in the early stages ($t \lesssim 1$), is much less than the current density in the $\hat{z}$-direction; the initial current density in the $\hat{y}$-direction is equal to zero. As the instability develops the y-component of the current density becomes increasingly important. After time t = 5 scale times the magnitude of the peak value of the y-component is of the same order as that of the z-component. Furthermore the maxima of $|j_y|$ occur either side of the maximum value of j_z. As the Ohmic heating rate goes as $\frac{(j_y^2+j_z^2)}{\sigma}$, the monotonic decrease of the heating rate away from the j_z peak no longer occurs as it did at previous times when $|j_y| << |j_z|$. Hence an extra heating at the "flanks" of the electron temperature filament occurs, leading to a spiky structure with wider spikes than expected from the results presented in Chapter 3. It is worth noting here that the perturbation in the magnetic field, B_z, is always comparatively small; its maximum value being about 9×10^{-3} B_{zo} at the end of the run (Figure 5.3e).

In Figure (5.3g) we plot the values of the rate of change of the dimensionless electric field and the rate of change of the dimensionless internal energy E_I against dimensionless time. The purpose of these plots is to indicate whether the system is approaching a steady-state. In this case clearly it is not. They also tell us that the applied electric field is decreasing in time throughout the simulation.

In summary we can say that the instability develops in such a way as to produce current filamentation. The electron temperature in the filaments is much higher than that of the surrounding plasma while the number density is much lower. The filaments are narrow and spiky with a separation distance equal to the wavelength of the fastest growing mode. In the regions surrounding the filaments the profiles for the number density, current density, electron temperature and magnetic field become very flat. The electron temperature is very nearly equal to the ion temperature and the current density is only

about 10% of its equilibrium value. The amplitude of the filament grows in time and becomes narrower. The filament has grown to a large amplitude after twelve linear growth times and the system is not approaching a steady-state. The electric field is decreasing throughout the simulation in order to keep the total current constant. Results found at times later than t = 12 scale times show that the filament continues to grow and becomes narrower and the electric field tends to zero. A steady state is not found and the system continues to behave in the way already described. The results at later times do not add to our information on how the system evolves and are therefore not reproduced here.

There are two further reasons why we do not show results at times later than t = 12 scale times. The first reason is that a fluid model of the system becomes invalid shortly after this time. As stated in Chapter 1, the fluid approach is only valid for large $\omega_e \tau_e$ if,

$$L_\perp \gg a_e \tag{5.3.4}$$

where $L_\perp$ is the characteristic scale length over which the plasma quantities vary perpendicular to the magnetic field and a_e is the electron Larmor radius. If condition (5.3.4) is not satisfied, the transport coefficients in the form used here are no longer valid. The characteristic dimensionless length scale over which the electron temperature varies may be approximated by,

$$\frac{L_\perp}{L_o} = \left(\frac{1}{T_e}\frac{\partial T_e}{\partial x}\right)^{-1} \tag{5.3.5}$$

We arbitrarily stipulate that the quantity in (5.3.5) should always be greater than about ten times the dimensionless electron Larmor radius.

Shortly after t = 12 scale times this condition is violated and hence our model is no longer applicable.

Before the fluid model breaks down, the condition for onset of ion acoustic instability (as given in equation (3.4.4) of Chapter 3) is violated in parts of the current filament. The presence of ion acoustic instability would have an important effect on the further evolution of the filament, because it is known[31,32] to lead to a high effective electron-ion collision frequency when fully developed. In Chapter 6 we simulate the macroscopic effects of ion acoustic turbulence on the further evolution of the system. In the rest of this chapter we explore the changes in the behaviour of the electrothermal instability brought about by using a smaller mesh length and hence reducing further the longest wavelength represented.

5.4 MESH LENGTH LIMITED TO SIX SCALE LENGTHS

A perturbation was applied to the steady-state system in exactly the same manner as described in the last section. The same initial conditions were used and the only change made was that the length of the mesh was set equal to six scale lengths instead of twenty.

Figure (5.4a) shows the electron temperature profile at different times during the simulation. We notice again that the longest wavelength on the mesh quickly dominates which is acceptable because linear theory tells us that the linear growth rate of growing modes increases as the wavelength is increased up to the optimum wavelength for growth. The shape of the electron temperature profile is smoother throughout the simulation than it was in the results in the last section; the temperature peaks are not as sharp nor the troughs as flat. The density profile (Figure 5.4b) has the shape one

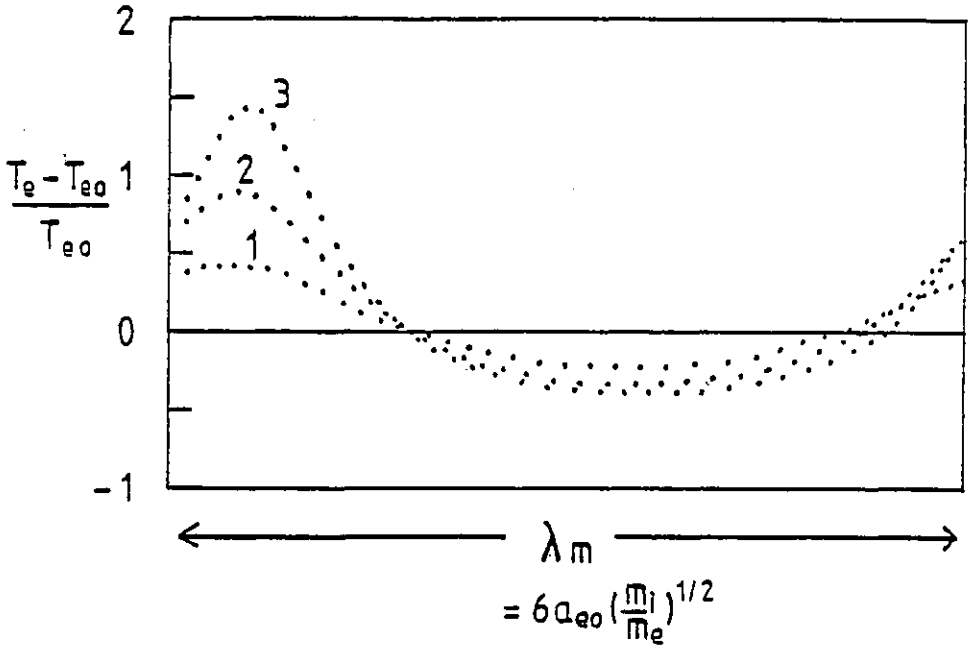

Figure 5.4a Spatial variation of electron temperature at times 1) t = 17; 2) t = 21; 3) t = 35.

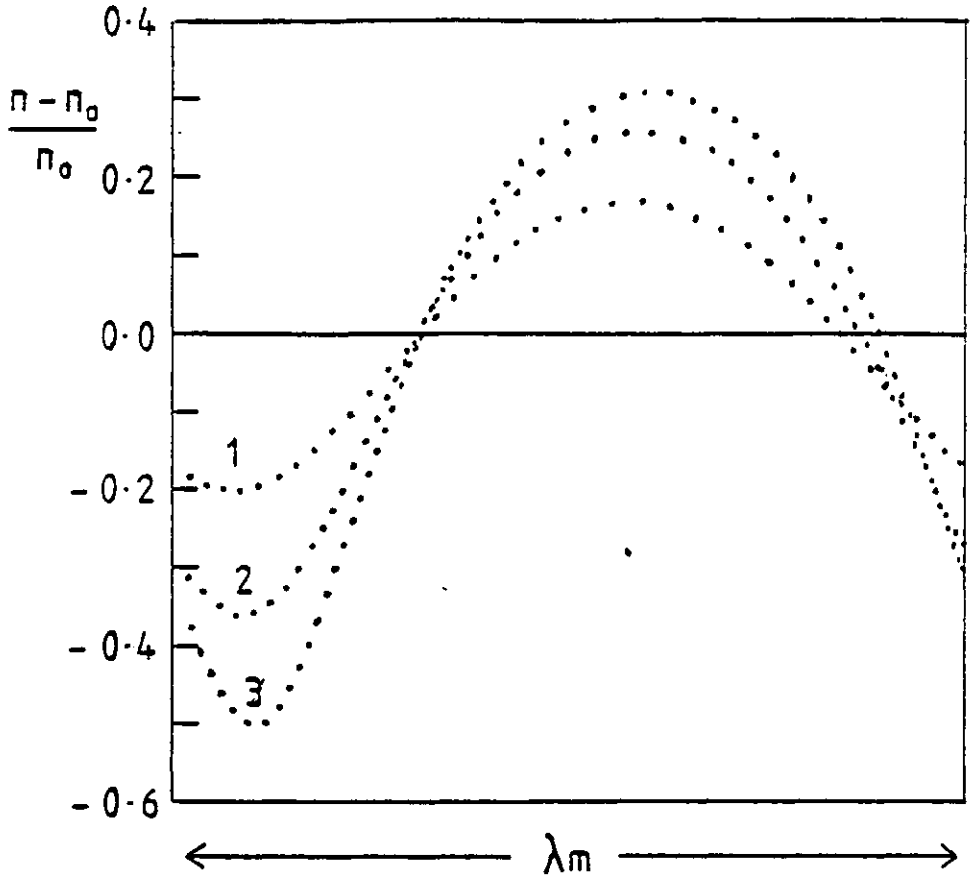

Figure 5.4b Number density profiles at 1) t = 17; 2) t = 21; and 3) t = 35.

Figures 5.4

The mesh length set equal to six scale lengths

$\omega_o\tau_o = 6.14\text{x}10^{6}$, $\pi_e = 4.338\text{x}10^{-3}$, $T_i/T_{eo} = 0.5$, R = 0

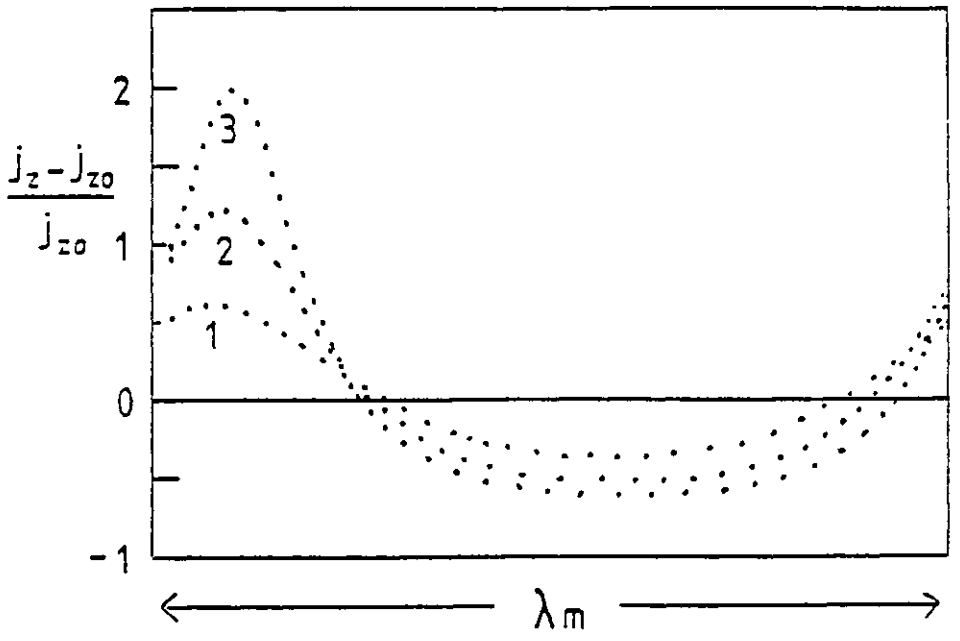

Figure 5.4c z-component of current density profiles at 1) t = 17; 2) t = 21 and 3) t = 35.

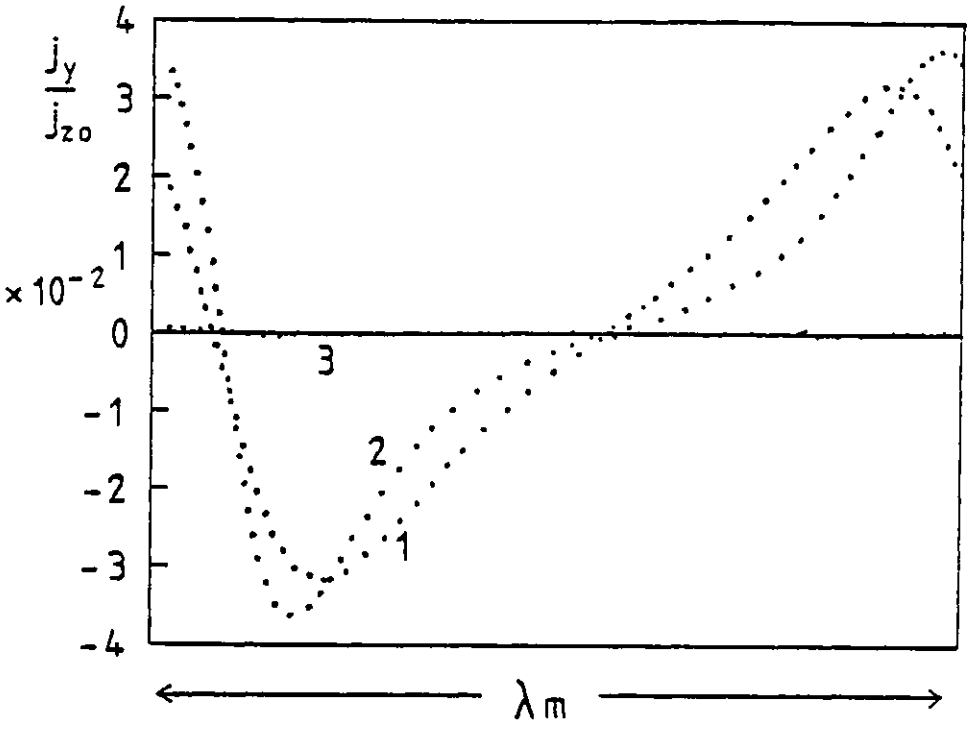

Figure 5.4d y-component of current density at 1) t = 17; 2) t = 21 and 3) t = 35. The y-component of the current density returns to zero when a steady-state is reached after t = 35.

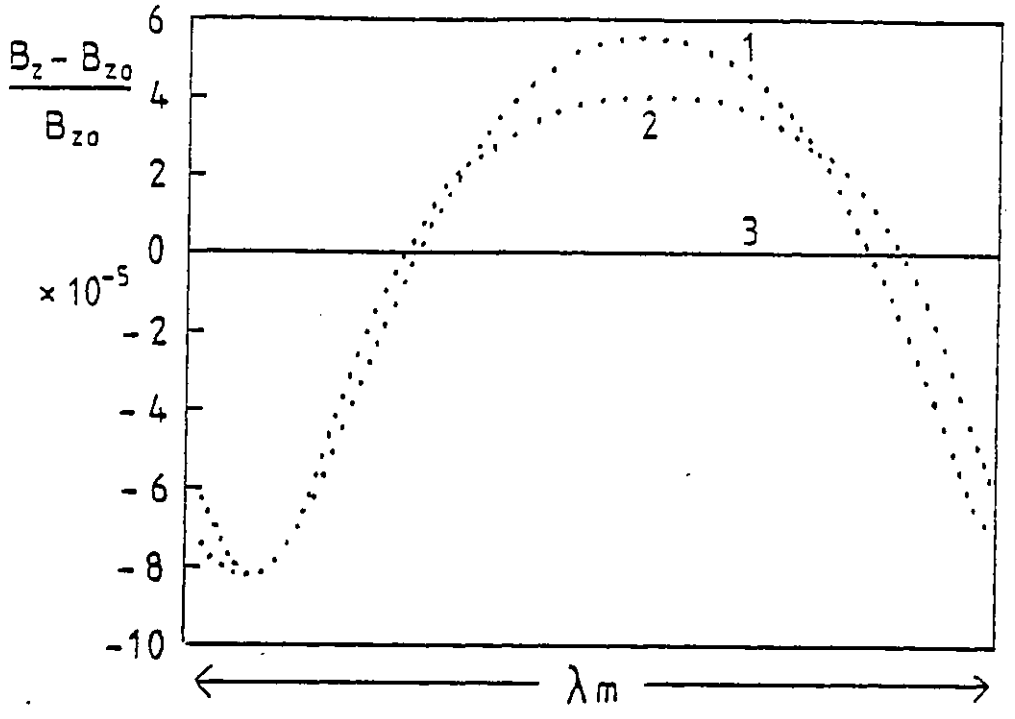

Figure 5.4e Spatial variation of magnetic field at 1) t = 17, 2) t = 21 and 3) t = 35.

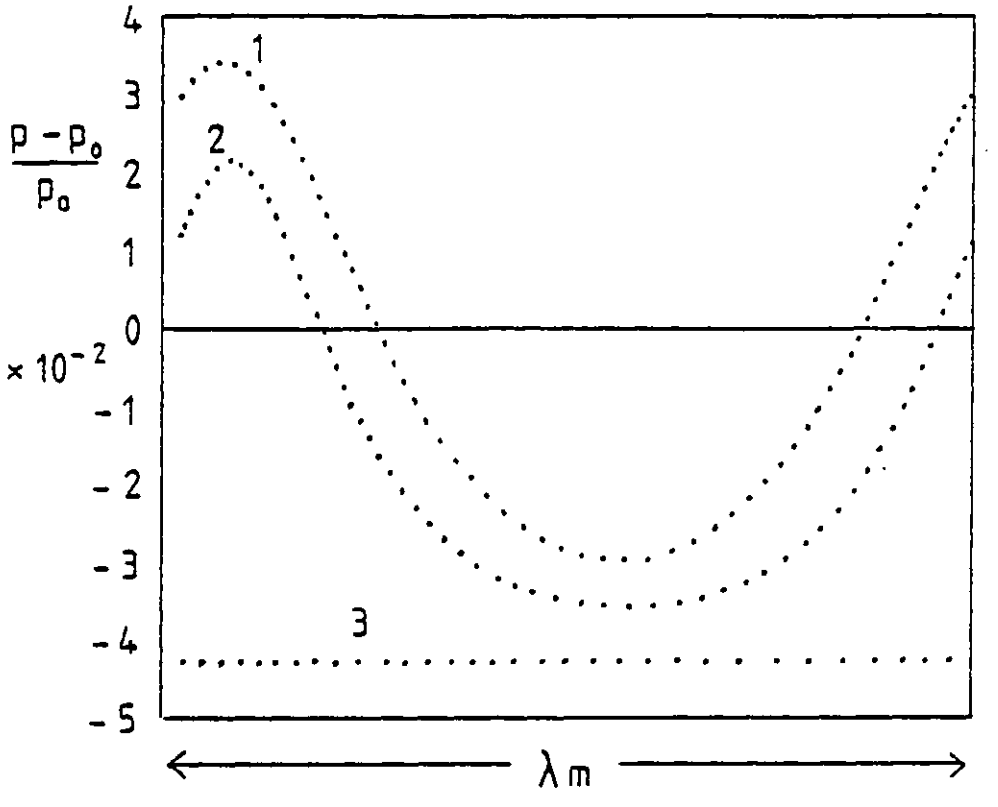

Figure 5.4f Total pressure profiles at 1) t = 17, 2) t = 21 and 3) t = 35.
When a steady-state is reached after time t = 35 the magnetic field returns to its initial configuration and the final total pressure is uniform again.

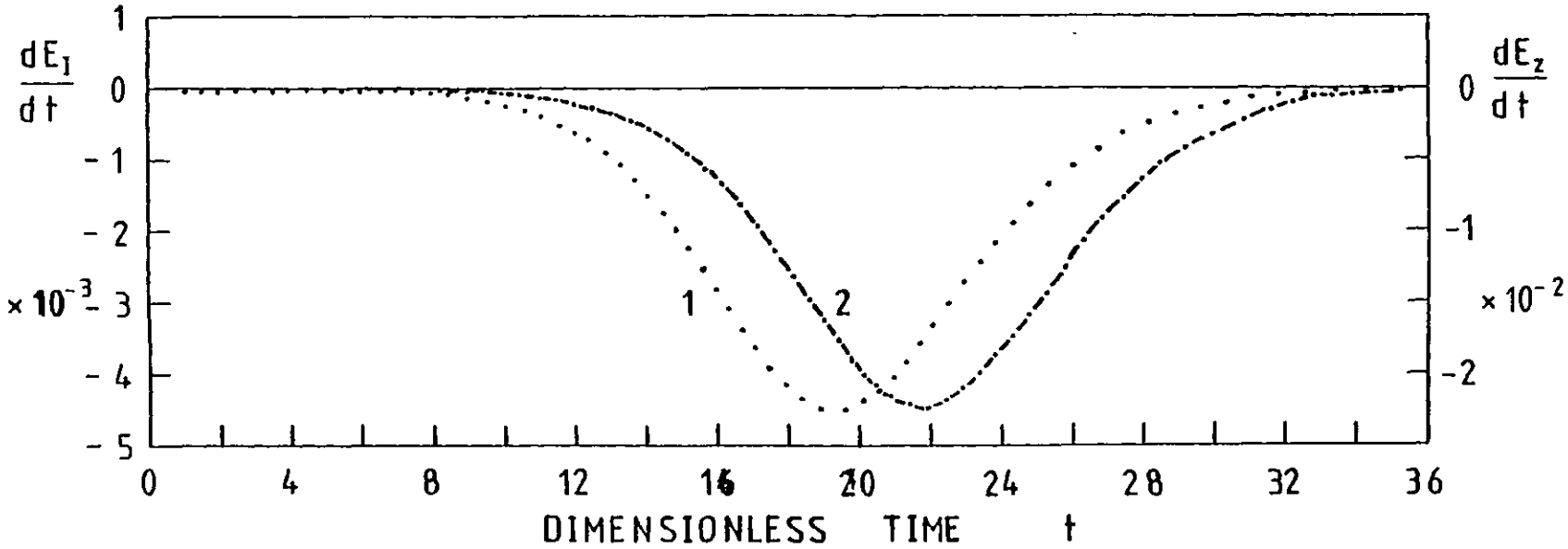

Figure 5.4g The curve labelled 1) shows the variation in time of the rate of change of the applied electric field and 2) shows the variation in time of the rate of change of the internal energy. Both go to zero at t = 35. The final steady-state value of the electric field is $E_z = 0.7855\ E_{zo}$.

would expect from looking at the electron temperature profiles. Looking at the current density profiles, Figure (5.3c) and Figure (5.3d) it is evident that the y-component of the current is always much smaller than the z-component, and again both are more smoothly varying than in the last set of results.

The most important result here is that a steady-state is reached. After the time labelled t = 35 scale times the electron temperature, z-component of the current density and the number density remained constant, while the y-component of the current density returned to zero and the magnetic field configuration returned to its initial value. The final total pressure is lower than its initial value. Figure (5.4g) shows the temporal behaviour of the quantities $\frac{dE_I}{dt}$ and $\frac{dE_z}{dt}$ both of which are very close to zero at t = 35 scale times. Furthermore the steady-state reached must be a stable one as the run was continued beyond this point in time with no further change. If the steady-state were not stable round-off error would be enough to trigger further changes.

Comparison with results in Chapter 3

The steady-state maximum value of the electron temperature is,

$$T_{emax} = 2.433 \text{ in dimensionless units} \qquad (5.4.1)$$

or in units of degrees Kelvin,

$$T_{emax} = 2.433\ T_{eo}\ ^{\circ}K \qquad (5.4.2)$$

where T_{eo} is the initial steady-state electron temperature in degrees Kelvin before the perturbation was applied. The minimum electron

temperature attained is,

$$T_{emin} = 1 - 0.3844 \quad \text{in dimensionless units} \tag{5.4.3}$$

or in units of degrees Kelvin,

$$T_{emin} = 0.6116\ T_{eo}\ ^{\circ}K \tag{5.4.4}$$

In Chapter 3 we obtained solutions to the steady-state electron energy equation. For the results presented in this section to be believable the electron temperature profiles must satisfy equation (3.1.9) with B = 0 (no radiation loss). This must be so because every assumption that was made to obtain solutions of the electron energy equation in Chapter 3 hold for these steady-state solutions, i.e.

$$\begin{aligned} &\omega_e \tau_e >> 1 \\ &\underline{E},\ \underline{B} \text{ and } T_i \text{ uniform} \\ &\nabla p = 0 \\ &\underline{j} \parallel \underline{B} \text{ everywhere} \end{aligned} \tag{5.4.5}$$

A_H^2 (not to be confused with A_F^2) is defined as given in equation (3.1.5), that is,

$$A_H^2 = \frac{m_i k_B \alpha^{12} T_i^4 E_z^2}{p^2 e^2} \tag{5.4.6}$$

(dimensionless quantities have not been used in equation (5.4.6)). A_H^2 can be written in terms of A_F^2 defined in equation (4.1.12) (and in equation (4.8.1)) as follows :

$$A_H^2 = A_F^2 \frac{E_z^2}{p^2} T_i^4 \qquad (5.4.7)$$

where the dimensionless quantities T_i, E_z and p are defined in (4.1.11). We can calculate A_H^2 for the steady-state solutions in this section. From the results and equation (4.8.1) for A_F^2 and the initial conditions,

$$\left.\begin{aligned} A_F^2 &= 1.5 \\ E_z^2 &= 0.7855^2 \\ p^2 &= (1.5 - 4.28 \times 10^{-2})^2 \\ T_i^4 &= 0.5^4 \end{aligned}\right\} \text{ final values} \qquad (5.4.8)$$

Hence,

$$A_H^2 = 2.7241 \times 10^{-2} \qquad (5.4.9)$$

We now briefly recall the method used in Chapter 3 to solve for the steady state electron temperature profile using the electron energy equation. For a given value of A_H^2 we choose "t_{min}" (remembering "t_{min}" = T_{emin}/T_i). With this value of t_{min} we can find the constant of integration. Using this value of the constant of integration we can find t_{max} ($t_{max} = T_{emax}/T_i$). For a clearer account of this method we refer the reader to section 3.2 of Chapter 3.

From the results in this section we know A_H^2, t_{min} and t_{max}. We now use these known values of A_H^2 and t_{min} and use the method described in Chapter 3, section 2 to find t_{max}. Obviously the value of t_{max} calculated in this way must agree with the value which can be derived from (5.4.2). Also, the wavelength calculated using the numerical method in Chapter 3 must equal the length of the mesh. The

results are compared in Table 5.4

TABLE 5.4

$A_H^2 = 2.7241 \times 10^{-2}$, $t_{min} = 1.2232$, no radiation loss

$t_{max} = \frac{T_{emax}}{T_i}$ λ in units of $a_{eo}(\frac{m_i}{m_e})^{\frac{1}{2}}$

value calculated using method in Chapter 3	4.882	5.89
value obtained from present model	4.866	6

The good agreement between the results obtained from the non-linear steady-state model and the steady-state results obtained here as a result of following the evolution of the electrothermal instability until saturation gives confidence in the computer program.

We note that the condition for onset of ion acoustic turbulence (5.3.7) is never violated in the electron temperature and current peaks.

5.5 MESH LENGTH SET TO SEVEN SCALE LENGTHS

The results obtained when the mesh length is limited to seven scale lengths are portrayed in Figures (5.5). The system again evolved to a stable steady-state. That is the results shown did not change appreciably after time t = 18.5. The arrival at a steady-state is also indicated by $\frac{dE_I}{dt}$ and $\frac{dE_Z}{dt}$ tending to zero at this time (Figure 5.5h). We have also plotted $\frac{dT_{emax}}{dt}$ as a function of time which also tends to zero, as it should. The final value of the electric field is somewhat lower than that obtained when the mesh length was limited to six scale lengths,

Figure 5.5a Spatial variation of electron temperature profile at 1) t=4, 2) t=7, 3) t=8 and 4) t=18.5. Steady-state exists after time t=18.5.

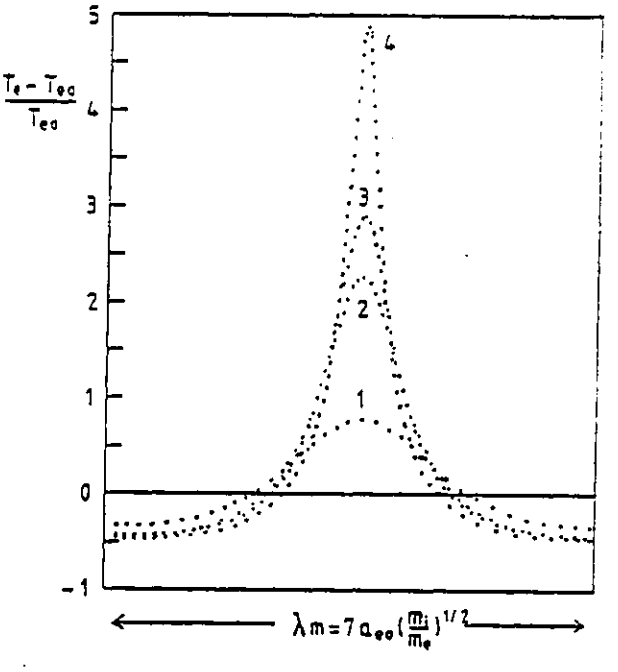

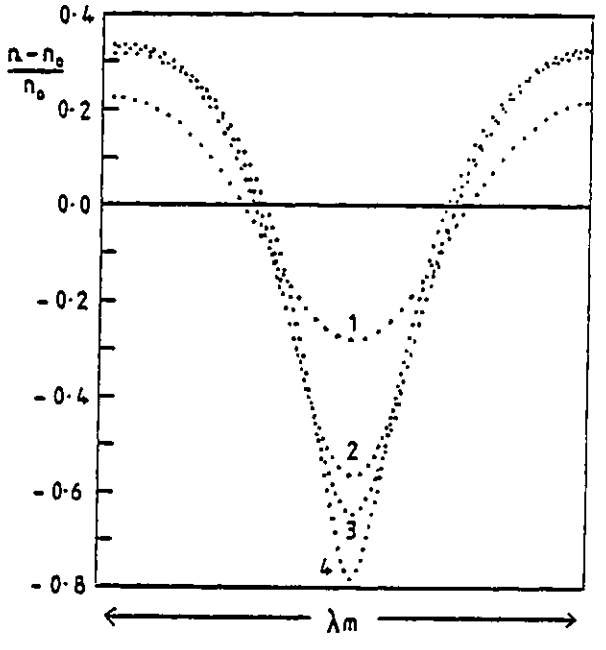

Figure 5.5b Number density profiles at 1) t=4, 2) t=7, 3) t=8 and 4) t=18.5

Figures 5.5

Mesh length set equal to seven scale lengths

$\omega_o \tau_o = 6.14 \times 10^6$, $\pi_e = 4.338 \times 10^{-3}$, R = 0, $T_i/T_{eo} = 0.5$

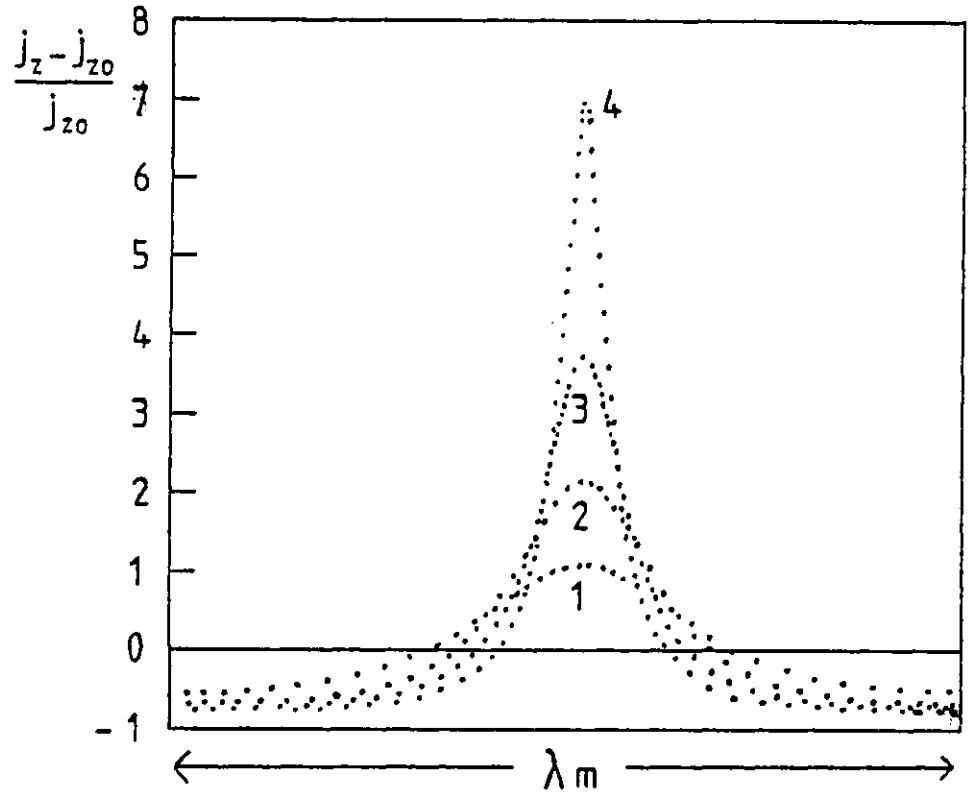

Figure 5.5c z-component of current density at 1) t = 4, 2) t = 7, 3) t = 8, 4) t = 18.5.

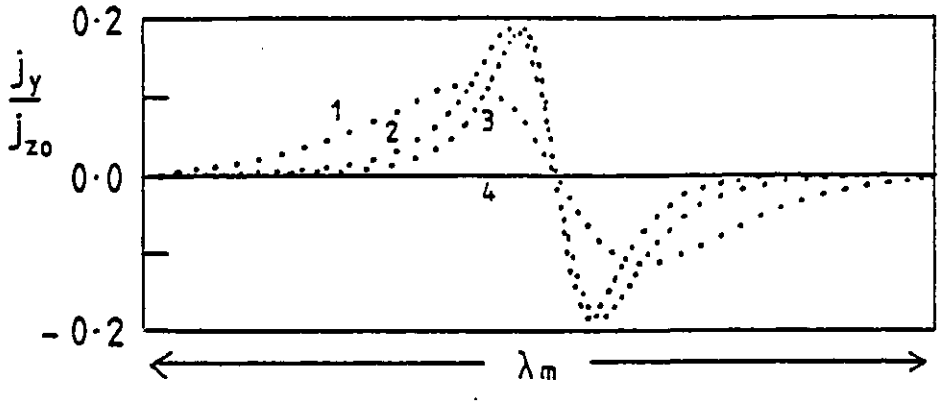

Figure 5.5d y-component of current density at 1) t = 4, 2) t = 7, 3) t = 8, 4) t = 18.5.

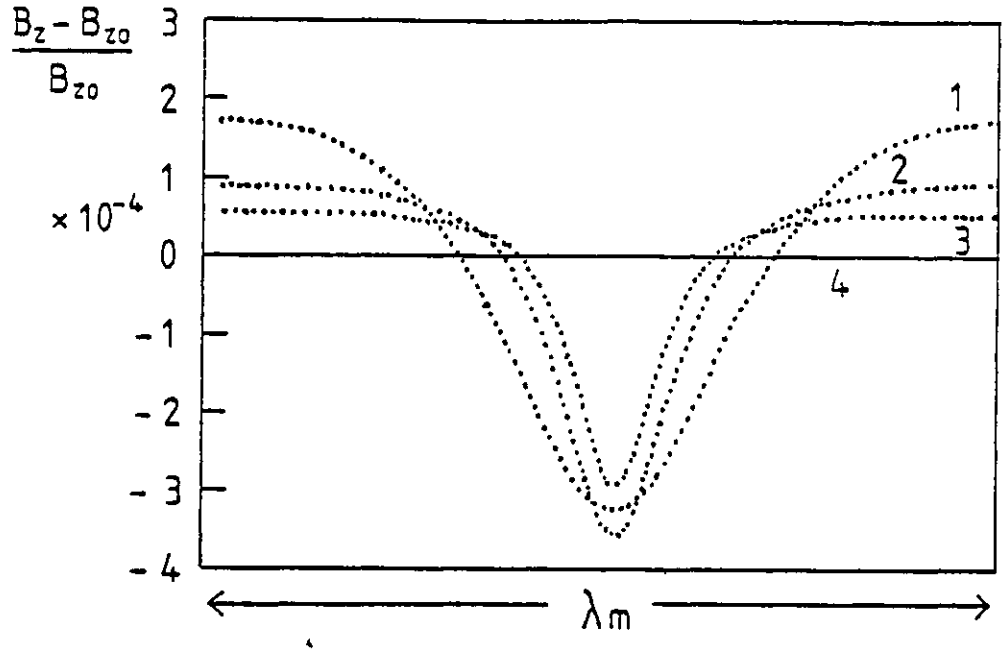

Figure 5.5e z-component of the magnetic field at 1) t = 4, 2) t = 7, 3) t = 8, 4) t = 18.5

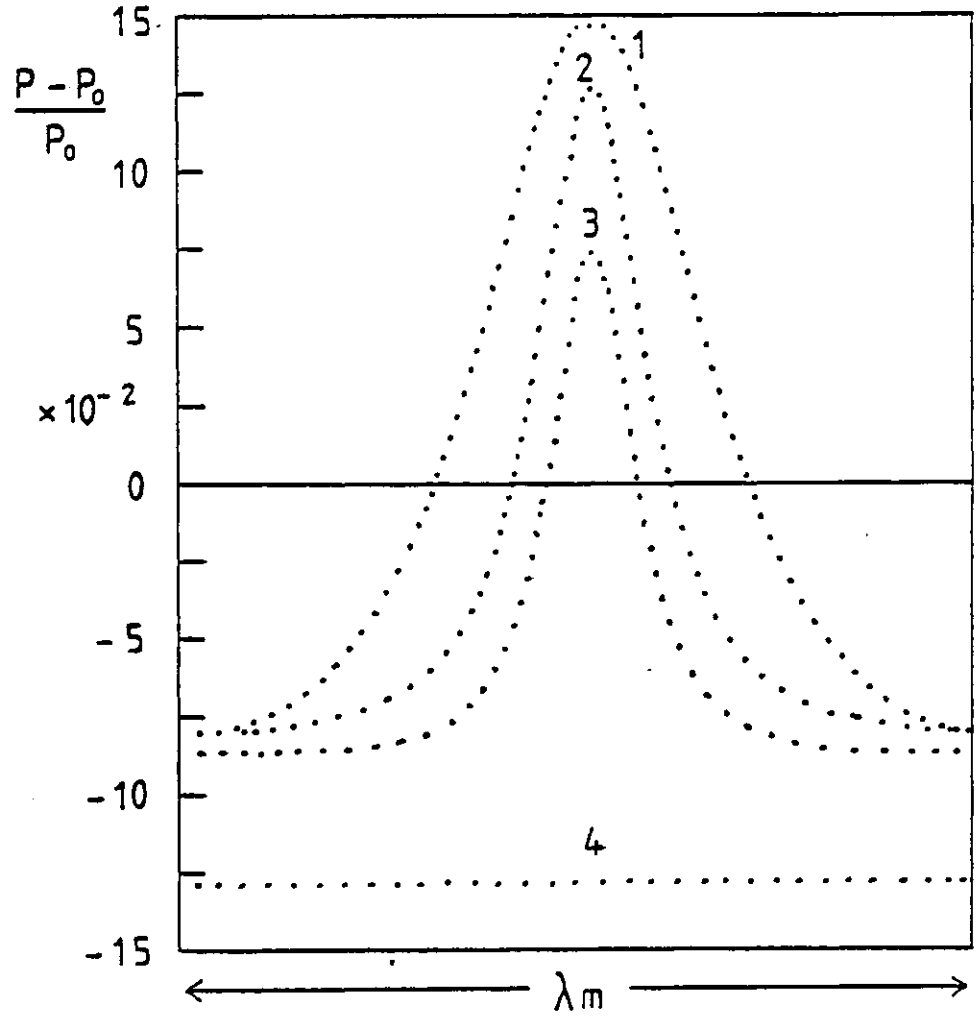

Figure 5.5f Total pressure profiles at 1) t = 4, 2) t = 7, 3) t = 8, 4) t = 18.5.

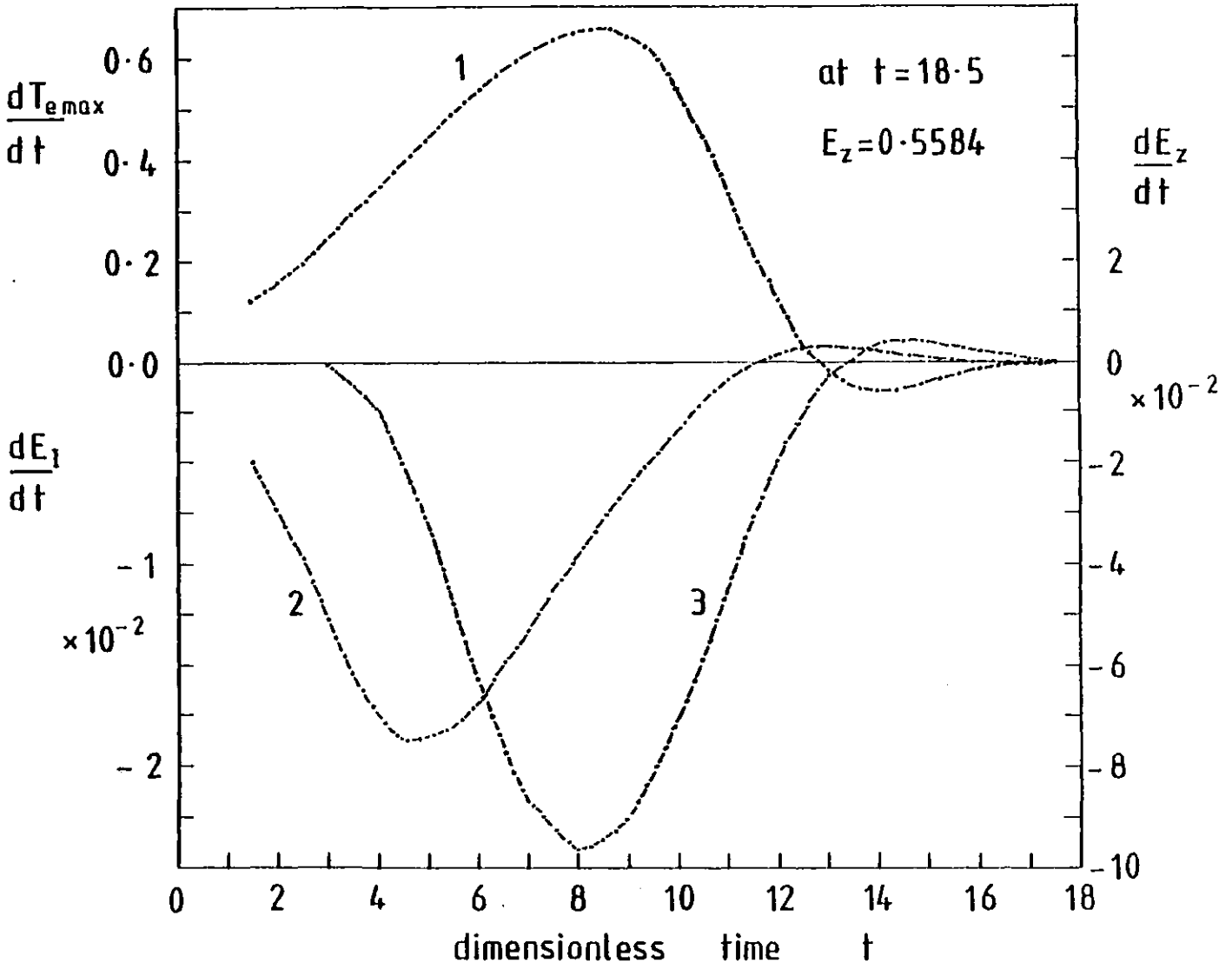

Figure 5.5g The curve labelled 1) shows the variation in time of the rate of change of the maximum electron temperature. 2) shows the variation in time of the rate of change of the internal energy and 3) shows the variation in time of the rate of change of the electric field.

steady-state value E_z = 0.5584 (5.5.1)

Correspondingly the final total pressure which is uniform has a lower value as can be seen by comparing figures (5.4f) and (5.5f). The electron temperature profile is more sharply peaked with a higher maximum value and the electron temperature trough is flatter with a lower minimum value. The y-component of the current density is at all times much smaller than the z-component.

It can be easily verified that the condition for onset of ion acoustic instability is just violated in the electron temperature peak. The characteristic scale length at the steepest point of the electron temperature profile is such that it is still valid to consider the plasma a fluid.

Comparison with results in Chapter 3

The steady-state electron temperature profile from these results is compared with the steady-state solutions found using the method in Chapter 3 in the same way as described in the last section. Good agreement was again found as can be seen from Table 5.5.

Final value of E_z = 0.5584

Final value of p = 1.5 - 0.1283

Hence from (5.4.7)

$$A_H^2 = 1.5536 \times 10^{-2}$$

Notice that this value of A_H^2 is less than the value obtained for the steady-state with the mesh length limited to six scale lengths.

TABLE 5.5

$A_H^2 = 1.5536 \times 10^{-2}$, $t_{min} = 1.0805$, no radiation loss

	t_{max}	λ in units of $a_{eo}(\frac{m_i}{m_e})^{\frac{1}{2}}$
Value calculated using method in Chapter 3	11.5544	6.5
Value obtained from present model	11.7842	7

5.6 MESH LENGTH SET TO EIGHT SCALE LENGTHS

The results obtained when the mesh length was limited to eight scale lengths are shown in Figure (5.6). The simulation was terminated after time t=8 because the characteristic scale length of the electron temperature gradient at its steepest point is just greater than ten electron Larmor radii. Hence a fluid approximation is no longer valid by our criterion after time t=8 scale times. Furthermore the condition for ion acoustic instability to be present is well violated by this time. As previously stated, the macroscopic effects of ion acoustic turbulence would have a considerable effect on the evolution of the plasma parameters after the condition for onset is first violated. These effects have not been taken into account in these results.

We observe from Figure (5.6a) that the peak electron temperature is greater at time t=8 scale times than it is when a steady-state is found for the cases when the mesh length is shorter (sections 5.4 and 5.5) and the temperature minimum is lower. In the light of what has been said in the last three sections most of the results here are self explanatory. It should be noted that although the y-component of the current is still small everywhere at all times compared to the z-

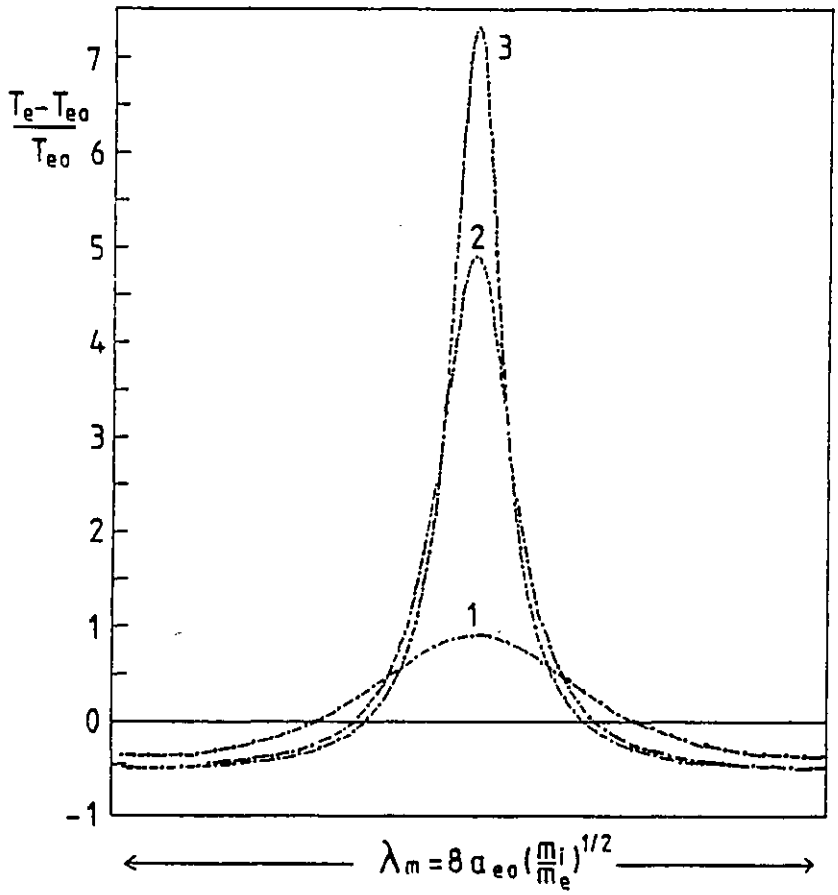

Figure 5.6a Electron temperature profiles at times 1) t=3, 2) t=7, 3) t=8.

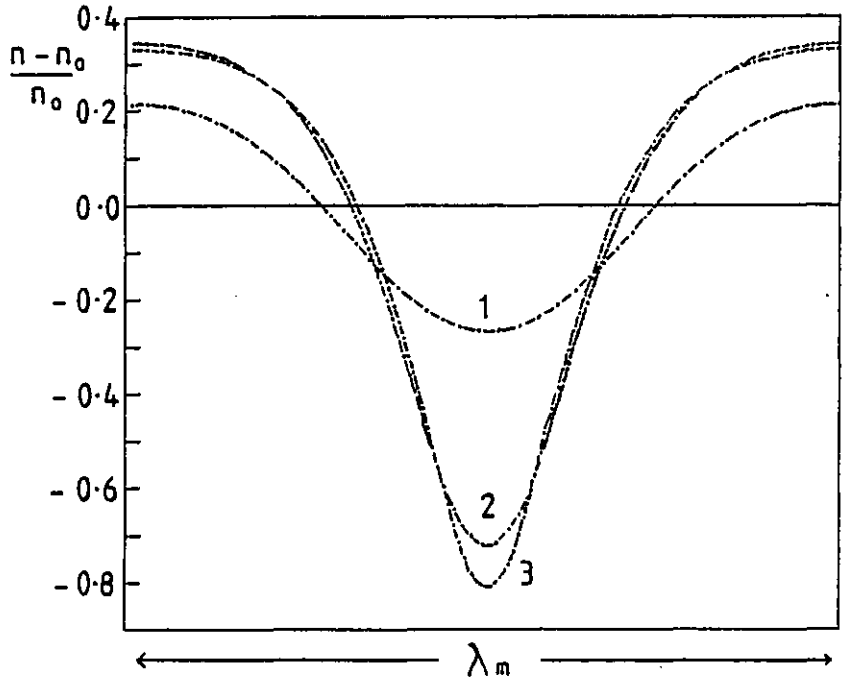

Figure 5.6b Number density profiles at times 1) t=3, 2) t=7, 3) t=8.

Figures 5.6

Mesh length set to eight scale lengths

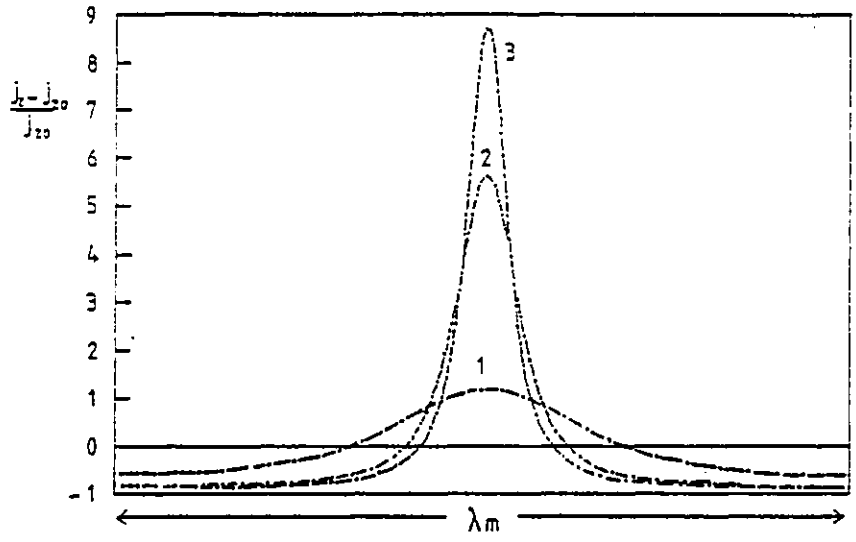

Figure 5.6c z-component of current density profiles at 1) t=3, 2) t=7, 3) t=8.

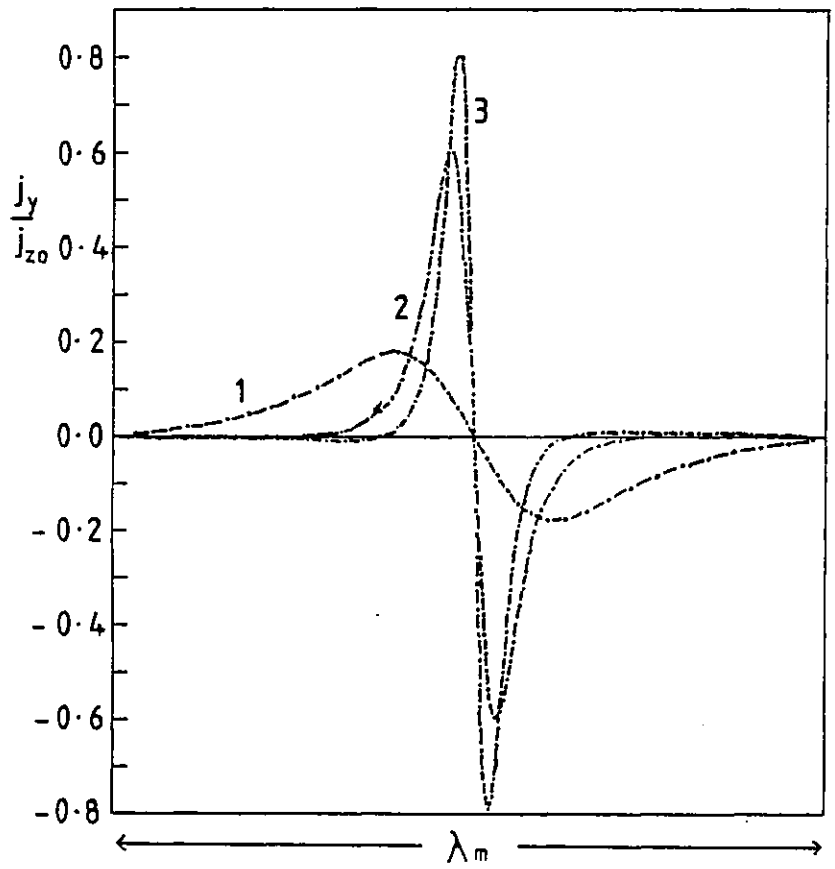

Figure 5.6d y-component of current density profiles at 1) t=3, 2) t=7, 3) t=8.

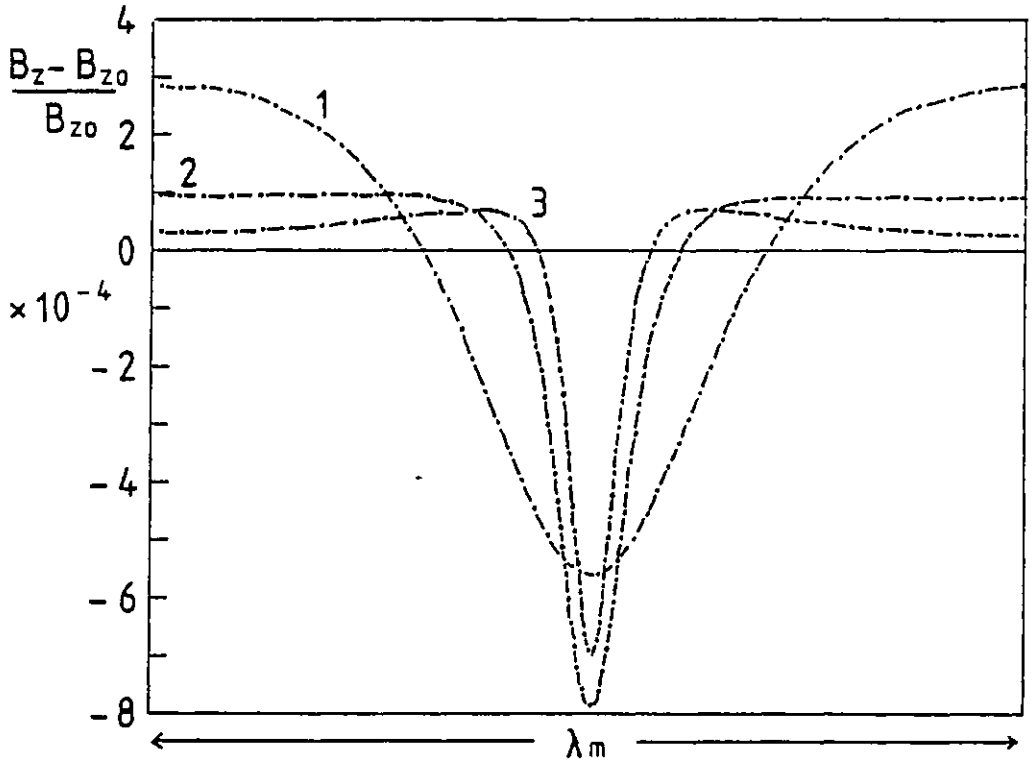

Figure 5.6e z-component of magnetic field at 1) t=3, 2) t=7, 3) t=8.

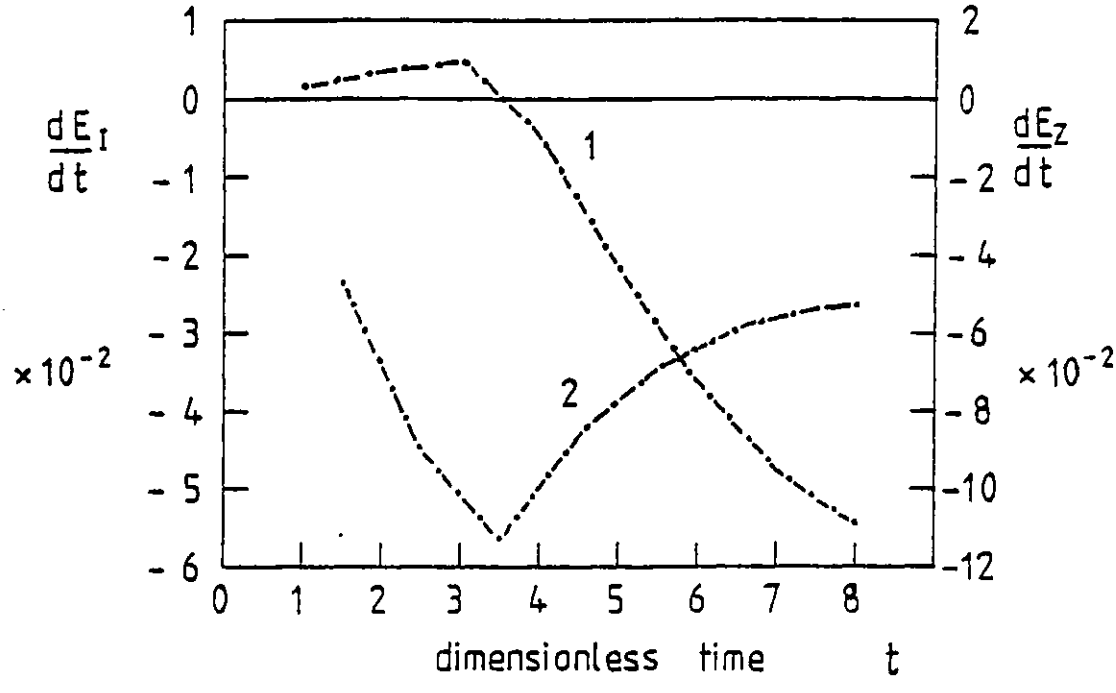

Figure 5.6f Variation in time of 1) the rate of change of the internal energy, 2) the rate of change of the applied electric field.

component it is certainly larger here comparatively than in the cases considered in the last two sections. Likewise the perturbation of the magnetic field is greater although still very small in absolute terms.

5.7 SUMMARY OF RESULTS

Further runs on the computer were produced with the mesh length increased above eight scale lengths. These results do not add any further information to or change the conclusions that can be made from the results presented here. Therefore they are not included.

We have demonstrated that the wavelength with the largest linear growth rate dominates in the non-linear regime. Valid steady-state solutions were found only for the cases where the mesh length was limited such that only short wavelength modes could grow; valid in the sense that our fluid model of the system is still applicable, and also in the sense that corrections or changes to the model do not have to be made due to the presence of ion acoustic instability. From the steady-state solutions obtained by following the evolution of the electrothermal instability we can say that the value of A_H^2 decreases as the mesh length increases. Also the longer the mesh length the lower is the final energy state of the system (the value of $E_I = p + \frac{B_z^2}{\pi_e}$), and the lower the value of the applied electric field E_z required to maintain constant total current. A_H^2 for a given value of T_i (dimensionless T_i) is a measure of the ratio E_z^2/p^2 in the steady-state. As the mesh length is increased the electron temperature and current filaments become more spiky and the troughs flatter while the amplitude of the electron temperature oscillation increases. The shorter the mesh length the longer is the time taken to reach a steady-state. This point can be understood by remembering that shorter wavelengths have smaller growth rates. The instability saturates at smaller deviations

from the initial steady-state (before the perturbation is applied) as the mesh length is decreased. It must be pointed out here that the absolute value of the time when the instability saturates and reaches a steady-state must be treated carefully as its value varies with the amplitude and shape of the initial perturbation.

We now turn our attention to the results obtained for longer mesh lengths. Some general comments can be made about the behaviour of the system when a short mesh length is used and those when a longer mesh length is used. Firstly "valid" steady-state solutions are not obtained. Secondly the shape and behaviour of the profiles change. The electron temperature filaments are less sharply peaked with steeper sides. The number density develops a maximum at the position of the density minimum (see Figure 5.3b). Both these features are due to the no longer negligible presence of the y-component of the current density compared to the z-component as explained in Section 5.3. For the cases where steady-state solutions were obtained,

$$j_y \ll j_z \quad \text{everywhere at all times} \tag{5.7.1}$$

Hence j_y is now playing an important part in the evolution of the electro-thermal instability to such an extent that the maximum Ohmic heating rate is no longer necessarily at the very peak of the electron temperature profile.

In Section 5.2 the comment was made that the amount of energy going into the y-component of the magnetic field is negligibly small. This assumption can be roughly tested by calculating the magnetic field generated by the perturbed current j_z. Using Faraday's Law we can approximate the back emf generated by the changing magnetic field and compare this with the applied electric field at a given time. This

method gives only an approximate idea of the effect of neglecting B_y, Approximate because these effects should be included self consistently. In all cases the back emf calculated in this manner was less than a few percent of the applied electric field at a given time.

We have illustrated the general behaviour of the system as the mesh length is increased. It must be stated here that the most important results are those obtained when the mesh length is set equal to the optimum wavelength for growth, because this mode would be expected to dominate in a real device as it is shown to do here.

CHAPTER 6

INTRODUCTION

In the last chapter we showed that the electrothermal instability leads to current filamentation in its non-linear stage. When the mesh length is set equal to the largest value this model will allow, the amplitude of the filaments becomes sufficiently large for ion acoustic turbulence to develop. We now formulate a model to include the effects of ion acoustic instability on the further evolution of the system.

6.1 THE MACROSCOPIC EFFECTS OF ION ACOUSTIC INSTABILITY

The nature and behaviour of the ion acoustic instability can only be obtained using a kinetic model. This is because the presence of this instability depends upon the details of the distribution functions. Hence its behaviour could not be simulated using our fluid model. However it is known[33] that the fully developed instability produces an effective electron-ion collision frequency which is much greater than classical. From a recent review[34] of ion acoustic turbulence typical values of the effective collision frequency are,

$$\nu_{eff} = (10^{-3} \rightarrow 3 \times 10^{-5})\ \omega_{pe} \qquad (6.1.1)$$

where ω_{pe} is the plasma frequency. Hence for Tokamak devices we can safely say,

$$\nu_{eff} >> \nu_{classical} \qquad (6.1.2)$$

The increased effective collision frequency results from enhanced electron collisions due to ion sound turbulence. The values quoted here are from theories and particle-in-cell simulations based on ion tail formation being the saturation mechanism[33,35]. Simulations show three distinct phases of growth of ion sound turbulence. The early phase is exponentially growing in time. The middle phase grows roughly linearly in time and marks the onset of non-linear modifications of the plasma processes. The final phase is the saturated phase. Workers differ to some extent on the late-time evolution. The time of evolution of the instability to saturation in present simulations is typically $100\ \omega_{pi}^{-1}$. Comparing this to the growth time of the electrothermal instability we get,

$$\frac{100}{\omega_{pi}}\ \frac{m_e}{m_i}\ \nu_{class} = \frac{100}{\sigma}\ \left(\frac{ne^2}{4\pi m_i}\right)^{\frac{1}{2}} \simeq 10^{-3}\ \left(\frac{n}{T_e^3}\right)^{\frac{1}{2}} \qquad (6.1.3)$$

From relation (6.1.3) we can say the ion acoustic turbulence grows and saturates in a time very much shorter than the time scale of interest in our model. The fastest growing modes (for ion sound turbulence) are those with wavenumber K such that,

$$K\ \lambda_D \simeq \sqrt{2}/2 \qquad (6.1.4)$$

where λ_D is the Debye length.

We know the ion acoustic instability grows and saturates in a time which is very much shorter than even the time step used in our simulation. During this short time the collision frequency could increase to a very high value. We therefore simulate the effect of ion acoustic turbulence by modelling the time averaged behaviour. This can be approximated when we have answered the question, what is the effect on

the filament of increasing the electron-ion collision frequency at the points where the condition for onset of ion acoustic instability is violated?

6.2 CHANGES TO THE MODEL

If the collision frequency increases, the electrical conductivity decreases as can be seen from equation (6.2.1)

$$\sigma = \frac{ne^2}{m_e \nu_{ei}} \quad \text{in cgs units} \tag{6.2.1}$$

The dependence of the thermal conductivity perpendicular to the magnetic field $\chi_{\perp e}$ is less straightforward,

$$\text{in cgs units} \quad \chi_{\perp e} = \frac{K_e}{(1+\omega_e^2\tau_e^2)} = \frac{5}{2}\frac{n K_B T_e}{m_e \nu_{ei}} \frac{1}{\left(1+\frac{eB}{m_e c \nu_{ei}}\right)^2} \tag{6.2.2}$$

However, provided $\omega_e\tau_e >> 1$ still holds equation (6.2.2) may be simplified to

$$\chi_{\perp e} = \frac{K_e}{\omega_e^2\tau_e^2} \simeq \frac{5}{2}\frac{n K_B T_e m_e c^2 \nu_{ei}}{e^2B^2} \tag{6.2.3}$$

In which case equation (6.2.3) tells us the thermal conductivity perpendicular to the magnetic field increases with collision frequency. Looking at the equations used to describe the evolution of the system, only the electron heat balance equation (4.1.6) and Ohm's Law, equations (4.1.4) and (4.1.5) are directly affected by σ and $\chi_{\perp e}$. If the collision frequency were increased less current would be driven in this region and hence the drift velocity would fall. Assuming the increase in collision frequency is sufficiently large the electron temperature would fall because of the increased equipartition and thermal conduction rates.

The ion acoustic instability arises when $T_e >> T_i$ and a current flow drives an electron drift with velocity $V_d > c_s$, the ion sound speed. Therefore if increasing the collision frequency acts to reduce the drift velocity and the electron to ion temperature ratio the region will quickly become ion acoustic stable, with the collision frequency returning to its classical value. This will decrease the rate of energy dissipation and increase the Ohmic heating rate resulting in an increase in electron temperature accompanied by an increase in drift velocity. Once again the conditions for ion acoustic instability will be present. In this way the region will oscillate in time about the marginal stability condition for ion acoustic turbulence. We therefore approximate the time averaged behaviour by assuming that once the marginal stability condition is reached at any point the collision frequency increases to maintain marginal stability at that point. Let us assume the dimensionless collision frequency increases to ν^* given by,

$$\nu^* = \xi \nu \tag{6.2.4}$$

where ν is the dimensionless classical collision frequency. The anomaly factor ξ is found by using the condition for onset of ion acoustic turbulence which is,

$$\text{in cgs units} \quad V_d > \left(\frac{m_e}{m_i}\right)^{\frac{1}{2}} \left(\frac{k_B T_e}{m_e}\right)^{\frac{1}{2}} + \left(\frac{m_i}{m_e}\right)^{\frac{1}{2}} \left(\frac{k_B T_i}{m_i}\right)^{\frac{1}{2}} \tag{6.2.5}$$

as an upper limit for the drift velocity. The drift velocity V_d may be written in terms of the current density,

$$\text{in cgs units} \quad V_d = \frac{(j_y^2 + j_z^2)^{\frac{1}{2}}}{ne} \tag{6.2.6}$$

In terms of the dimensionless quantities defined in (4.1.11) relation (6.2.5) becomes,

$$\frac{A_F\,(\tilde{j}_y^{\,2} + \tilde{j}_z^{\,2})^{\frac{1}{2}}}{\tilde{n}} > \tilde{T}_e^{\,\frac{1}{2}} + \tilde{T}_i^{\,\frac{1}{2}}\,(\frac{m_i}{m_e})^{\frac{1}{2}} \tag{6.2.7}$$

Again the tilde notation will be dropped and the quantities when referred to are dimensionless unless otherwise stated. At marginal stability, the current density is obtained from relation (6.2.7),

$$(j_y^{\,2} + j_z^{\,2})^{\frac{1}{2}} = \frac{n}{A_F}\,(T_e^{\,\frac{1}{2}} + T_i^{\,\frac{1}{2}}\,(\frac{m_i}{m_e})^{\frac{1}{2}}) \tag{6.2.8}$$

However the current density must also obey Ohm's Law, equations (4.1.17) and (4.1.18), that is,

$$(j_y^{\,2} + j_z^{\,2})^{\frac{1}{2}} = \sigma^*\,[(E_y - \frac{V_x B_z}{A_F})^2 + E_z^{\,2}]^{\frac{1}{2}} \tag{6.2.9}$$

where σ^* is the dimensionless electrical conductivity decreased as a result of the increased collision frequency,

$$\sigma^* = \frac{\sigma}{\xi} \tag{6.2.10}$$

Equations (6.2.8), (6.2.9) and (6.2.10) are combined to find the anomaly factor ξ giving,

$$\xi = \frac{A_F\sigma}{n}\,[(E_y - \frac{V_x B_z}{A_F})^2 + E_z^{\,2}]^{\frac{1}{2}}\,[T_e^{\,\frac{1}{2}} + (\frac{m_i}{m_e})^{\frac{1}{2}}\,T_i^{\,\frac{1}{2}}]^{-1} \tag{6.2.11}$$

The introduction of an increased collision frequency to maintain marginal stability is consistently incorporated in the program as follows. When the system is approaching the condition for onset of ion

acoustic instability the solutions are tested at each mesh point at every time step. If condition (6.2.7) is true at any point on the mesh at time step n+1 we say the solutions at this time step are invalid. At the mesh points where the condition for onset is violated, we use the invalid solutions in the right hand side of equation (6.2.11) to obtain a first approximation for the anomaly factor ξ. This value of ξ is used to calculate the dimensionless anomalous electrical conductivity σ^* as defined in (6.2.10), and the dimensionless anomalous thermal conductivity $\chi_{\perp e}^*$ defined as,

$$\chi_{\perp e}^* = \xi \chi_{\perp e} \tag{6.2.12}$$

where $\chi_{\perp e}$ is the dimensionless thermal conductivity as defined in equation (4.1.19). At the mesh points where the ion acoustic instability condition is not violated ξ is set equal to one. With these values of $\chi_{\perp e}^*$ and σ^* we find the next approximation to the solution of equations (4.1.14-20) at time step n+1. Again the solutions are tested for ion acoustic instability and using the same method as before a second approximation for ξ is obtained. We note here that once the marginal condition for ion acoustic instability has been reached at any mesh point marginal stability is maintained at that mesh point for all future time. This means that if our first approximation for ξ is so large that the next approximate solutions produce results showing ion acoustic stability this would not be acceptable. The only acceptable results are those showing marginal stability. The iteration procedure is repeated obtaining successively improved values of ξ and all other variables until convergence is achieved. In practice convergence was achieved more rapidly by using a combination of the p^{th} and $p\text{-}1^{th}$ values of ξ in the $p+1^{th}$ iteration instead of using the p^{th} i.e.

$$\xi^{p+1} = (\xi^{p}-1) + \xi^{p-1} \qquad (6.2.13)$$

where p denotes the iteration number.

6.3 RESULTS FROM THE MODEL INCLUDING THE EFFECTS OF ION ACOUSTIC TURBULENCE

The results from the simulation described in section three of Chapter 5, at a time just before the conditions for onset of ion acoustic instability are met, are used as a starting point for this simulation. The model and equations are changed according to the prescriptions given in the last section and the run continued. The results obtained are shown in Figures (6.3). The curve labelled 1 in Figure (6.3a) shows the perturbed electron temperature profile at a time just before the anomalous collision frequency is introduced. Looking at the curves labelled 2 and 3 we can see that the electron temperature filament continues to grow. This shows the Ohmic heating rate is still larger than the total energy dissipation rate despite the introduction of the anomalous collision frequency. However the width of the filament increases with time instead of decreasing. This can be understood by looking at the current density profiles in Figures (6.3b) and (6.3c). The z-component of the current density is falling in the region where an anomalous collision frequence exists, as expected. In order to maintain constant total current the width of the current filament is increasing so that more current is flowing in regions where the z-component of the current density was previously low. Hence the Ohmic heating rate rises expanding the width of the electron temperature filament. We also observe the z-component of the current density develops two spikes which mark the edges of the region where an anomalous collision frequency exists. Current is being expelled from

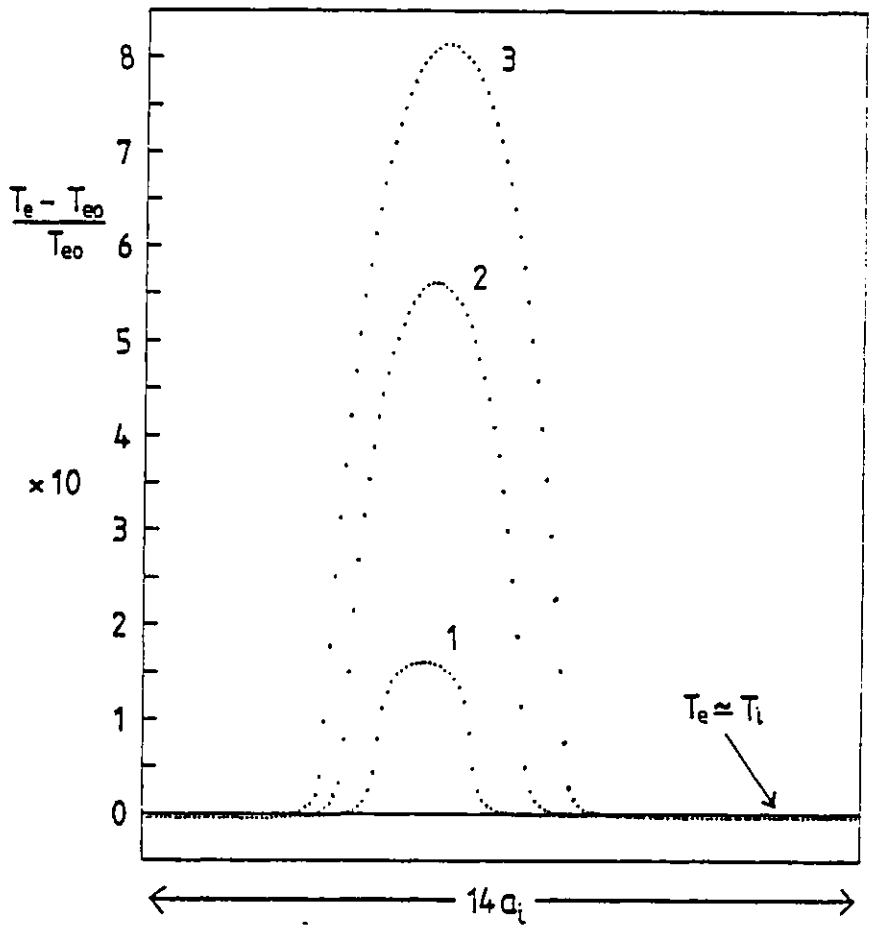

Figure 6.3a Electron temperature profiles at times 1) t=12 just before ion acoustic instability condition is violated, 2) t=27, 3) t=37.

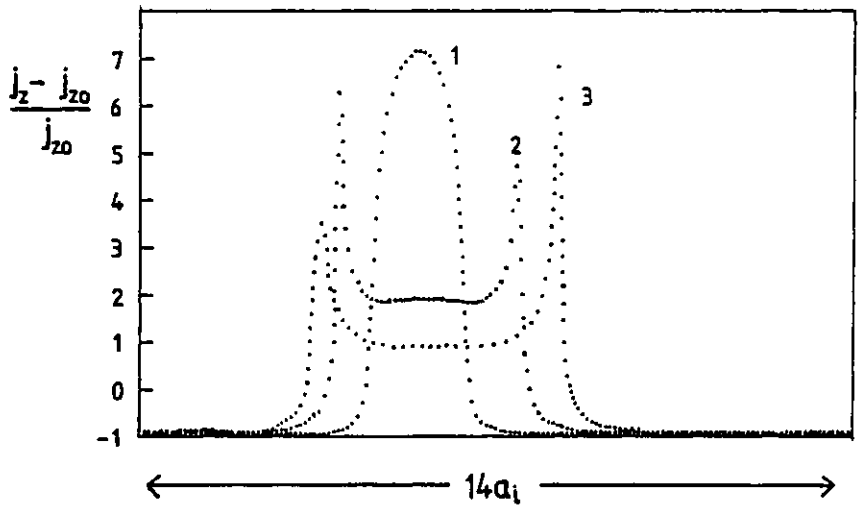

Figure 6.3b z-component of current density profiles at times 1) t=12, 2) t=27, 3) t=37.

Figures 6.3

Results obtained including the effects of ion acoustic turbulence

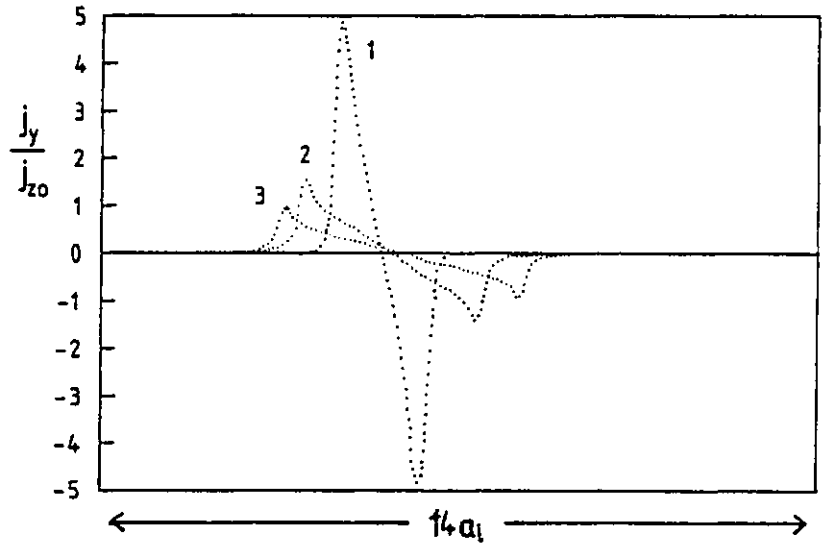

Figure 6.3c y-component of current density profiles at 1) t=12, 2) t=27, 3) t=37.

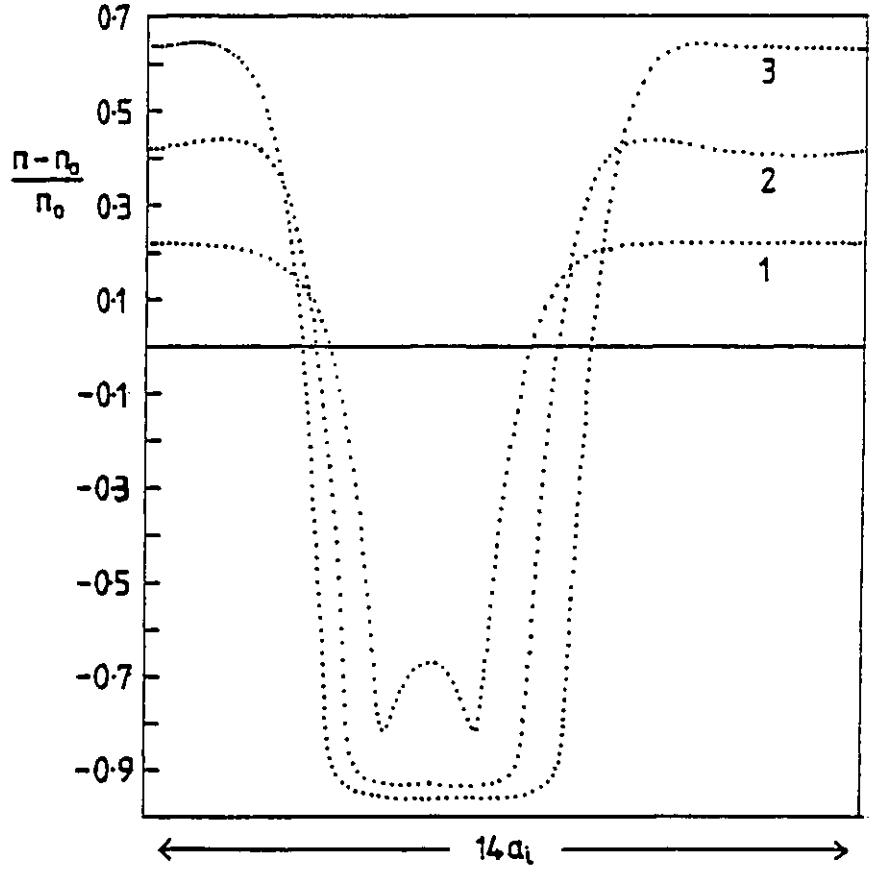

Figure 6.3d Number density profiles at 1) t=12, 2) t=27, 3) t=37.

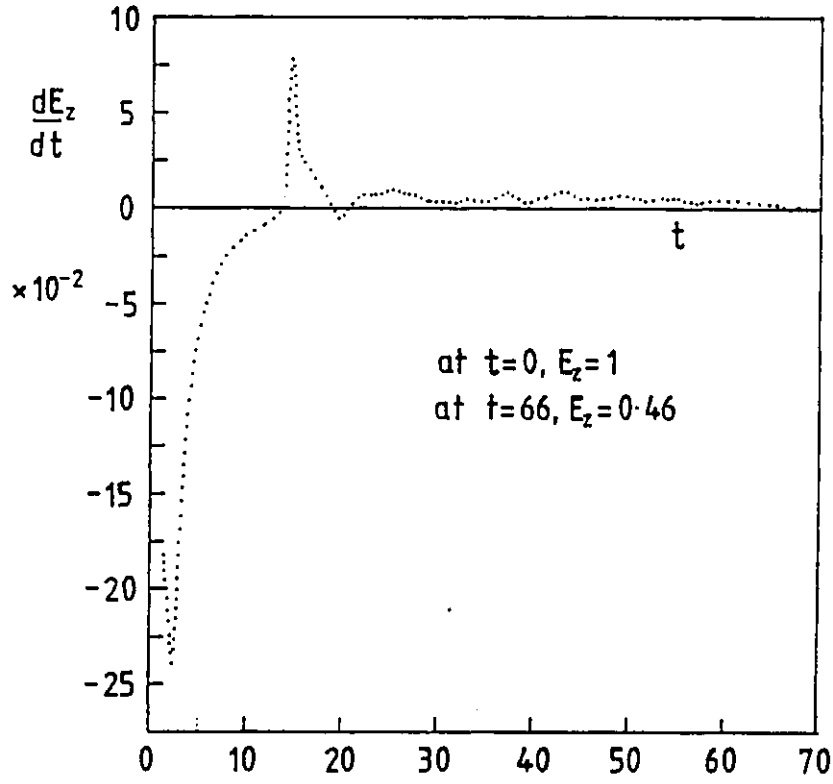

Figure 6.3e Variation in time of the rate of change of the applied electric field required to maintain constant total current.

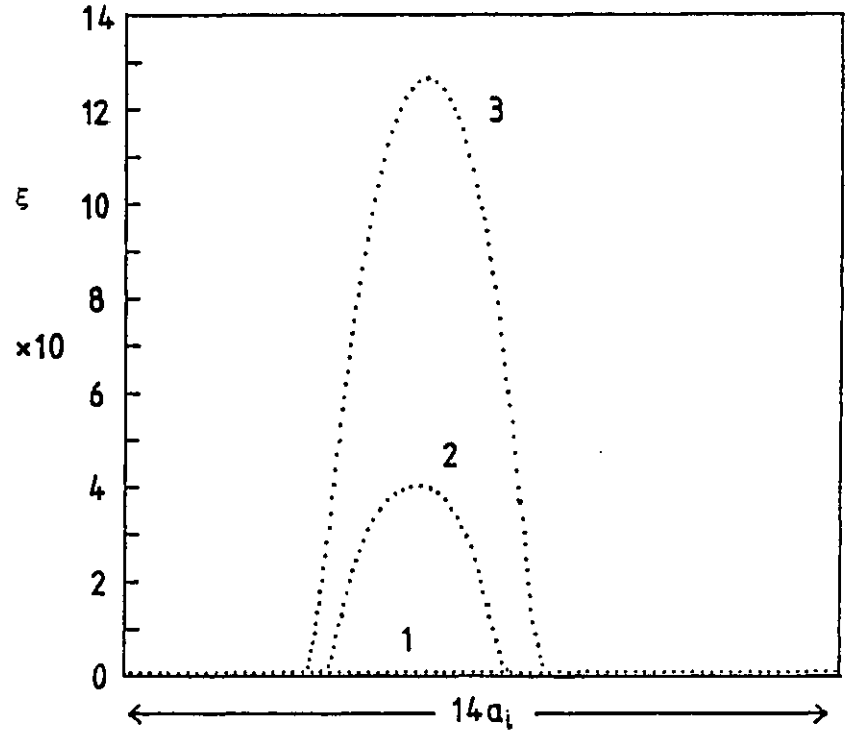

Figure 6.3f Spatial variation of anomaly factor ξ at times 1) t=12, 2) t=27, 3) t=37.

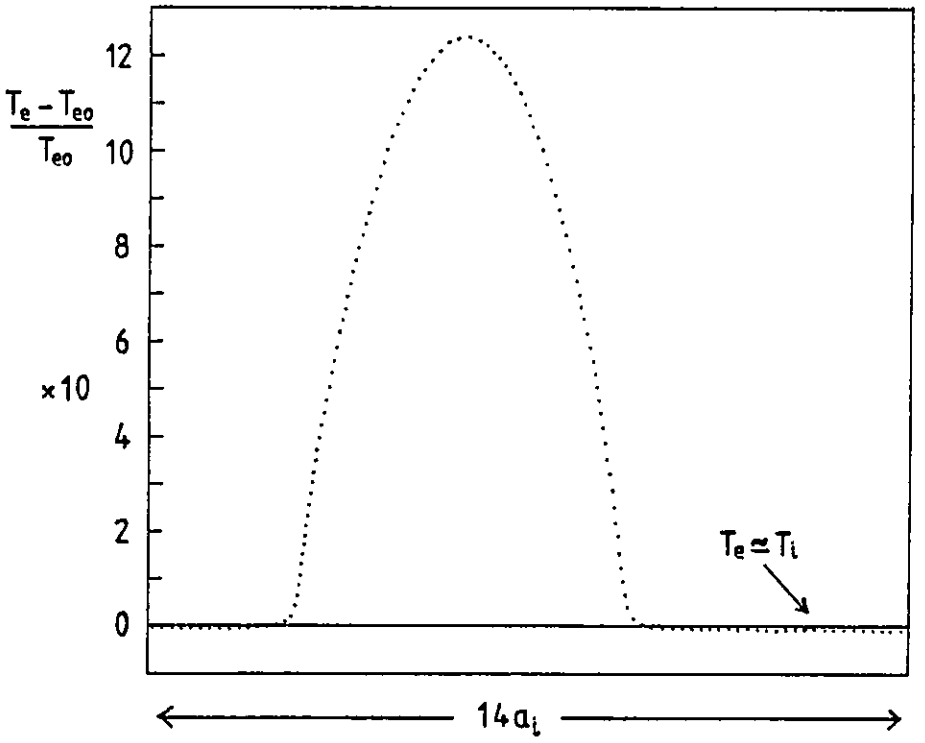

Figure 6.3g Steady-state electron temperature profile.

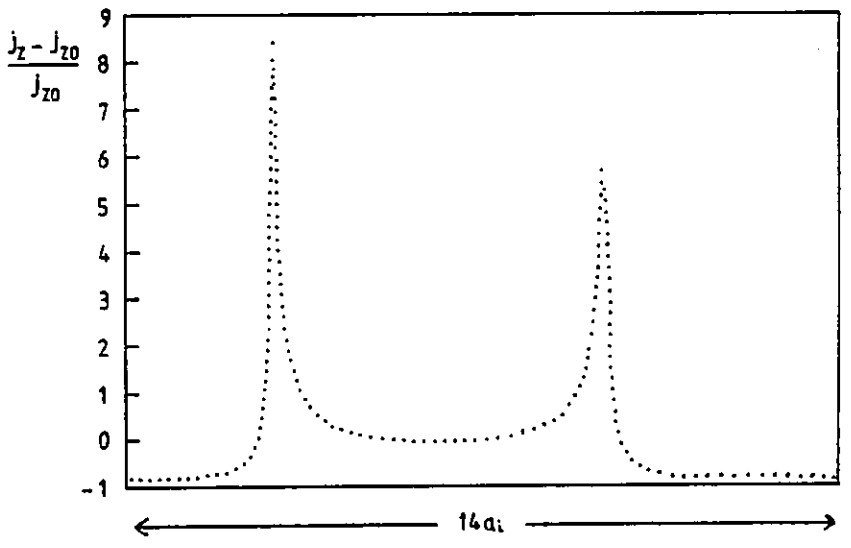

Figure 6.3h z-component of current density at the steady-state.

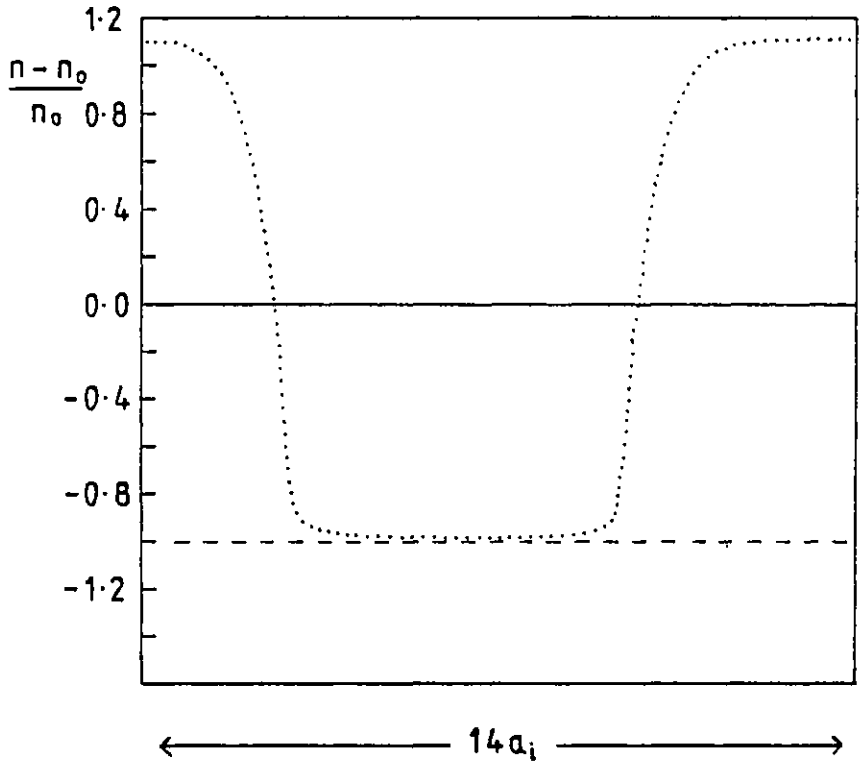

Figure 6.3i Steady-state density profile.

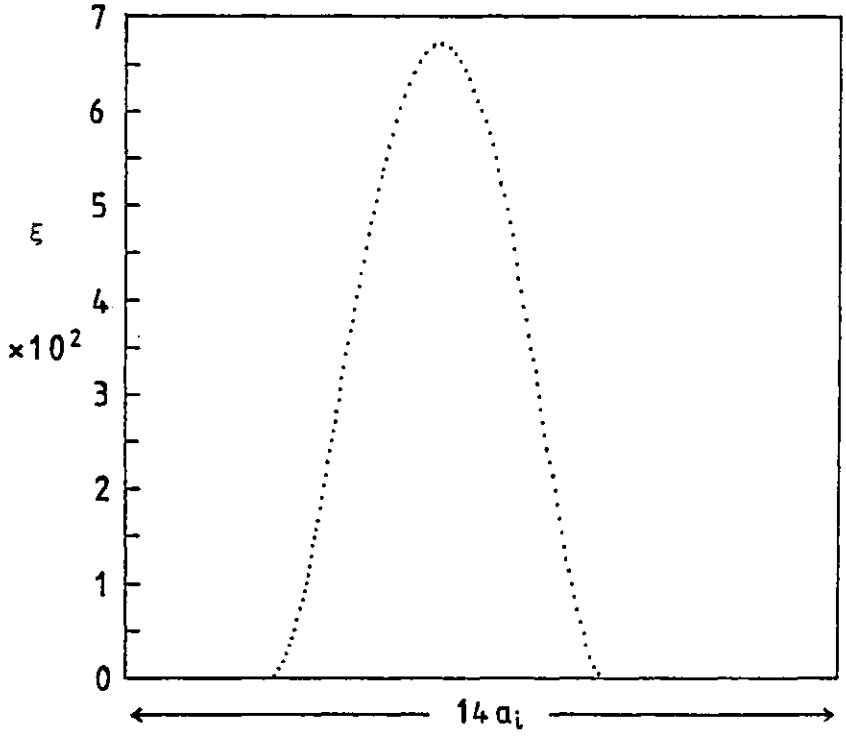

Figure 6.3j Spatial variation of anomaly factor ξ at the steady-state.

the region between the spikes because of the high resistivity brought about by the anomalous collision frequency, while either side of the spikes the resistivity is high because of the lower electron temperature. Therefore the spikes develop because these regions offer paths of least resistance. This explanation is upheld by the behaviour of the y-component of the current density which is also being expelled from the region affected by ion acoustic turbulence and concentrating in the same regions as the z-component. However the total magnitude of the y-component of the current density is decreasing in time. As can be seen from Figure (6.3e) the electric field E_z starts to rise shortly after the onset of ion acoustic turbulence and continues to do so because the current cannot be instantaneously expelled from the anomalous region at any given time in order to maintain constant total current. Plots of the number density profile at various times, Figure (6.3d), show that particles are still evacuating the high electron temperature region. The number density minimum becomes square and the secondary maxima disappears as a result of the combined effects of the y-component of the current density dying away and becoming once again much smaller than the z-component, and the development of the spikes in the z-component. Figure (6.3f) shows the width of the region affected by ion acoustic turbulence is increasing in time. Furthermore the anomaly factor ξ increases in time showing the collision frequency has to become more and more anomalous to keep marginal stability.

After a time equal to about sixty six scale times the system is approaching a steady state; the centre of mass velocity, the y-component of the current and the total pressure gradient are all very close to zero while the time rate of change of any quantity is very small. The steady-state electron temperature, current and number density profiles are plotted in Figures (6.3g-i) and the steady-state anomaly factor ξ is

plotted in Figure (6.3j). The maximum electron temperature is about 120 times the initial equilibrium value while the minimum electron temperature is very nearly equal to the ion temperature.

6.4 THE EFFECTS OF THE PRESENCE OF THE FILAMENTS ON ENERGY TRANSPORT

We are now in a position to test the hypothesis that the presence of a fully developed electrothermal instability may increase the rate at which energy is equipartitioned to the ions from the electrons to a value above that deduced from experiments. The separation of the electron temperature filaments if they existed would be about $20\ a_{eo}\ (\frac{m_i}{m_e})^{\frac{1}{2}}$. Such fine scale structure would not be detected using existing experimental methods. In a Tokamak the electron density and temperature are most reliably measured by Thomson scattering. There are typically only 1-4 laser pulses of short duration ($\sim$ 25 ns) during a discharge pulse giving 1-4 time resolved measurements at one point in the plasma. Thus to build up radial profiles requires many pulses and good plasma reproducibility. Even using a high brightness laser, and complex detection systems, it is only possible to measure the parameters at several radial positions from a single laser pulse[23]. Using Thomson scattering an experimentalist would measure the average electron temperature over the scattering volume weighted with density[33]. It is generally assumed that the equipartition rate is classical. Therefore the average equipartition rate as calculated from Thomson scattering measurements would be

$$E_{q\ scat} = \frac{3\ \bar{n}^2\ e^2\ k_B\ (T_{e\ scat} - T_i)}{m_i\ \alpha^1\ T_{e\ scat}^{3/2}} \qquad (6.4.1)$$

where $\bar{n} = \frac{1}{\lambda_m} \int_o^{\lambda_m} n(x)\ dx\ cm^{-3}$ (6.4.2)

$$\text{and} \qquad T_{e\ scat} = \frac{1}{\bar{n}\,\lambda_m} \int_o^{\lambda_m} n(x)\ T_e(x)\ dx\ ^\circ K \tag{6.4.3}$$

The electrical conductivity is known from experiment to agree well with the Spitzer formula which has been used in equation (6.4.1). We must compare $E_{q\ scat}$ with $E_{q\ et}$, the average equipartition rate calculated taking into account the fine scale filamentary structure, and the anomalous collision frequency in regions affected by ion acoustic turbulence,

$$E_{q\ et} = \frac{1}{\lambda_m} \int_o^{\lambda_m} \frac{3n^2(x)\ e^2 k_B (T_e(x) - T_i)}{m_i\ \alpha^1\ T_e(x)^{3/2}}\ \xi\ dx \tag{6.4.4}$$

If our hypothesis is correct,

$$\frac{E_{q\ et}}{E_{q\ scat}} > 1 \tag{6.4.5}$$

Not only should condition (6.4.5) be true, but also the presence of the filaments and associated regions of ion acoustic turbulence must be shown not to give rise to differences between the calculated and experimentally measured values of electrical conductivity. As previously stated these two values should agree well. Therefore we also compute the ratio,

$$\frac{\sigma_{scat}}{\sigma_{et}} = \frac{\alpha^1\ T_{e\ scat}^{3/2}}{\sigma_{et}} \tag{6.4.6}$$

where

$$\sigma_{et} = \frac{1}{\lambda_m} \int_o^{\lambda_m} \frac{j_z}{E_z}\ dx \tag{6.4.7}$$

Returning to our dimensionless units and remembering the total current

is held constant and the electric field E_z is not a function of position we obtain,

$$\frac{E_{q\ et}}{E_{q\ scat}} = \left[\frac{\bar{n}^2 (T_{e\ scat} - T_i)}{T_{e\ scat}^{3/2}} \right]^{-1} \frac{1}{\lambda_m} \int_o^{\lambda_m} \frac{n^2(x)\ (T_e(x) - T_i)}{T_e(x)^{3/2}}\ \xi\ dx \tag{6.4.8}$$

and

$$\frac{\sigma_{scat}}{\sigma_{et}} = T_{e\ scat}^{3/2}\ E_z \tag{6.4.9}$$

From the steady-state solutions the final electric field is equal to 0.46 of its initial value before the perturbation was applied, and from the results shown in Figures (6.3g) to (6.3j) we obtain,

$$\frac{E_{q\ et}}{E_{q\ scat}} = 0.4302 < 1 \tag{6.4.10}$$

and

$$\frac{\sigma_{scat}}{\sigma_{et}} = 1.09 \tag{6.4.11}$$

Relation (6.4.10) tells us that the presence of the filaments leads to a reduced rather than an enhanced energy equipartition rate. The equipartition rate goes as,

$$E_q \propto \frac{n^2 (T_e - T_i)}{\sigma} \tag{6.4.12}$$

Now $T_{e\ scat}$ is the dimensionless average electron temperature weighted with number density. The density is a minimum where the electron

temperature is a maximum and vice versa. From the steady-state results,

$$T_{e\ scat} = 1.7575 \qquad (6.4.13)$$

The average dimensionless number density $\bar{n}$ defined in relation (6.4.2) is equal to one because mass can neither enter nor leave the system at any time and therefore the final average number density equals the initial uniform number density. Therefore $E_{q\ scat}$ is approximately one half the initial equilibrium equipartition rate. In the electron temperature peaks the number density is very small. Despite the anomalously high collision frequency there the equipartition rate is still only about 2% of the initial equilibrium value. In the electron temperature troughs the electron temperature is very nearly equal to the ion temperature producing a very small value for the equipartition rate in this region. This explains the result obtained in (6.4.10).

6.5 SUMMARY OF THE RESULTS

We have included the effects of ion acoustic turbulence by introducing an anomalous collision frequency in the region concerned in such a way as to maintain marginal stability. Current is expelled from the region because marginal stability is held by imposing,

$$|j| \propto n\ (T_e^{\frac{1}{2}} + \text{constant}) \qquad (6.5.1)$$

The number density continues to fall because the pressure is still high in this region and hence the current density falls. Condition (6.5.1) then determines the anomalous collision frequency. The current spikes at the edges of the turbulent region arise because of the strict adherence to the constant total current condition and because of the

abrupt onset in time and space of ion acoustic turbulence. Therefore we would not expect the spikes to occur in reality. After about seventy linear growth times the system reaches a steady-state. The electron temperature filament persists accompanied by a sharp number density well. The fine scale structure of the filament is shown to decrease the value of the average equipartition rate compared with that calculated from experimental results, while the electrical conductivity is unaffected.

6.6 DIRECT ION HEATING BY ION ACOUSTIC TURBULENCE

An important effect which has been neglected in this model is the direct heating of the ion tail by the ion acoustic turbulence. This is thought by some authors to be responsible in some numerical simulations for the saturation of the ion acoustic instability, and could be allowed for in this model by postulating that a fraction of the Ohmic heating rate $\delta\ \underline{J}.\underline{E}$ from the energy source $\underline{J}.\underline{E}$ goes directly into ion heating. Hence the Ohmic heating of the electrons will be reduced to $(1-\delta)\underline{J}.\underline{E}$. The value of the variable δ can be approximated from values of the electron and ion heating rates calculated by Weinstock and Sleeper[36], though it should be noted that this particular paper postulates ion resonance broadening rather than ion tail formation as the saturation mechanism. Further studies are being made of both PIC numerical simulation results and the analytic work of Vekstein and Sagdeev[37]. The inclusion of direct ion heating may well change the results described in this chapter.

CONCLUSION

We have extended the work of other authors on the linear behaviour of the electrothermal instability. From this work we

conclude that the effect of taking into account the changes in the y-component of the magnetic field ($B_y << B_z$ assumed) on the linear behaviour of the electrothermal instability are negligible for wavelengths up to and including the optimum wavelength for growth ($\lambda_{optimum} \sim$ few $a_{eo} (\frac{m_i}{m_e})^{\frac{1}{2}}$). The inclusion of deviations from $\nabla p = \frac{\underline{j} \times \underline{B}}{c}$ are also shown to have negligible effects on the behaviour of the electrothermal instability. The inclusion of Bremsstrahlung radiation loss or indeed any radiation loss with an $n^2 T_e^{\gamma}$ (where $\gamma \leq \frac{1}{2}$ such as impurity) dependence enhances the growth rate of the instability.

Solutions of the steady-state electron energy equation show the possibility of the existence of a sharply peaked filamentary structure for the electron temperature and current profiles at saturation of the instability. Such profiles only exist for the electric field less than a critical value. For some of these solutions, the conditions for onset of ion acoustic instability are violated in the filament peaks. For solutions with very large amplitude filaments, the conditions for full electron runaway are violated in the current and temperature peaks, while the average values of the plasma parameters preclude the existence of either of these phenomena.

A numerical simulation of the development in time of the electrothermal instability from an initially small, random perturbation confirms the development of the filaments and shows their separation to be equal to the optimum wavelength for growth as calculated from linear theory (including B_y). However the filaments are of more uniform width and less sharply peaked than expected from the solutions of the steady-state electron energy equation mentioned in the last paragraph. The troughs are indeed very flat as predicted, and the filaments develop to sufficiently large amplitude and composition for ion acoustic instability to be triggered. Steady-state solutions which

agree very well with the steady-state solutions of the electron energy equation are found if only very short wavelength modes are permitted to grow. As the optimum wavelength mode is shown to dominate, these results only serve to give confidence in the computer program.

When the effects of ion acoustic turbulence are included by introducing an increased effective electron-ion collision frequency the system reaches a steady-state in approximately seventy linear growth times. The electron temperature filament persists although its width is increased and it is less spiky. The current density is concentrated in the transition regions from anomalous to classical collision frequency. However, the presence of the filament, from this model, does not lead to an enhanced energy equipartition rate. Including the direct heating of the ions due to ion acoustic turbulence in this model may considerably change these results.

APPENDIX A

RECURRENCE SOLUTION OF A BLOCK PERDIAGONAL MATRIX EQUATION

We wish to solve the matrix equation AU = W, rapidly, where A is a block tridiagonal matrix with additional blocks in the upper right and lower left corners, referred to here as perdiagonal.

The method of solution follows the principles for a recurrence solution of a tridiagonal matrix equation[28], modified to deal with the more complex case of periodic boundary conditions. We are interested in solving equations of the form,

$$\alpha_j\, U_{j+1} + \beta_j\, U_j + \gamma_j\, U_{j-1} = W_j \qquad (1a)$$

at every mesh point j, j=1 to J, where α_j, β_j and γ_j are 3x3 submatrices and W_j and U_j are 3-component column vectors. Using periodic boundary conditions, $U_1 = U_J$ and $(\frac{dU}{dx})_1 = (\frac{dU}{dx})_J$, the number of independent equations reduces from J to J-1 and equation (1a) may be written in matrix form :

$$\begin{bmatrix} \beta_1 & \alpha_1 & 0 & . & . & . & \gamma_1 \\ \gamma_2 & \beta_2 & \alpha_2 & 0 & . & . & 0 \\ 0 & \gamma_3 & \beta_3 & \alpha_3 & . & . & 0 \\ . & & & & & & \\ . & & & & & & \\ . & & & & & & \\ \alpha_{J-1} & 0 & . & . & . & \gamma_{J-1} & \beta_{J-1} \end{bmatrix} \begin{bmatrix} U_1 \\ U_2 \\ U_3 \\ . \\ . \\ . \\ U_{J-1} \end{bmatrix} = \begin{bmatrix} W_1 \\ W_2 \\ W_3 \\ . \\ . \\ . \\ W_{J-1} \end{bmatrix} \qquad (2a)$$

Assume a recursive solution exists of the form,

$$U_{j-1} = \chi_j U_j + \psi_j U_{J-1} + Y_j \tag{3a}$$

where again χ_j and ψ_j are 3x3 matrices and Y_j is a 3-component column vector. If equation (3a) is applicable at the point j, for consistency it must be applicable at every other point so the same formula applies at the point j-1. Substituting equation (3a) for U_{j-1} in equation (1a) and rearranging,

$$U_j = -(\beta_j + \gamma_j \chi_j)^{-1} \alpha_j U_{j+1} - (\beta_j + \gamma_j \chi_j)^{-1} \gamma_j \psi_j U_{J-1} + (\beta_j + \gamma_j \chi_j)^{-1} (W_j - \gamma_j Y_j) \tag{4a}$$

Equation (4a) has exactly the same form as the recursive relation equation (3a), namely,

$$U_j = \chi_{j+1} U_{j+1} + \psi_{j+1} U_{J-1} + Y_{j+1} \tag{5a}$$

Identifying coefficients in equations (4a) and (5a) gives the relations required to generate the successive values of χ_j, ψ_j and Y_j :

$$\chi_{j+1} = -(\beta_j + \gamma_j \chi_j)^{-1} \alpha_j$$

$$\psi_{j+1} = -(\beta_j + \gamma_j \chi_j)^{-1} \gamma_j \psi_j$$

$$Y_{j+1} = (\beta_j + \gamma_j \chi_j)^{-1} (W_j - \gamma_j Y_j) \tag{6a}$$

Using equation (3a) at the point j=2, comparing it with the original equation (1a) at the point j=1 gives the following expressions for χ_2, ψ_2 and Y_2,

$$\chi_2 = -\beta_1^{-1}\alpha_1$$

$$\psi_2 = -\beta_1^{-1}\gamma_1$$

$$Y_2 = \beta_1^{-1} W_1 \qquad (7a)$$

Applying relations (6a) at the point j=1 and comparing these with relations (7a), we obtain,

χ_1 is a null matrix

ψ_1 is the identity matrix

Y_1 is a null vector

The relations in (6a) are now used to scan the mesh upwards from j=2 to j=J-1 providing all required values of χ_j, ψ_j and Y_j. Equation (3a) is then used to scan the mesh downwards in j from j=J-1 to j=2 to determine values of U at every point j on the mesh. The values of U at every point j=J-1 is needed before the downwards scan can be carried out. This is achieved by solving two equations in the unknown variables U_{J-1} and U_{J-2}. The first equation is obtained as follows. Assume a relation exists,

$$e_j U_{j-1} + f_j U_{J-2} + g_j U_{J-1} = h_j \qquad (8a)$$

where e_j, f_j and g_j are 3x3 matrices and h_j is a 3-component column vector. Substituting the expression for U_{j-1} from equation (3a) into equation (8a) yields,

$$e_j \chi_j U_j + f_j U_{J-2} + (e_j \psi_j + g_j) U_{J-1} = h_j - e_j Y_j \qquad (9a)$$

Equation (9a) is of the same form as equation (8a), that is,

$$e_{j+1}\, U_j + f_{j+1}\, U_{J-2} + g_{j+1}\, U_{J-1} = h_{j+1} \qquad (10a)$$

Hence identifying coefficients in equations (9a) and (10a) we obtain the equations required to generate successive values of e_j, g_j, f_j and h_j,

$$\begin{aligned} e_{j+1} &= e_j\, X_j \\ f_{j+1} &= f_j \qquad \text{the elements of f do not vary with j} \\ g_{j+1} &= g_j + e_j\, \psi_j \\ h_{j+1} &= h_j - e_j\, Y_j \end{aligned} \qquad (11a)$$

If the original equation (1a) is applied at the point j = J-1 and U_J is replaced by U_1 we obtain an equation in the variables U_1, U_{J-1} and U_{J-2}. Now, applying equation (10a) at the point j=1 and comparing the coefficients with the equation described in the last sentence we obtain expressions defining e_2, g_2, h_2 and f,

$$\begin{aligned} e_2 &= \alpha_{J-1} \qquad & f &= \gamma_{J-1} \\ g_2 &= \beta_{J-1} \qquad & h_2 &= W_{j-1} \end{aligned} \qquad (12a)$$

The relations in (11a) are now used to scan upwards in j to find successive values of e_j, g_j and h_j and finally to find the values of e, g and h at the point j=J-1. We can then write an equation involving the variables U_{J-1} and U_{J-2} only from equation (10a),

$$(e_{J-1} + f)\ U_{J-2} + g_{J-1}\ U_{J-1} = h_{J-1} \tag{13a}$$

The other equation in U_J-1 and U_{J-2} only is obtained by applying equation (3a) at the point j=J-1. This equation is then used to eliminate U_{J-2} from equation (13a) giving an equation for U_{J-1} in terms of all known quantities, namely,

$$U_{J-1} = ((e_{J-1} + f)\ (\chi_{J-1} + \psi_{J-1}) + g_{J-1})^{-1} \times (h_{J-1} - (e_{J-1} + f)\ \psi_{J-1}) \tag{14a}$$

We now use this value of U_{J-1} to initiate the scanning procedure described previously. Hence we find U at every mesh point j.

APPENDIX B

NUMERICAL STABILITY OF THE DIFFERENCE SCHEME USING GERSCHGORIN'S THEOREM

The simplest way of implementing Gerschgorin's theorem is to start by guessing a stable time step Δt for a given mesh spacing Δx. The elements of the matrix K_{im} (4.3.2) are known at a given mesh point j at time level n. Therefore we can find analytically the elements of the amplification matrix G using equations (4.7.8) and (4.7.10) for the "worst case", $\sin^2 \frac{K\Delta x}{2} = 1$. We now compute the three separate sums of the rows, using the chosen value of Δt, and store the sum of greatest magnitude. Similarly we compute the three separate sums of the columns and again store the sum of greatest magnitude. Gerschgorin's theorem tells us the smallest in magnitude of the two stored values is greater than or equal to the magnitude of the largest eigenvalue of the amplification matrix G. Therefore if the magnitude of this number is less than or equal to one the chosen time step Δt should render the difference scheme locally (in space and time) stable. If the magnitude is greater than one the time step is halved and the computation repeated until a satisfactory value for Δt is obtained.

The subroutine which carries out this numerical stability test should, in theory, be applied at each mesh point at every time step. In practice, it is only found to be necessary to apply it at, on average, every fifty time steps. Also many test runs on the computer showed the value of the stable time step obtained in this way to be pessimistic.

REFERENCES

1 Artsimovich, L.A. et al, Plasma Physics and controlled Nuclear Fusion Research (Proc. 2nd Int. Conf. Novosibirsk, 1968), IAEA, VIenna, 1, (1969).

2 Tomimura, A. and Haines, M.G., J. Plasma Physics (1980) Vol.23, part 1, pp.1-20.

3 Tomimura's thesis submitted for the degree of Doctor of Philosophy, 1977, London.

4 Haines, M.G. and Marsh, F., J. Plasma Physics (1982), Vol.1, part 1.

5 Shipuk, I. Ya and Pashkin, S.V. (1968) Soviet Physics Dokl. 12, 10.

6 Zukowski, E.E. and Gilpin, R.R. (1967) Physics of Fluids, 10, 9.

7 Sören Plamgren, Physica Scripta, 9, 184-188, (1974).

8 Nelson, A.H. and Haines, M.G., Plasma Physics, 11, 811-827, (1969).

9 Kerrebrock, J., AIAAJ, 2, 6 (1964).

10 Haines, M.G., J. Plasma Physics, 12, 1, (1974).

11 Dixon, R.H., Düchs, D.F. and Elton, R.C., Physics of Fluids, 16, 1762, (1973).

12 Tomimura, A., Haines, M.G., Plasma Physics, 22, Part 3, 397-420, (1979).

13 Furth, H.P., Rosenbluth, M.N., Rutherfor d, P.H. and Stodiek, W., Physics of Fluids, 13, No.12, 3020-30, (1970).

14 Survey of Tokamak experiments CLM R176 (1977) by R.J. Bickerton, Culham Laboratory Report.

15 Evans, D.E. and Katzenstein, J., Rep. Prog. Physics, 32, 207-271, (1969).

16 Cowling, G.T., Proc. Royal Soc. (London) A183, 453, (1945).

17 Landshoff, R.K.M., Phys. Rev., 76, 904, (1949).

18 Spitzer, L. Jr and Härm, R., Phys. Rev. 89, 977, (1953).

19 Braginskii, S.I., ZhETF, 33, 459 (1957) Soviet Phys. JETP, 6, 358, (1958).

20 Spitzer, L. Jr, "Physics of fully ionised gases", Interscience 2nd edition, 1962.

21 Rose, D.J., Clark, M. Jr, Plasmas and Controlled Fusion, M.I.T Procs. 1st edition, 1961.

22 Chapman, S., Cowling, G.T., "The Mathematical theory on non-uniform gases", Cambridge University Press, 3rd edition, 1970.

23 Braginskii, S.I., "Review of Plasma Physics", (Leontovich, M.A. Gd.) Consultant Bureau, N.Y., 1, 205, (1965).

24 Summers, H.P., McWhirter, R.W.P., J. of Physics B Atomic and Molecular Physics, 12, No.14, (1979).

25 Dreicer, H., 1958, Proc. 2nd Int. Conf. on the peaceful uses of atomic energy, 31, 57 (Geneva : United Nations).

26 Wesson, J. in Lectures fro- the Culham Plasma Physics Summer Schools, (1974).

27 Richtmyer, R.D., Morton, K.W., "Difference methods for initial value problems" 2nd edition, Interscience Publishers, John Wiley and Sons (1967).

28 Potter, D.E., Computational Physics (John Wiley, London, 1972).

29 Marsh, F. and Potter, D.E., Computer Physics Communications, 24, 185-190, (1981).

30 Gerschgorin's theorem "Computational Methods in partial differential equations", p.10. Ames, W.F. (1977).

31 Wesson, J.A., Sykes, A., Lewis, H.R., Plasma Physics, 15, 49-55, (1973).

32 Biskamp, D., Chodura, R., Phys. Rev. Letts, 27, No.23, (1971).

33 Lindman, E.L., J. de Physique, 38, Colloque C6, 9, (1977).

34 Cecam Workshop report 1979.

35 Biskamp, D., Chodura, R., Phys. Fluids, 16, 893, (1973).

36 Weinstock, J., Sleeper, A.M., Phys. Fluids, 18, 247, (1975).

37 Vekshtein and Sagdeev, JETP Lett. 9, 194, (1970).

Computer Physics Communications 24 (1981) 185–190
North-Holland Publishing Company

RECURRENCE SOLUTION OF A BLOCK TRIDIAGONAL MATRIX EQUATION WITH NEUMANN, DIRICHLET, MIXED OR PERIODIC BOUNDARY CONDITIONS

F. MARSH and D.E. POTTER
Department of Physics, Imperial College of Science and Technology, London SW7 2BZ, UK

Received 23 July 1981

PROGRAM SUMMARY

Title of program: PERDIAG

Catalogue number: AARF

Program obtainable from: CPC Program Library, Queen's University of Belfast, N. Ireland (see application form in this issue)

Computer: CDC 6500; *Installation*: Imperial College Computer Centre

Operating system: NOS

Programming language used: FORTRAN IV

High speed storage required: 17.7 Kwords

No. of bits in a word: 60

Overlay structure: none

No. of magnetic tapes required: none

Other peripherals used: card reader, line printer

No. of cards in combined program and test deck: 445

Card punching code: CDC

Key words: matrix equation, perdiagonal, tridiagonal, $n \times n$ blocks, direct method, recursive, periodic boundary conditions, n finite difference equations, one space dimension, implicit

Nature of physical problem
A theorist may wish to solve the matrix equation $AU = W$, rapidly, where A is a block tridiagonal matrix. This type of matrix equation frequently arises in the solution of problems in one space dimension; in the solution of boundary-value and many initial-value problems (because the time-dependent problem has been formulated implicitly), where it is necessary to solve n coupled, finite difference equations. The program is capable of dealing with Neumann, Dirichlet, mixed or periodic boundary conditions. If the boundary conditions are periodic, the resulting matrix A is block tridiagonal with additional blocks in the upper right and left corners, referred to here as block perdiagonal.

Method of solution
A recurrence solution is used to solve the matrix equation $AU = W$. The method follows the principles for a recurrence solution of a tridiagonal matrix equation [1], modified, when appropriate, to deal with the more complex case of periodic boundary conditions.

Restrictions on the complexity of the problem
None. The method does not assume any particular properties of the $n \times n$ submatrices, other than their being non-singular.

Typical running time
The test runs took about 0.3 s. Generally, the running time would depend on the size of the blocks and the number of mesh points.

References
[1] D. Potter, Computational physics (John Wiley, London, 1972).

LONG WRITE-UP

1. Introduction

The computer program described uses a recursive method to solve both the block perdiagonal and the block tridiagonal matrix equations, $AU = W$.

The program has been used as part of a larger code to follow the non-linear time development of electrothermal instabilities in a fully ionized plasma. This involves the solution of a block perdiagonal matrix equation at every iteration within each time step. In this case, there are three coupled equations, differenced using a Crank Nicholson implicit method. Hence the dimensions of the blocks are 3×3. The number of mesh points used was fifty.

2. Description of the problem and the method of solution

We are interested in solving equations of general form,

$$a_j U_{j+1} + \beta_j U_j + \gamma_j U_{j-1} = W_j \,, \tag{1}$$

at every mesh point j, $j = 1, ..., J$, where α_j, β_j and γ_j are $n \times n$ submatrices, and W_j and U_j are n-component column vectors. Using periodic boundary conditions, $U_1 = U_J$ and $(dU/dx)_1 = (dU/dx)_J$, the number of independent equations reduces from J to $J - 1$, and eq. (1) may be written in matrix form:

$$\begin{Bmatrix} \beta_1 & \alpha_1 & 0 & & \dots & & \gamma_1 \\ \gamma_2 & \beta_2 & \alpha_2 & & \dots & & 0 \\ 0 & \gamma_3 & \beta_3 & \alpha_3 & \dots & & 0 \\ \vdots & & & & & & \\ \alpha_{J-1} & 0 & & & \dots & 0 \; \gamma_{J-1} & \beta_{J-1} \end{Bmatrix} \begin{Bmatrix} U_1 \\ U_2 \\ U_3 \\ \vdots \\ U_{J-1} \end{Bmatrix} = \begin{Bmatrix} W_1 \\ W_2 \\ W_3 \\ \vdots \\ W_{J-1} \end{Bmatrix} . \tag{2}$$

Using more general boundary conditions, written in differential form,

$$\left(B \frac{dU}{dx} + CU\right)_{X_1} = D, \quad \left(B' \frac{dU}{dx} + C'U\right)_{X_J} = D', \tag{3}$$

where B, B', C and C' are $n \times n$ matrices (diagonal matrices), and D and D' are n-component column vectors. The number of equations is J, and the resulting matrix is block tridiagonal, i.e. there are no submatrices in the upper right and lower left corners.

3. Solutions and boundary conditions

3.1. Recursive solution – periodic boundary conditions

Assume a recursive solution exists of the form,

$$U_{j-1} = \chi_j U_j + \psi_j U_{J-1} + Y_j \,, \tag{4}$$

where again χ_j and ψ_j are $n \times n$ matrices, and Y_j is an n-component column vector. If the boundary conditions are not periodic, the second term on the right hand side of eq. (4) is not included. This is because, with periodic boundary conditions, there exists a cyclic coupling of points, as well as the intimate coupling of neighbouring points existing with more general boundary conditions. If eq. (4) is applicable at the point j, for consistency it must be applicable at every other point, so the same formula applies at the point $j - 1$. Substituting eq. (4) for U_{j-1} in the original equation (1) and rearranging

$$U_j = -(\beta_j + \gamma_j \chi_j)^{-1} \alpha_j U_{j+1} - (\beta_j + \gamma_j \chi_j)^{-1} \gamma_j \psi_j U_{J-1} + (\beta_j + \gamma_j \chi_j)^{-1} (W_j - \gamma_j Y_j) \,. \tag{5}$$

Eq. (5) has exactly the same form as the recursive relation, eq. (4), namely,

$$U_j = \chi_{j+1} U_{j+1} + \psi_{j+1} U_{J-1} + Y_{j+1} \,. \tag{6}$$

Identifying coefficients in eqs. (5) and (6) gives the relations required to generate the successive values of χ_j, ψ_j and Y_j;

$$\begin{aligned} \chi_{j+1} &= -(\beta_j + \gamma_j \chi_j)^{-1} \alpha_j \,, \\ \psi_{j+1} &= -(\beta_j + \gamma_j \chi_j)^{-1} \gamma_j \psi_j \,, \\ Y_{j+1} &= (\beta_j + \gamma_j \chi_j)^{-1} (W_j - \gamma_j Y_j) \,. \end{aligned} \tag{7}$$

Using eq. (4) at the point $j = 2$, comparing it with the

original equation (1) at the point $j = 1$, gives the following expressions for χ_2, ψ_2 and Y_2;

$$\chi_2 = -\beta_1^{-1}\alpha_1,$$

$$\psi_2 = -\beta_1^{-1}\gamma_1,$$

$$Y_2 = \beta_1^{-1}W_1 . \tag{8}$$

Applying relations (7) at the point $j = 1$, and comparing these with the relations (8), we obtain

χ_1 is a null matrix,
ψ_1 is the identity matrix,
Y_1 is a null vector.

The relations in (7) are now used to scan the mesh upwards from $j = 2$ to $j = J - 1$, providing all required values of χ_j, ψ_j and Y_j. Eq. (4) is then used to scan the mesh downwards in j, from $j = J - 1$ to $j = 2$, to determine values of U at every point, j, on the mesh. The values of the variable U at the point, $j = J - 1$, is needed before the downwards scan can be carried out.

3.2. To determine U_{J-1}

This is achieved by solving two equations in the unknown variables, U_{J-1} and U_{J-2}. The first equation is obtained as follows. Assume a relation exists,

$$e_j U_{j-1} + f_j U_{J-2} + g_j U_{J-1} = h_j , \tag{9}$$

where e_j, f_j and g_j are $n \times n$ matrices and h_j is an n-component column vector. Substituting the expression for U_{j-1} from eq. (4) into eq. (9) yields,

$$e_j\chi_j U_j + f_j U_{J-2} + (e_j\psi_j + g_j)U_{J-1} = h_j - e_j Y_j . \tag{10}$$

Eq. (10) is of the same form as eq. (9), that is,

$$e_{j+1}u_j + f_{j+1}U_{J-2} + g_{j+1}U_{J-1} = h_{j+1} . \tag{11}$$

Hence, identifying coefficients in eqs. (10) and (11), we obtain the equations required to generate successive values of e_j, g_j, f_j and h_j;

$$e_{j+1} = e_j\chi_j,$$

$$f_{j+1} = f_j \text{ , the elements of } f \text{ do not vary with } j, \tag{12}$$

$$g_{j+1} = g_j + e_j\psi_j,$$

$$h_{j+1} = h_j - e_j Y_j .$$

If the original equation (1) is applied at the point $j = J - 1$, and U_J is replaced by U_1, we obtain an equation in the variables U_1, U_{J-1} and U_{J-2}. Now, applying eq. (11) at the point $j = 1$, and comparing the coefficients with the equation described in the last sentence, we obtain expressions defining e_2, g_2, h_2 and f;

$$e_2 = \alpha_{J-1}, \quad f = \gamma_{J-1},$$

$$g_2 = \beta_{J-1}, \quad h_2 = W_{J-1}. \tag{13}$$

The relations in (12) are now used to scan upwards in j to find successive values of e_j, g_j and h_j, and, finally, to find the values of e, g and h at the point $j = J - 1$. We can then write an equation involving the variables U_{J-1} and U_{J-2} only from eq. (11),

$$(e_{J-1} + f)U_{J-2} + g_{J-1}U_{J-1} = h_{J-1} . \tag{14}$$

It is worth noting here that successive values of e_j, g_j and h_j are not stored as only the values at the point $j = J - 1$ are used.

The other equation in U_{J-1} and U_{J-2} only is obtained by applying eq. (4) at the point $j = J - 1$. This equation is then used to eliminate U_{J-2} from eq. (14), giving an equation for U_{J-1} in terms of known quantities, namely

$$U_{J-1} = ((e_{J-1} + f)(\chi_{J-1} + \psi_{J-1}) + g_{J-1})^{-1} \times (h_{J-1} - (e_{J-1} + f)\psi_{J-1}) . \tag{15}$$

We now use this value of U_{J-1} to initiate the scanning procedure described in the last section, and hence find U at every mesh point j.

3.3. Neumann, Dirichlet or mixed boundary conditions

It is a simple matter to perform the same analysis for the case with more general boundary conditions. It is found that the formulae defining the recursive procedure for obtaining solutions to block tridiagonal sets of equations are the same as those defined in relations (7) and (8) except ψ_j is not included. The general boundary conditions in eq. (3) may be written in difference form,

$$BU_2 + (\Delta C - B)U_1 = \Delta D ,$$

$$-B'U_{J-1} + (\Delta C' + B')U_J = \Delta D', \tag{16}$$

where Δ represents the space separation of the mesh

points, and is hence a number. Comparing the equations in relation (16) with eq. (1) at the points $j = 1$ and $j = J$, respectively,

(a)	(b)	
$\alpha_1 = B$,	α_J is a null matrix,	
$\beta_1 = \Delta C - B$,	$\beta_J = \Delta C' + B'$,	(17)
γ_1 is a null matrix,	$\gamma_J = -B'$,	
$W_1 = \Delta D$,	$W_J = \Delta D'$.	

Relations (17a) are then used in (8) to define the starting values χ_2 and Y_2. The first and third equations in (7) are used to scan the mesh upwards from $j = 2$ to $j = J$, providing all required values of χ_j and Y_j. This time χ_j and Y_j at $j = J$ are defined because, unlike the periodic case, the points $j = 1$ and $j = J$ are not equivalent. The values of the variable U at the point $j = J$ are defined using the consistency of the recursion relation, eq. (4), at the point $j = J$, with the boundary condition, the second equation in (16),

$$U_J = (\Delta C' + B' - B'\chi_J)^{-1}(\Delta D' + B'Y_J)$$
$$= (\beta_J + \gamma_J\chi_J)^{-1}(W_J - \gamma_J Y_J)\,. \qquad (18)$$

U_J is now used to initiate the downwards scan to determine U_j at every mesh point j.

4. The computer program

The listing of the program contains a description of the input data required, and what the program is doing at every stage. The input required is the values of the elements of the $n \times n$ matrices, α_j, β_j and γ_j at every mesh point j, $j = 1$ to $J - 1$, (or to $j = J$ if non-periodic boundary conditions are used) stored as three-dimensional arrays, the values of the elements of the n-component column vectors W_j at every mesh point j, stored as a two-dimensional array, the value of n, (referred to in the program as NBLK) and either mesh1 (mesh1 $= J - 1$) if periodic boundary conditions are used or mesh (mesh $= J$) otherwise. The dimensions of the arrays in the DIMENSION statement in the main program must be changed accordingly. The value of "NPER" should be set to zero for general boundary conditions and 1 for periodic boundary conditions. These are the only changes that have to be made by the user. The user may, of course, change the three FORMAT statements in the main program to suit his requirements. There are two READ statements, detailing how the input information is read in, with two corresponding FORMAT statements. The remaining FORMAT statement is associated with the WRITE command which writes the results, U, a two-dimensional array.

The program consists of a main program, PERDIAG, and the subroutines: MULT, ADD, MINUS, EQUAL, NEG, NULL, IDENT, GAUSS and IFAILS. All the subroutines, with the exception of the last two, perform elementary matrix algebra. An explanation of how each subroutine works is given in the listing. Subroutine GAUSS has two functions, dependent upon the arguments with which it is called. The first function is to invert an $n \times n$ matrix by Gauss elimination [2]; the second is to solve the matrix equation, $CU = D$, where C is an $n \times n$ matrix, again using Gauss elimination [2]. Subroutine IFAILS is called if the matrix to be inverted, or the matrix, C, is singular, and the error message, "the matrix is singular", is written to output, and the program stops.

The first part of the main program calculates the elements of χ_j, Y_j (and ψ_j, if NPER = 1), for $j = 1$ to $J - 1$ (to J if NPER = 0) using relations (7) and (8), and stores them. The second part calculates successive values of the elements of e_j, g_j, h_j, and the values of the elements of f (relations (12) and (13)). Only the values of e_j, g_j, h_j, at $j = J - 1$ are stored together with f. This second part is by-passed if NPER = 0. The elements of the column vector U_{J-1} are then found, eq. (15), if NPER = 1 or the elements of U_J, eq. (18), if NPER = 0. The final stage of the main program consists of a backwards scan to find the elements of U_j for all j using the values of χ_j, Y_j (and ψ_j defined if NPER = 1) previously stored, and eq. (4).

The test runs were performed for mesh1 = 5 and n = NBLK = 4, with NPER = 1 and NPER = 0. The elements of α_j, β_j, γ_j and U_j were chosen, using a random number generator, and the elements of W_j found by multiplication. α_j, β_j, γ_j and W_j were then used as input for PERDIAG, and the results U_j checked by comparing them with the chosen values of U_j. The only output from the program is the set of values of U_j.

Acknowledgement

One of the authors (F. Marsh) wishes to thank M.A. Christie for his encouragement and interest in this work.

References

[1] D. Potter, Computational physics (John Wiley, London, 1972).
[2] D.K. Fadeev and V.N. Faddeeva, Computational methods of linear algebra (Freeman, San Francisco, 1963).

TEST RUN OUTPUT

```
U(I,J),I INCREASES ACROSS THE PAGE,AND J DOWN
 8.2980E-02  4.0719E-02  9.5484E-02 -2.8989E-01
 1.5045E-01 -1.1252E-01  1.2387E-01  3.0056E-01
 3.1284E-01 -4.2521E-01  3.3655E-01  2.3960E-01
 2.3801E-02  3.5003E-01 -2.8187E-01  2.5902E-01
-2.2102E-01  8.1139E-02 -1.8375E-01  8.7984E-02

U(I,J),I INCREASES ACROSS THE PAGE,AND J DOWN
-2.0740E-01 -2.8187E-01 -3.9531E-01 -4.2437E-01
 8.2980E-02  4.0719E-02  9.5484E-02 -2.8989E-01
 1.5045E-01 -1.1252E-01  1.2387E-01  3.0056E-01
 3.1284E-01 -4.2521E-01  3.3655E-01  2.3960E-01
-4.4800E-01  2.4425E-02  3.6704E-02 -9.0595E-02
```